NAVAL POSTGRADUATE SCHOOL
MONTEREY, CALIFORNIA

THESIS

EVALUATION OF THE STRAIN ENERGY DENSITY METHOD OF NOTCH STRESS CONCENTRATION CALCULATIONS IN THE PLASTIC RANGE

by

Grant B. Stephenson

March, 1996

Thesis Advisor: Gerald H. Lindsey

Approved for public release; distribution is unlimited.

REPORT DOCUMENTATION PAGE

Form Approved OMB No. 0704-0188

1. AGENCY USE ONLY *(Leave blank)*	2. REPORT DATE 28 March 1996.	3. REPORT TYPE AND DATES COVERED Engineer's Thesis

4. TITLE AND SUBTITLE EVALUATION OF THE STRAIN ENERGY DENSITY METHOD OF NOTCH STRESS CONCENTRATION CALCULATIONS IN THE PLASTIC RANGE

5. FUNDING NUMBERS

6. AUTHOR(S) Grant B. Stephenson

7. PERFORMING ORGANIZATION NAME(S) AND ADDRESS(ES)
Naval Postgraduate School
Monterey CA 93943-5000

8. PERFORMING ORGANIZATION REPORT NUMBER

9. SPONSORING/MONITORING AGENCY NAME(S) AND ADDRESS(ES)

10. SPONSORING/MONITORING AGENCY REPORT NUMBER

11. SUPPLEMENTARY NOTES The views expressed in this thesis are those of the author and do not reflect the official policy or position of the Department of Defense or the U.S. Government.

12a. DISTRIBUTION/AVAILABILITY STATEMENT
Approved for public release; distribution is unlimited.

12b. DISTRIBUTION CODE

13. ABSTRACT *(maximum 200 words)*

Accurate stress and strain calculations at a notch usually require a non-linear finite element analysis when local yielding has occurred. The strain energy density hypothesis is a method to predict these stress and strain values. This method proposes that the plastic strain energy density is equivalent to the strain energy density found assuming the material to be entirely elastic. This hypothesis was evaluated using the finite element method, which was tested by comparing to exact solutions of elastic and elasto-plastic problems, to calculate the stress and strain field for two notched plates of varying widths under elasto-plastic loading. For both geometries, a plane stress and plane strain analysis was performed.

The elasto-plastic strain energy density from the finite element method was found to be greater than that predicted by this proposal, which in turn resulted in under-predicting the local stresses and strains. This difference was greater for the plane stress condition than for the plane strain condition. Comparisons were also made with notch stresses based the Neuber method. The two methods appear to give an upper and lower bound to the actual stresses and strains. By combining the results of the strain energy density method and the Neuber method, reasonably accurate estimates of stress and strain values can be obtained.

14. SUBJECT TERMS *Strain Energy Density, Stress Concentration, Elasto-plastic Finite Element Analysis.			15. NUMBER OF PAGES 124
			16. PRICE CODE
17. SECURITY CLASSIFICATION OF REPORT Unclassified	18. SECURITY CLASSIFICATION OF THIS PAGE Unclassified	19. SECURITY CLASSIFICATION OF ABSTRACT Unclassified	20. LIMITATION OF ABSTRACT UL

NSN 7540-01-280-5500

Standard Form 298 (Rev. 2-89)
Prescribed by ANSI Std. 239-18 298-102

EVALUATION OF THE STRAIN ENERGY DENSITY METHOD OF NOTCH STRESS CONCENTRATION CALCULATIONS IN THE PLASTIC RANGE

Grant B. Stephenson
Lieutenant, United States Navy
B.S., United States Naval Academy, 1988
M.S., Naval Postgraduate School, 1995

Submitted in partial fulfillment of the
requirements for the degree of

AERONAUTICAL AND ASTRONAUTICAL ENGINEER

from the

NAVAL POSTGRADUATE SCHOOL
March 1996

ABSTRACT

Accurate stress and strain calculations at a notch usually require a non-linear finite element analysis when local yielding has occurred. The strain energy density hypothesis is a method to predict these stress and strain values. This method proposes that the plastic strain energy density is equivalent to the strain energy density found assuming the material to be entirely elastic. This hypothesis was evaluated using the finite element method, which was tested by comparing to exact solutions of elastic and elasto-plastic problems, to calculate the stress and strain field for two notched plates of varying widths under elasto-plastic loading. For both geometries, a plane stress and plane strain analysis was performed.

The elasto-plastic strain energy density from the finite element method was found to be greater than that predicted by this proposal, which in turn resulted in under-predicting the local stresses and strains. This difference was greater for the plane stress condition than for the plane strain condition. Comparisons were also made with notch stresses based the Neuber method. The two methods appear to give an upper and lower bound to the actual stresses and strains. By combining the results of the strain energy density method and the Neuber method, reasonably accurate estimates of stress and strain values can be obtained.

TABLE OF CONTENTS

I. INTRODUCTION 1
A. FATIGUE LIFE 1
B. STRESS CONCENTRATION FACTOR 2

II. THEORETICAL BACKGROUND 5
A. NEUBER'S MODEL 5
B. GLINKA MODEL: STRAIN ENERGY DENSITY APPROACH 6

III. STRAIN ENERGY 9
A. STRAIN ENERGY PRINCIPLE 9
B. DERIVATION OF STRAIN ENERGY RELATIONSHIP 10
C. STRAIN ENERGY DENSITY 11
1. Strain Energy Density for the Elastic Case 12
2. Strain Energy Density for the Plastic Case 12

IV. VERIFICATION OF FINITE ELEMENT METHOD 15
A. VERIFICATION OF ELASTIC FINITE ELEMENT MODEL 17
1. Elliptical Hole in an Infinite Plate 17
2. Conclusion of Elastic Finite Element Model 25
B. VERIFICATION OF ELASTOPLASTIC FINITE ELEMENT MODEL 25
1. Uniaxial Test of Stress-Strain Curve 25
2. Infinite Plate with a Circular Hole 26
3. Comparison to Experimental Data 41

V. NUMERICAL CALCULATION OF STRAIN ENERGY DENSITY 51
A. INTEGRATION ROUTINE 51
B. RESULTS OF NUMERICAL SCHEME ON UNIAXIAL CASE 53

VI. CALCULATIONS AND RESULTS OF STRAIN ENERGY DENSITY 57
A. NOTCH GEOMETRY AND MATERIAL SELECTION 57
B. FINITE ELEMENT MODELING 59
C. RESULTS OF FINITE ELEMENT ANALYSIS 66
1. Computational Procedures 66
2. Plane Stress Condition 66
3. Plane Strain Condition 74

VII. STRESS AND STRAIN CALCULATIONS 81
A. PLANE STRESS CONDITION 81
1. Finite Element Method Results 81
2. Notch Root Stress and Strain Calculations and Comparisons 84
B. PLANE STRAIN CONDITION 90
1. Finite Element Method Results 90

2. Notch Root Stress and Strain Calculations 90

VIII. APPLICATION OF RESULTS TO FATIGUE CALCULATIONS 101
A. STRAIN LIFE CALCULATIONS 101
B. RESULTS OF STRAIN LIFE FATIGUE PREDICTIONS 102

IX. CONCLUSIONS 105
A. FINITE ELEMENT CALCULATIONS 105
B. STRAIN ENERGY DENSITY CALCULATIONS 106
C. NOTCH ROOT STRESS AND STRAIN CALCULATIONS 107
D. IMPACT ON FATIGUE LIFE PREDICTIONS 107
E. RECOMMENDATIONS 108

REFERENCES 109

INITIAL DISTRIBUTION LIST 111

LIST OF SYMBOLS

b	fatigue strength exponent
c	fatigue ductility exponent
δ_{ij}	Kronecker delta
E	Young's modulus
E_p	plastic modulus (slope of plastic stress-strain curve)
E_s	secant modulus of plastic stress-strain curve
E_s^t	secant modulus of total stress-strain curve
e	far-field strain
ε	local uniaxial strain
ε_{ij}	total strain components
ε_{ij}^e	elastic strain components
ε_{ij}^p	plastic strain components
ε_{et}	equivalent total strain
ε_e^e	equivalent elastic strain
ε_e^p	equivalent plastic strain
ε_f'	fatigue ductility coefficient
FEM	finite element method
G	shear modulus
K	strength coefficient
K_t	theoretical stress concentration factor
K_σ	stress concentration factor
K_ε	strain concentration factor
λ	Lamé's constant
n	strain hardening exponent
N_f	reversals till crack initiation
σ	local uniaxial stress

σ_{ij}	local stress component
σ_e	equivalent stress
σ_0	yield stress
σ'_f	fatigue strength coefficient
S	nominal stress
s_{ij}	stress deviator tensor
W_o	strain energy density
W_e	strain energy density based on elastic material properties
W_p	strain energy density based on elasto-plastic material properties
W_σ	local strain energy density
W_S	farfield strain energy density

ACKNOWLEDGMENT

The author would like to thank Prof. Lindsey for his indispensably guidance and patience throughout this study. The author also thanks his wife, Reneé, for her support, encouragement, and understanding during this work.

I. INTRODUCTION

A. FATIGUE LIFE

Fatigue phenomena were first considered in 1850 when it was discovered that railroad car axles failed after a certain amount of time under cyclic loads. The concept of endurance limit was introduced, which states that below a minimum load cyclic load, or endurance limit S_e, some materials will never fail [Ref. 1]. To prevent fatigue failure, one only has to design the structure strong enough so that the stresses remain below this endurance limit. However, certain structural applications require low weight, and this excessive design would be unfeasible. Such is the case with aircraft. All aircraft are put under cyclic loads every flight – from repetitive takeoffs and landings, basic maneuvering, and flight gust loads. While aircraft are designed to withstand mechanical failure modes of large scale yielding and sudden monotonic fracture, it is unrealistic to design an aircraft that will never experience fatigue.

It is not surprising then that the service lives of U. S. Naval Aircraft are based on the fatigue life of the aircraft structure. Due to both a safety factor and a cost factor, the structural life of every U. S. Naval aircraft is thoroughly tracked. Engine or aircraft system components can be replaced, but when the main structural components of an aircraft fail, there are few options. The aircraft is either taken out of service, or major and costly rework such as replacing the wings on the A-6E Intruder aircraft is required to extend its life. Known weak spots are constantly inspected and reworked, if required, to extend the life of the aircraft. These critical areas of failure, or crack initiation, usually occur at stress concentrations, such as those occurring at notches or rivet holes. Current fatigue calculations can estimate the cyclic life of a component given the range of stresses and strains it will undergo. However, for these calculations to be accurate, precise stress and strain figures are required. This is especially true when the cyclic fatigue calculations occur over tens of thousands of cycles, and any error gets multiplied many-fold. Thus, accurate calculations of the stress at a notch root is the first step in accurate fatigue life estimation.

B. STRESS CONCENTRATION FACTOR

Stress concentrations are stresses that are locally higher than the far-field stress for any loaded material. Stresses increase and decrease due to the geometry of a part, and when abrupt geometric changes occur, such as a notch or a hole, stresses can be two to three times greater than the far-field stresses. Given a defined geometry and applied loads, a ratio of local (notch root) stress σ to the far-field stress S can be determined and remains constant as long as σ and S remain in the linear range of the stress-strain curve. For a notched specimen, the maximum stress will occur at the notch root, and the ratio of the maximum stress to the nominal stress is the stress concentration factor:

$$K_t = \frac{\sigma}{S} \qquad (1.1)$$

Throughout this thesis, K_t is the theoretical stress concentration factor based on a elastic model. Even though it is labeled theoretical, its value may be obtained from analytic solutions or a finite element analysis. Regardless, it is a constant and holds for any stresses in the elastic range.

The difficulty in calculating the stresses for a geometry such as a notch or a hole arise when local yielding occurs. Although an analytic solution or a finite element analysis can easily calculate the stress concentration factor that remains constant in the elastic range, as soon as plastic yielding occurs, this stress concentration factor decreases in magnitude as the yield zone around the notch increases. This may often be the case, since local yielding is allowed in the design of the aircraft, and for stress concentrations of two to three, it is difficult to design a structurally efficient wing that will prevent local yielding. Once the local stress departs the linear range of the stress-strain curve, it thus becomes more difficult to calculate the local stresses and strains at the notch root. A finite element analysis is possible, but this becomes expensive and time consuming when used in high-cycle fatigue calculations that involve tens of thousands of runs.

In 1961, H. Neuber [Ref. 2] derived a relationship for determining stresses and strains at a notch that has been loaded into the plastic range. Although Neuber's derivation involved a notch loaded in antiplane shear, it has been widely applied to general notch problems. By the 1980's, the Neuber method had been adopted by virtually

all fatigue analysts, including the Naval Air Systems Command. However, over the years since Neuber's original paper and ever since it has come into prominent use, many investigators have proposed alternative means.

One proposal by Glinka et al. [Ref. 3, 4, 5, 6] is based upon the concept that the strain energy density of the material in the yielded zone is virtually the same as the strain energy density considering the material to be elastic. This is represented below in Figure 1.1, where W_e is the strain energy density assuming an elastic material and equals the area under the linear curve, and W_p is the strain energy density for an elasto-plastic material and equals the area under the nonlinear curve. This conjecture results in being able to calculate the stress concentration factor in the elasto-plastic zone from the strain energy density of the elastic model. This proposal is based on reasoning that the for local plastic yielding, there is a relatively large volume of material in the elastic region surrounding the plastic zone. Glinka continued to work on his proposal through the 1980's, and published several papers applying his model to plane stress and plane strain problems. In

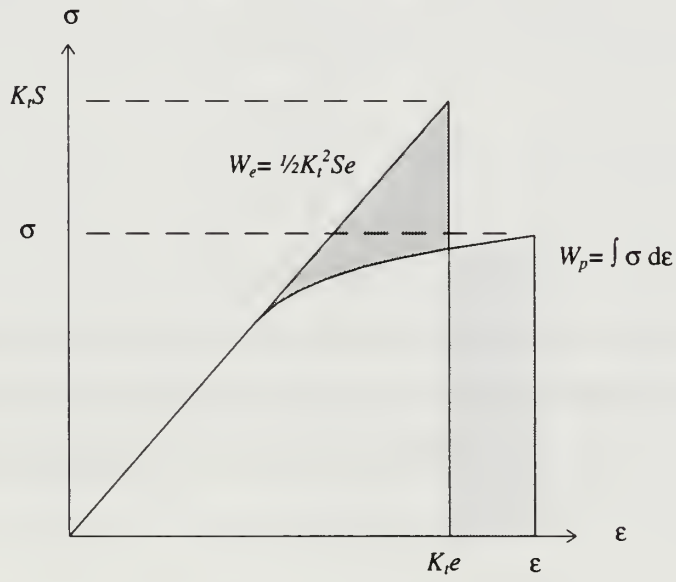

Figure 1.1. Representation of Strain Energy Density Equivelance Concept

1992 W. N. Sharpe, Jr., C. H. Yang, and R. L. Trengoning [Ref. 7] evaluated the Glinka relations with that of Neuber's for various plane strain and plain stress configurations using experimental data at the notch root. Their conclusions were mixed, and stated that

some cases were better predicted by the Glinka model, while others were accurately predicted by the Neuber model.

Drawing upon advanced finite element techniques, the proposal that the strain energy density in the plastic zone is equal to that calculated on the basis of an elastic solution has been further tested, not only at the notch root, but throughout the plastic zone of the model. Elastic and Elasto-plastic problems with closed form solutions, along with previously published experimental data have verified the finite element modeling, which was then used to calculate strain energy density. Assessments are then made of its impact upon fatigue life calculations of aircraft as compared to the Neuber approach.

II. THEORETICAL BACKGROUND

This thesis will concentrate on the Glinka model for calculating the stress concentration in the elasto-plastic range. The Neuber model is reviewed below, and will be used for comparison of results at the notch root with that of the Glinka model.

A. NEUBER'S MODEL

Neuber proposed that at the notch root under plastic yielding, the elastic stress concentration factor was the geometric mean of the stress concentration factor and strain concentration factor, as shown in Equation 2.1 [Ref. 2].

$$K_t = \sqrt{K_\sigma K_\varepsilon} \tag{2.1}$$

$$\text{where } K_\sigma = \frac{\sigma}{S} \text{ and } K_\varepsilon = \frac{\varepsilon}{e}$$

When the far-field stress S is in the linear rage, this can be rewritten as:

$$K_t^2 = K_\sigma K_\varepsilon$$

$$K_t^2 = \frac{\sigma}{S}\frac{\varepsilon}{e}$$

$$K_t^2 = \frac{\sigma}{S}\frac{\varepsilon E}{S}$$

or:

$$(K_t S)^2 = E\sigma\varepsilon \tag{2.2}$$

There are two unknowns here, σ and ε. To solve for them, the stress-strain constitutive relationship is required. One of the most common stress-strain relationships that can be applied is the Ramberg-Osgood curve. For a uniaxial stress state, this is:

$$\varepsilon = \frac{\sigma}{E} + \left(\frac{\sigma}{K}\right)^{\frac{1}{n}} \tag{2.3}$$

where E, K, and n are obtained from a curve fit to the uniaxial stress-strain curve. Substituting Equation 2.3 into Equation 2.2, the Neuber relation gives Equation 2.4 shown below.

$$\frac{(K_t S)^2}{E} = \frac{\sigma^2}{E} + \sigma\left(\frac{\sigma}{K}\right)^{\frac{1}{n}} \tag{2.4}$$

For the above derivation, the stress-strain relationship using the Ramberg-Osgood relationship is based on true stress, $\bar{\sigma}$, and true strain, $\bar{\varepsilon}$. However, the computational finite element analysis is based on engineering stresses and strains, σ and ε. The relationship between true and engineering stresses and strains, valid up to necking, is given below in Equation 2.5. It can be seen that for small strains such as $\varepsilon \leq 0.01$, the difference between true and engineering strains is less than 0.5%, and the difference between true and engineering stresses is less than or equal to 1.0%. Therefore, for small strains, as is the case in this thesis, the true and engineering stresses and strains can be interchanged without any significant error.

$$\bar{\varepsilon} = \ln(1+\varepsilon) \qquad \bar{\sigma} = \sigma(1+\varepsilon) \qquad (2.5)$$

While Neuber's rule has been well established as an engineering tool to calculate notch stresses and strains, it has been shown to overestimate these values [Ref. 3]. The accuracy of strain estimation is critical for fatigue calculations, therefore, a more accurate method would prove very beneficial.

B. GLINKA MODEL: STRAIN ENERGY DENSITY APPROACH

Glinka proposed that the energy density at the notch root, calculated on the basis of elasto-plastic constitutive laws, is equal to that based on linear elastic constitutive laws for equivalent far-field loading. In Chapter III, a detailed derivation of the strain energy density will be shown, for now it is given below for the uniaxial case:

$$W_o = \int_0^{\varepsilon} \sigma \, d\varepsilon \qquad (2.6)$$

Using the above definition of strain energy density, the strain energy at the notch and far-field regions are calculated (using a linear elastic stress-strain relationship $\sigma = E\varepsilon$). For the notch root, this becomes:

$$W_\sigma = \int_0^{\varepsilon} E\varepsilon \, d\varepsilon \qquad (2.7)$$

$$W_\sigma = E\frac{\varepsilon^2}{2} \qquad (2.8)$$

$$W_\sigma = \frac{\sigma^2}{2E} \qquad (2.9)$$

For the far-field region, $\sigma = S$ and $\varepsilon = e$:

$$W_S = E\frac{e^2}{2} \qquad (2.10)$$

$$W_S = \frac{S^2}{2E} \qquad (2.11)$$

Rewriting the stresses in terms of strain energy density and substituting these values into the theoretical stress concentration factor in Equation 1.1, one gets:

$$K_t = \sqrt{\frac{W_\sigma}{W_S}} \qquad (2.12)$$

However, Glinka's hypothesis is that the strain energy density at the root will result in the same value, regardless if calculated for a linear elastic or an elasto-plastic material. Therefore, this ratio remains constant, even when local yielding occurs at the notch root. The argument is that if the area of local yielding is small, and is surrounded by a large volume of elastic material, then the energy distribution does not change significantly, even when local yielding occurs.

For a nonlinear stress-strain relationship, W_σ is found by manipulating the integrand of Equation 2.6:

$$\sigma\, d\varepsilon = \varepsilon\, d\sigma + \sigma\, d\varepsilon - \varepsilon\, d\sigma = d(\sigma\varepsilon) - \varepsilon\, d\sigma \qquad (2.13)$$

Substituting Equation 2.13 into Equation 2.6 results in:

$$W_\sigma = \int\left[d(\sigma\varepsilon) - \varepsilon\, d\sigma\right] = \sigma\varepsilon - \int_0^\sigma \varepsilon\, d\sigma \qquad (2.14)$$

Substituting the Ramberg-Osgood stress-strain relationship (Equation 2.3) into Equation 2.14 results in the strain energy density in terms of the local uniaxial stress:

$$W_\sigma = \frac{\sigma^2}{E} + \left(\frac{1}{K}\right)^{\frac{1}{n}}(\sigma)^{\frac{1}{n}+1} - \int\left[\frac{\sigma}{E} + \left(\frac{\sigma}{K}\right)^{\frac{1}{n}}\right]d\sigma \qquad (2.15)$$

$$W_\sigma = \frac{\sigma^2}{E} + \left(\frac{1}{K}\right)^{\frac{1}{n}}(\sigma)^{\frac{1}{n}+1} - \left[\frac{\sigma^2}{2E} + \left(\frac{1}{K}\right)^{\frac{1}{n}}(\sigma)^{\frac{1}{n}+1}\left(\frac{1}{\frac{1}{n}+1}\right)\right] \qquad (2.16)$$

$$W_\sigma = \frac{\sigma^2}{2E} + \left(\frac{\sigma}{1+n}\right)\left(\frac{\sigma}{K}\right)^{\frac{1}{n}} \qquad (2.17)$$

Substituting 2.17 back into the ratio for K_t (Equation 2.12) one obtains an equation in terms of the far-field stress S, material properties E, n, and K, and the theoretical stress concentration factor K_t that can be solve numerically for the local stress σ:

$$\frac{(K_t S)^2}{E} = \frac{\sigma^2}{E} + \frac{2\sigma}{1+n}\left(\frac{\sigma}{K}\right)^{\frac{1}{n}} \qquad (2.18)$$

This expression applies only for the uniaxial case. In Chapter III, the strain energy density is expressed in terms of the general stress-strain equations.

By inspecting Equations 2.18 from Glinka and Equation 2.4 from Neuber, one can observe that the only difference is the factor of $2/(1+n)$ in the strain energy density model. Since n is less than 1, this term is greater than 1, and for the left side of these two equations to be equal, the local stress in Equation 2.18 must be less than the local stress in Equation 2.4. Likewise, if the local stress in the strain energy model are lower than those in the Neuber model, so will be the local strains. In fact, Glinka states that the Neuber model has been shown to overestimate the local stresses and strains [Ref. 3].

III. STRAIN ENERGY

A. STRAIN ENERGY PRINCIPLE

For a general deformable body, external applied loads will cause internal stresses and strains to develop until an equilibrium point is reached. The result is an internal potential energy, or stored energy that is able to do work. In other words, potential strain energy is the potential energy due to internal stresses referenced from a zero stress state of a deformable body. For a system with no losses, potential energy equals the work put into the system. To develop the strain energy relationship, consider a general body with externally applied loads as shown in Figure 3.1 below.

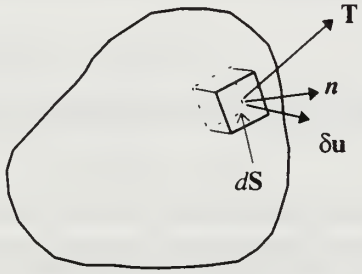

Figure 3.1. External Loads to a General Deformable Body.

Given a traction force **T** acting on a portion of the body $d\mathbf{S}$ with a outward normal **n** and that displaces $\delta\mathbf{u}$, then the work increment is:

$$\delta W = \iint_S \left(\vec{T} \bullet \delta\vec{u}\right) dS \qquad (3.1)$$

To develop potential strain energy, the basic governing equations are shown below:

Boundary Conditions:

$$\begin{aligned} T_x &= \sigma_{xx} n_x + \sigma_{xy} n_y + \sigma_{xz} n_z \\ T_y &= \sigma_{xy} n_x + \sigma_{yy} n_y + \sigma_{yz} n_z \\ T_z &= \sigma_{xz} n_x + \sigma_{yz} n_y + \sigma_{zz} n_z \end{aligned} \qquad (3.2)$$

Equations of Equilibrium:

$$\begin{aligned}
\frac{\partial \sigma_{xx}}{\partial x} + \frac{\partial \sigma_{xy}}{\partial y} + \frac{\partial \sigma_{xz}}{\partial z} &= 0 \\
\frac{\partial \sigma_{xy}}{\partial x} + \frac{\partial \sigma_{yy}}{\partial y} + \frac{\partial \sigma_{yz}}{\partial z} &= 0 \\
\frac{\partial \sigma_{xz}}{\partial x} + \frac{\partial \sigma_{yz}}{\partial y} + \frac{\partial \sigma_{zz}}{\partial z} &= 0
\end{aligned} \qquad (3.3)$$

Strain-Displacement Relationships (Engineering Strains):

$$\begin{aligned}
\varepsilon_{xx} &= \frac{du}{dx} & \varepsilon_{yy} &= \frac{dv}{dy} & \varepsilon_{xx} &= \frac{dw}{dz} \\
\varepsilon_{xy} &= \frac{dv}{dx} + \frac{du}{dy} & \varepsilon_{xz} &= \frac{dw}{dx} + \frac{du}{dz} & \varepsilon_{yz} &= \frac{dw}{dy} + \frac{dv}{dz}
\end{aligned} \qquad (3.4)$$

B. DERIVATION OF STRAIN ENERGY RELATIONSHIP

From this point on, tensor notation will be used as a shorthand notation to develop the strain energy terms. The governing equations are rewritten below. The only change is in the shear strain terms, in which the tensor shear strains are 1/2 of the value of the engineering shear strains.

Boundary Conditions: $$T_i = \sigma_{ij} n_j \qquad (3.5)$$

Equilibrium Equations: $$\frac{\partial \sigma_{ij}}{\partial x_j} = \sigma_{ij,j} = 0 \qquad (3.6)$$

Strain Displacement Relationships: $$\varepsilon_{ij} = \frac{1}{2}\left(u_{i,j} + u_{j,i}\right) \qquad (3.7)$$

Returning to equation 3.1, we substitute in the boundary conditions and expand:

$$dW = \iint_S T_i \, \delta u_i \, dS$$

$$dW = \iint_S \left(\sigma_{ij} n_j\right) \delta u_i \, dS$$

$$dW = \iint_S \left(\sigma_{ij} \delta u_i\right) n_j \, dS$$

At this point, the Gauss-Divergence theorem can be applied, and the internal strain energy can be obtained from the externally applied loads:

$$\delta W = \iiint_V \left(\sigma_{ij}\delta u_i\right)_{,j} dV$$

$$\delta W = \iiint_V \left(\sigma_{ij,j}\delta u_i + \sigma_{ij}\delta u_{i,j}\right) dV$$

When the equilibrium equations are substituted into the above equation, the first term goes to zero. The result is expanded to form a symmetric and a skew-symmetric matrix:

$$\delta W = \iiint_V \sigma_{ij}\left(\tfrac{1}{2}\delta u_{i,j} + \tfrac{1}{2}\delta u_{i,j}\right) dV$$

$$\delta W = \iiint_V \sigma_{ij}\left[\tfrac{1}{2}\left(\delta u_{i,j} + \delta u_{j,i}\right) + \tfrac{1}{2}\left(\delta u_{i,j} - \delta u_{j,i}\right)\right] dV$$

$$\delta W = \iiint_V \sigma_{ij}\left(\delta\varepsilon_{i,j} + \delta\omega_{i,j}\right) dV$$

where ω is defined as: $$\omega = \frac{1}{2}\left(u_{i,j} - u_{j,i}\right)$$

However, since ω is a skew-symmetric matrix, and since a skew-symmetric matrix multiplied by a symmetric matrix is zero, the last terms disappear in the above equations. The final result is:

$$\delta W = \iiint_V \sigma_{ij}\delta\varepsilon_{ij} dV \qquad (3.8)$$

C. STRAIN ENERGY DENSITY

Equation 3.8 is the differential strain energy. To find the total strain energy, the integration along each strain can be accomplished inside the volume integral. Strain energy density is the strain energy per unit volume and can be represented as the integrand of equation 3.8. The δ operator will be changed to a differential, and when considered from a zero stress state, this becomes:

$$W_o = \int_0^{\varepsilon_{ij}} \sigma_{ij} d\varepsilon_{ij} \qquad (3.9)$$

where ε_{ij} is the strain value at the final stress state.

1. Strain Energy Density for the Elastic Case

To calculate the strain energy density for the elastic case, the elastic stress-strain relationship, given below, is substituted into equation 3.9:

$$\sigma_{ij} = 2G\varepsilon_{ij} + \lambda\varepsilon_{ij}\delta_{ij} \qquad (3.10)$$

with λ given as: $\lambda = \dfrac{vE}{(1+v)(1-2v)}$; $G = \dfrac{E}{2(1+v)}$; and $\delta_{ij} = \begin{cases} 1; & i = j \\ 0; & i \neq j \end{cases}$

The evaluation of the integral is straight forward:

$$W_o^e = \int_0^{\varepsilon_{ij}} \left(2G\varepsilon_{ij} + \lambda\varepsilon_{kk}\delta_{ij}\right) d\varepsilon_{ij} \qquad (3.11)$$

$$W_o^e = G\varepsilon_{ij}\varepsilon_{ij} + \frac{\lambda\varepsilon_{kk}^{\ 2}}{2} \qquad (3.12)$$

$$W_o^e = G\varepsilon_{ij}\varepsilon_{ij} + \frac{\lambda\varepsilon_{kk}\varepsilon_{ij}}{2}\delta_{ij} \qquad (3.13)$$

$$W_o^e = \frac{\varepsilon_{ij}}{2}\left(2G\varepsilon_{ij} + \lambda\varepsilon_{ij}\delta_{ij}\right) \qquad (3.14)$$

Replacing the term in brackets again by the elastic stress-strain relationship, the strain energy density can be written as:

$$W_o^e = \frac{1}{2}\sigma_{ij}\varepsilon_{ij} \qquad (3.15)$$

Geometrically, this is the area under the linear stress-strain curve for the case of uniaxial tension.

2. Strain Energy Density for the Plastic Case

To evaluate the strain energy density for the plastic case, the strain energy density relationship, equation 3.9, is separated into an elastic term and plastic term:

$$W_o = W_o^e + W_o^p = \int \sigma_{ij} d\varepsilon_{ij}^e + \int \sigma_{ij} d\varepsilon_{ij}^p \qquad (3.16)$$

The first term is equation 3.15, and the second term can be manipulated in the same manner as Equation 2.14 to give:

$$W_o = \frac{1}{2}\sigma_{ij}\varepsilon_{ij}^e + \sigma_{ij}\varepsilon_{ij}^p - \int \varepsilon_{ij}^p \, d\sigma_{ij} \qquad (3.17)$$

The stress-strain relationship for elasto-plastic behavior for deformation theory based on the Prandtl-Reuss equations is given as Equation 3.18 [Ref. 8].

$$\varepsilon_{ij} = \left[\frac{1}{2G}\sigma_{ij} - \frac{\nu}{E}\sigma_{kk}\delta_{ij}\right] + \frac{3}{2}\frac{1}{E_s}\left[\sigma_{ij} - \frac{\sigma_{kk}}{3}\delta_{ij}\right] \qquad (3.18)$$

Where E_s is the secant modulus of the effective stress versus plastic strain curve:

$$E_s = \frac{\sigma_e}{\varepsilon_e^p} \qquad (3.19)$$

where the effective stress, σ_e, and effective plastic strain strain, $\varepsilon_e{}^p$, are defined as:

Effective Stress: $$\sigma_e = \sqrt{\tfrac{3}{2} s_{ij} s_{ij}} \qquad (3.20)$$

Effective Plastic Strain $$\varepsilon_e^p = \sqrt{\tfrac{2}{3}\varepsilon_{ij}^p \varepsilon_{ij}^p} \qquad (3.21)$$

where the stress deviator tensor is: $s_{ij} = \sigma_{ij} - \frac{\sigma_{kk}}{3}\delta_{ij}$

Substituting the plastic strain component of the relationship given in Equation 3.18 into Equation 3.17, the strain energy density becomes:

$$W_o = \frac{1}{2}\sigma_{ij}\varepsilon_{ij}^e + \sigma_{ij}\left[\frac{3}{2E_s}\left(\sigma_{ij} - \frac{\sigma_{kk}}{3}\delta_{ij}\right)\right] - \int \frac{3}{2E_s}\left(\sigma_{ij} - \frac{\sigma_{kk}}{3}\delta_{ij}\right) d\sigma_{ij} \qquad (3.22)$$

If the Ramberg-Osgood uniaxial stress-strain curve is rewritten in terms of effective stress and effective strain, it becomes:

$$\varepsilon_e = \varepsilon_e^e + \varepsilon_e^p = \frac{\sigma_e}{E} + \left(\frac{\sigma_e}{K}\right)^{\frac{1}{n}} \qquad (3.23)$$

Substituting the plastic portion of the effective strain of the Ramberg-Osgood relationship in Equation 3.23 into the definition of the secant plastic modulus, Equation 3.19, it can be rewritten in terms of the effective stress and the Ramberg-Osgood material constants.

$$\frac{1}{E_s} = \frac{\left(\frac{\sigma_e}{K}\right)^{\frac{1}{n}}}{\sigma_e} = \left(\frac{1}{K}\right)^{\frac{1}{n}} \sigma_e{}^{\frac{1-n}{n}} \qquad (3.24)$$

Substituting this back into equation 3.22 results in the strain energy density relationship

in terms of stresses only (based on the Ramsberg-Osgood stress-strain curve):

$$W_o = \frac{1}{2}\sigma_{ij}\varepsilon_{ij}^{e} + \sigma_{ij}\left[\frac{3}{2K^{\frac{1}{n}}}(\sigma_e)^{\left(\frac{1-n}{n}\right)}\left(\sigma_{ij} - \frac{\sigma_{kk}}{3}\delta_{ij}\right)\right] - \int \frac{3}{2K^{\frac{1}{n}}}(\sigma_e)^{\left(\frac{1-n}{n}\right)}\left(\sigma_{ij} - \frac{\sigma_{kk}}{3}\delta_{ij}\right)d\sigma_{ij} \quad (3.25)$$

Before calculating the strain energy density from the finite element results, the finite element program as applied to notched geomentries will be verified in Chapter IV. Following verification of the FEM results, the strain energy density Equations 3.9, 3.17 and 3.25 will be numerically integrated to calculate the actual strain energy density.

IV. VERIFICATION OF FINITE ELEMENT METHOD

To evaluate the strain energy density concept for calculating stress concentrations in the plastic zone, a finite element model was used to obtain the stress and strain data as an input to the calculations. However, verification of the finite element data was paramount to ensure that a legitimate analysis is performed. The finite element program used was I-DEAS Master Series™ Release 1.3 and 2.1. Quadrilateral plane stress and plain strain elements were employed, and a non-linear stress-strain analysis was performed.

The I-DEAS Master Series™ offers several approaches to createing a finite element model. The general approach was to create a three dimensional model to represent the physical specimen. Next, an element mesh was created by specifying the type of element to be used and the number of elements on each side of the surface being meshed. All plane stress and plane strain analyses throughout this thesis used an eight node quadrilateral element. These elements are two-dimensional, with nodal degrees of freedom consisting of translation in x and y directions, and rotation about the z axis. Only one face of the model was required to be meshed. A mesh refinement routine can be used to refine the element shapes to reduce distortion (i.e., skewing and stretching), and this routine was used to refine the finite element meshes for all analyses. After generation of the mesh, boundary conditions were applied to represent external loads and fixed displacements. Note that boundary conditions can be applied at lines of symmetry; thus reducing a block by one half or one quarter of the original geometry, resulting in significantly reduced computation time.

Effective mesh generation is paramount in obtaining a correct solution for the finite element method. A coarse mesh (few elements, large distance between nodes) will not produce the correct solution while an overly fine mesh (many elements, small distance between nodes) may result in excessive computational time and storage. Additionally, a dense mesh near large stress gradients is not only necessary for accurate solutions, but also to provide the data for effective post processing analysis. Thus, for each problem, a mesh study was performed to determine the optimal mesh size and distribution to use. This involved running several finite element models with varying

mesh sizes and distributions, and determining at what point further mesh refinements did not effect the solution.

Two additional factors effect the non-linear portion of the analysis: the non-linear stress-strain relationship and the iteration procedure. For a non-linear stress-strain analysis, the I-DEAS Master Series™ program uses input data points to model the stress-strain curve. The program assumes a constant stiffness between each point, breaking the curve up into individual linear sections. A maximum of twenty points can be entered. To ensure a smooth curve, all twenty points were used to define the stress-strain curve, with denser groupings at the highest curvature. Two basic iteration procedures are available: either the Newton-Raphson method or the Modified Newton-Raphson method. The Newton-Raphson method was used, and although this may mean more computational time per iteration, it generally iterates at a faster rate than the Modified Newton-Raphson method, requiring fewer iterations. For either method, a convergence requirement can be set, specifying the minimum value a function can change from one iteration to the next before the solution is considered to have converged.

Two basic types of comparisons can be made: the first to an analytic solution, and the second to experimental data. The first type provides a comparison to an exact solution, and differences between the finite element method and an analytic solution should be minimal. The advantage of this type of comparison is that it will show the error of the finite element method compared to the governing equations of solid mechanics. The comparison of the finite element method to experimental data will indicate how well the finite element method models actual mechanical behavior. The critical area in this case is the elasto-plastic relationship, or how well the Prandtl-Reuss equations represent this relationship. This includes modeling the effective stress and effective strain with a uniaxial stress-strain curve.

Full stress field measurements in solid mechanics must rely on surface techniques and assume plane stress or plane strain conditions. There are also approximations necessary in obtaining the elasto-plastic measurements, such as reducing the data via the Prandtl-Reuss equations. Another disadvantage of using experimental data is the percent error introduced when making measurements. Despite these difficulties and experimental

error, qualitative experimental results are indispensable, and when executed properly, can show were the mathematical model differs from the actual physics. Numerical computational techniques will have no validity unless they can be shown to truly represent the actual physical phenomenon. Therefore, despite the difficulty in obtaining experimental data, an attempt has been made to compare the finite element method to previously published experimental results.

A. VERIFICATION OF ELASTIC FINITE ELEMENT MODEL

1. Elliptical Hole in an Infinite Plate

The first step in the finite element modeling was to ensure the program could obtain accurate results for a notched type of geometry under linear elastic loading. An elliptical hole in an infinite thin plate was used for this comparison. Durelli [Ref. 9] gives the stress distribution around the elliptical boundary and compares this with experimental data. Brown [Ref. 10] gives the complete stress field for any uniaxial load. The stress distributions for a infinite plate with an elliptical hole are given in elliptical coordinates, which are shown in Figure 4.1 and Figure 4.2, for an ellipse of $a = 1$ and $b = 0.5$.

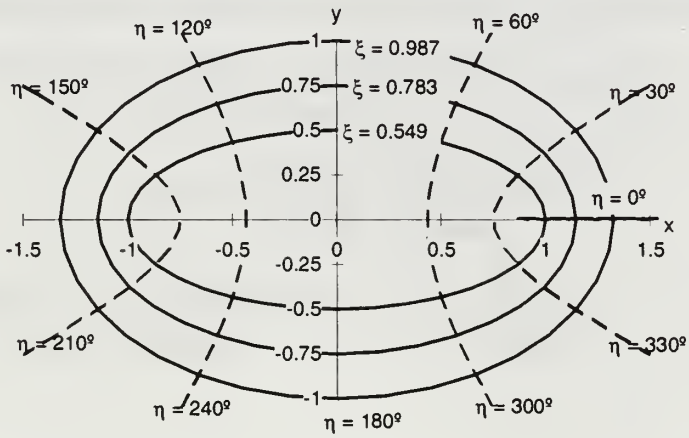

Figure 4.1. Elliptical Coordinate System.

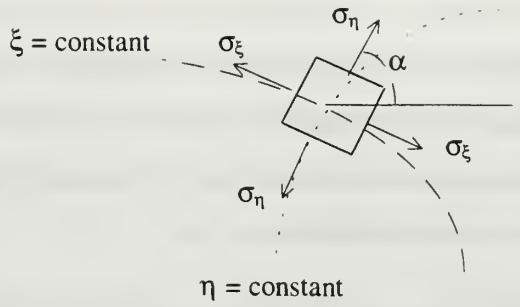

Figure 4.2. Normal Stress Components on an Element Referenced to Elliptical Coordinates.

The conversion from elliptical to Cartesian coordinates is given by:

$$\begin{aligned} x &= c\cosh\xi\cos\eta \\ y &= c\sinh\xi\sin\eta \end{aligned} \qquad (4.1)$$

where c is the focal distance of the ellipse given by:

$$c^2 = a^2 - b^2$$

The stress around the circumference of the elliptical boundary is:

$$\sigma_\eta = S\,e^{2\xi_o}\,\frac{\sinh 2\xi_o + e^{2\xi_o}\cos 2\eta - 1}{\cosh 2\xi_o - \cos 2\eta} \qquad (4.2)$$

were ζ_0 is the value of ζ at the boundary of the ellipse.

The stress components, as shown by Brown [Ref. 10], throughout the body are given as:

$$\begin{aligned} \sigma_\eta = \frac{S}{2}\Bigg[e^{2\xi_o}\Bigg(& \frac{\cos 2\eta - \cosh 2\xi_o + \cosh(2\xi - 2\xi_o)\cos 2\eta}{\cosh 2\xi - \cos 2\eta} \\ & + \frac{\sinh 2\xi_o \sinh 2\xi - \sinh 2\xi\cos 2\eta}{(\cosh 2\xi - \cos 2\eta)^2}\Bigg) \\ & + \frac{\sinh 2\xi - e^{(2\xi_o - 2\xi)}}{\cosh 2\xi - \cos 2\eta} + \frac{\sinh 2\xi(\cosh 2\xi_o + 1) - \sinh 2\xi\cos 2\eta}{(\cosh 2\xi - \cos 2\eta)^2}\Bigg] \end{aligned} \qquad (4.3)$$

and

$$\sigma_\xi = \frac{S}{2}\left[e^{2\xi_o}\left(\frac{\cos 2\eta + \cosh 2\xi_o - \cosh(2\xi - 2\xi_o)\cos 2\eta}{\cosh 2\xi - \cos 2\eta} - \frac{\sinh 2\xi_o \sinh 2\xi - \sinh 2\xi \cos 2\eta}{(\cosh 2\xi - \cos 2\eta)^2} \right) + \frac{\sinh 2\xi - e^{(2\xi_o - 2\xi)}}{\cosh 2\xi - \cos 2\eta} + \frac{\sinh 2\xi(\cosh 2\xi_o + 1) - \sinh 2\xi \cos 2\eta}{(\cosh 2\xi - \cos 2\eta)^2} \right] \quad (4.4)$$

Along the x axis, $\sigma_{\xi\eta} = 0$, $\eta = 0$, therefore $\sigma_x = \sigma_\xi$ and $\sigma_y = \sigma_\eta$. On the y axis, $\sigma_{\xi\eta} = 0$, $\eta = \pi/2$, therefore $\sigma_y = \sigma_\xi$ and $\sigma_x = \sigma_\eta$.

To approximate an infinite plate, a plate 40 inches by 40 inches with a central elliptical hole with a major axis of 1 inch and a minor axis of 0.5 inches was used. A far-field load of $S = 1000$ psi was applied. Due to symmetry, only one quarter of the block was modeled (20 inches by 20 inches). The boundary conditions required to accomplish this symmetry were zero displacement in the y direction along the x axis, and zero displacement in the x direction along the y axis. This is shown below in Figure 4.3. A

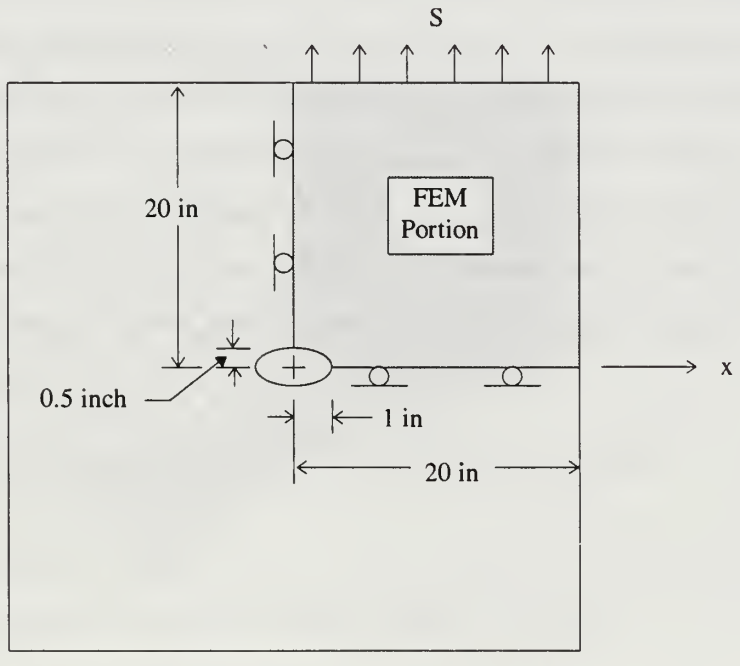

Figure 4.3 Layout of model representing an elliptical hole in an infinite plate.

mesh of 30 by 30 quadrilateral plane stress elements was used. Figures 4.4 and 4.5 below show the layout of the finite element mesh used.

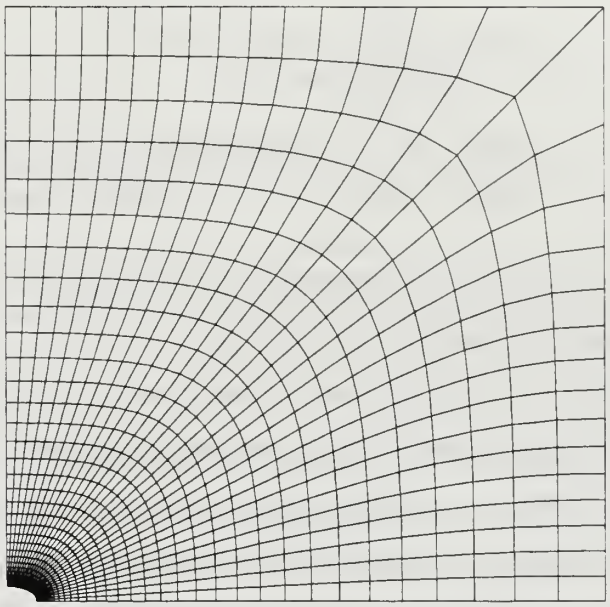

Figure 4.4. Finite element mesh for elliptical hole in an infinite plate.

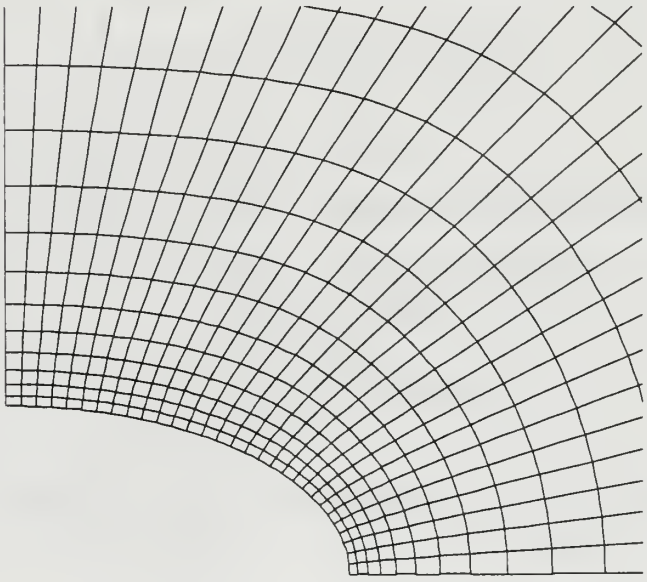

Figure 4.5. Detail of finite element mesh around elliptical hole.

Comparison of the finite element results with that of the analytical solution shows very good agreement between the two. Figure 4.6 shows the tangential stress along the

boundary of the ellipse plotted against the x-axis location. The finite element results coincide with the analytic solution across the complete boundary.

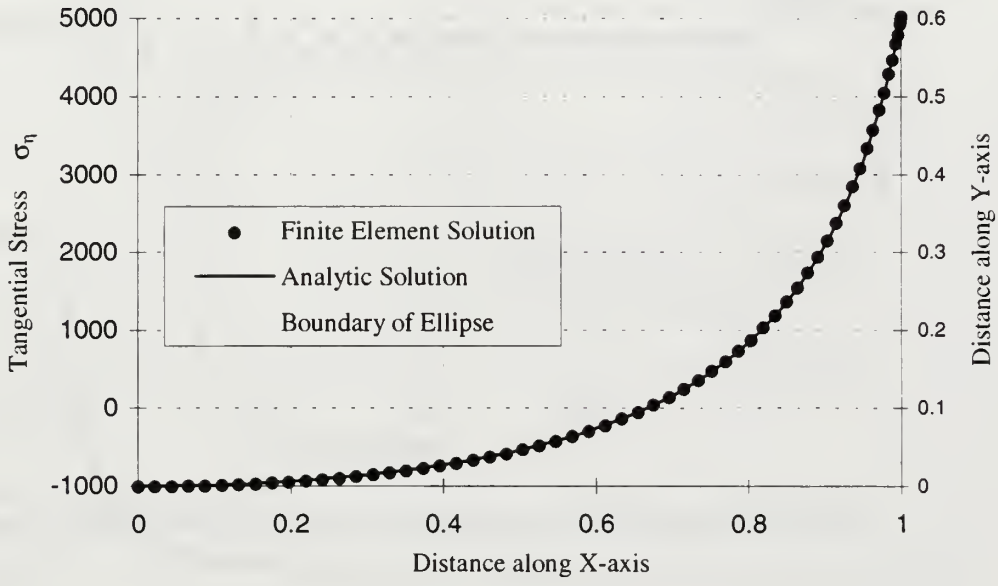

Figure 4.6. Tangential Stress σ_η Along Elliptical Boundary.

Figure 4.7 below shows the percent error from the analytic solution. The error is generally less than 1.0%, even at the point of maximum stress ($x = 1$). The greatest error occurs near the point of sign reversal ($x \cong 0.65$) and is a maximum of 7.45%. However, the stresses at this point are on the order of 5 times less than the applied far-field stresses, and the actual solution crosses zero. Therefore, a better representation of the amount of error is to normalize the difference between the finite element data and the analytic solution by the far-field stress vice the analytic solution itself, as stated in Equation 4.5. This is shown in Figure 4.8.

$$\text{Normalized Stress Error} = \frac{\sigma_{\text{Finite Element}} - \sigma_{\text{Amalytic Value}}}{S} \times 100\,\% \qquad (4.5)$$

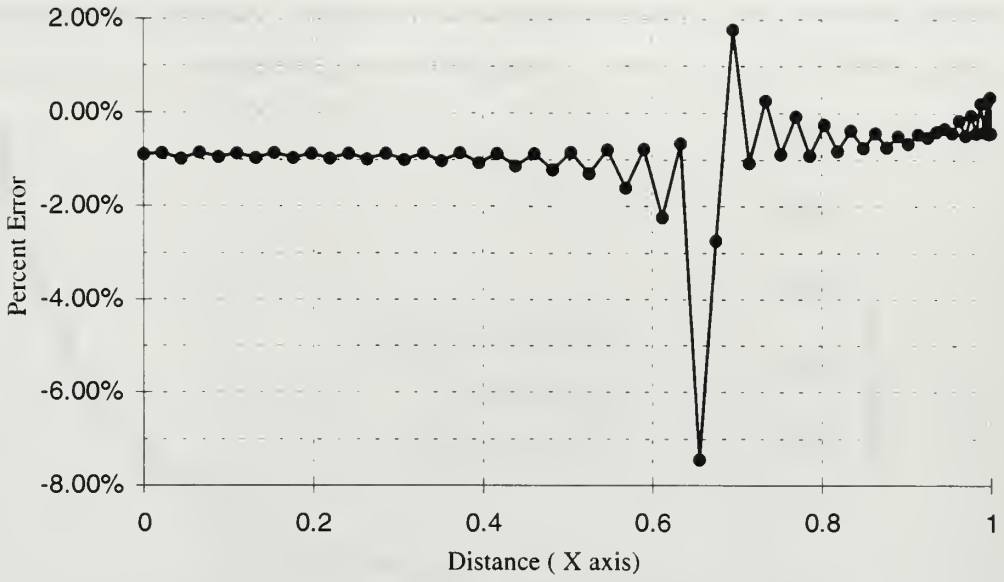

Figure 4.7 Percent Error of tangential stress σ_η along elliptical boundary.

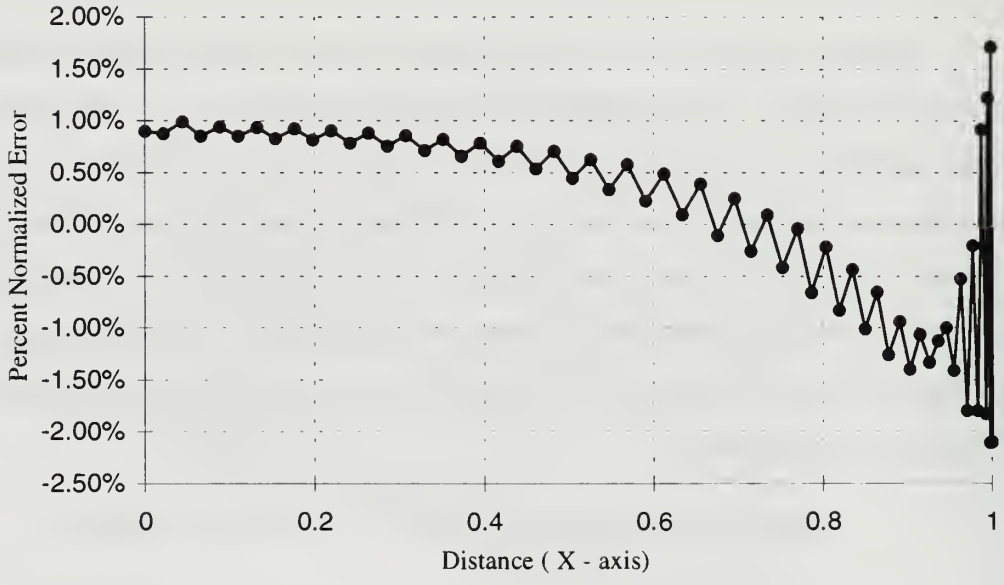

Figure 4.8 Percent Normalized Error of tangential stress σ_η along elliptical boundary.

A comparison was also made of the stress distribution along $\eta = 0$ and $\eta = \pi/2$. Figure 4.9 below shows the σ_η stress distribution along $\eta = 0$ for both the finite element calculations and the analytic solution. Very good correlation is shown, with the

maximum error at 1.23% (see Figure 4.10). Figure 4.11 below shows the σ_η stress distribution along $\eta = \pi/2$ for both the finite element calculations and the analytic solution. Again, very good agreement of the finite element method with the analytic solution was achieved. The normalized error is shown in Figure 4.12.

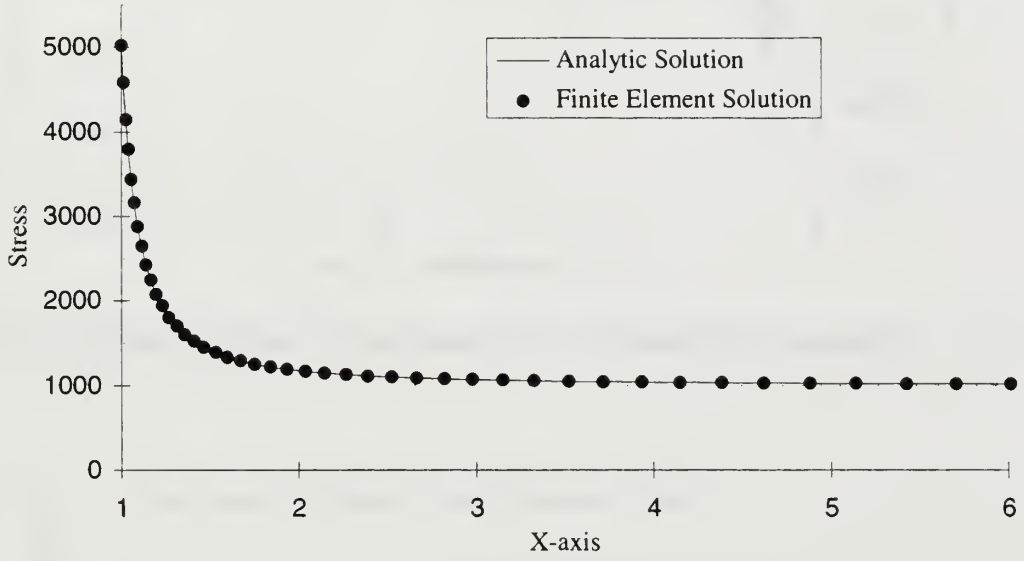

Figure 4.9. Axial stress (σ_η) along $\eta = 0$.

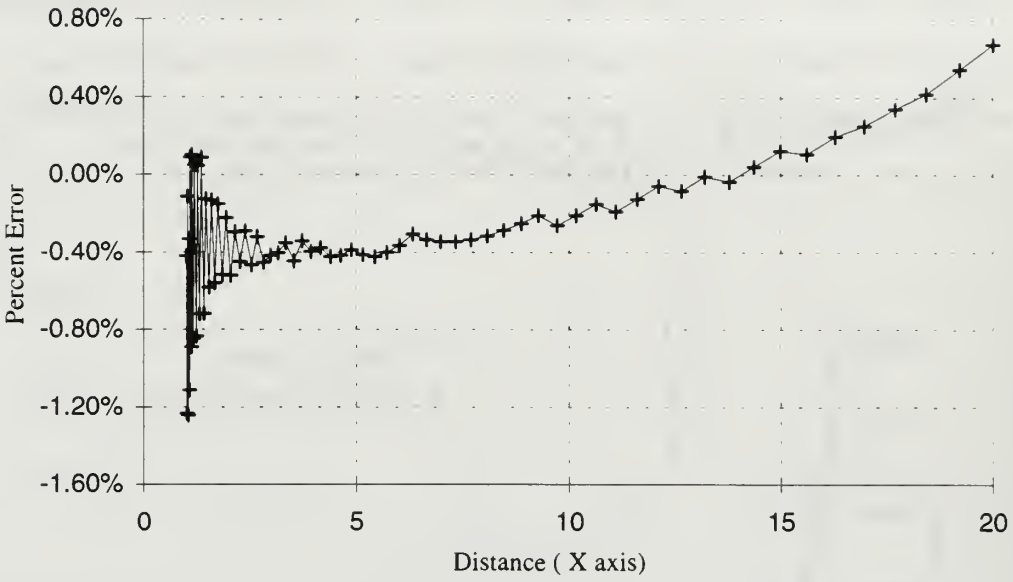

Figure 4.10 Finite Element Error of Axial Stress (σ_η) Along $\eta = 0$.

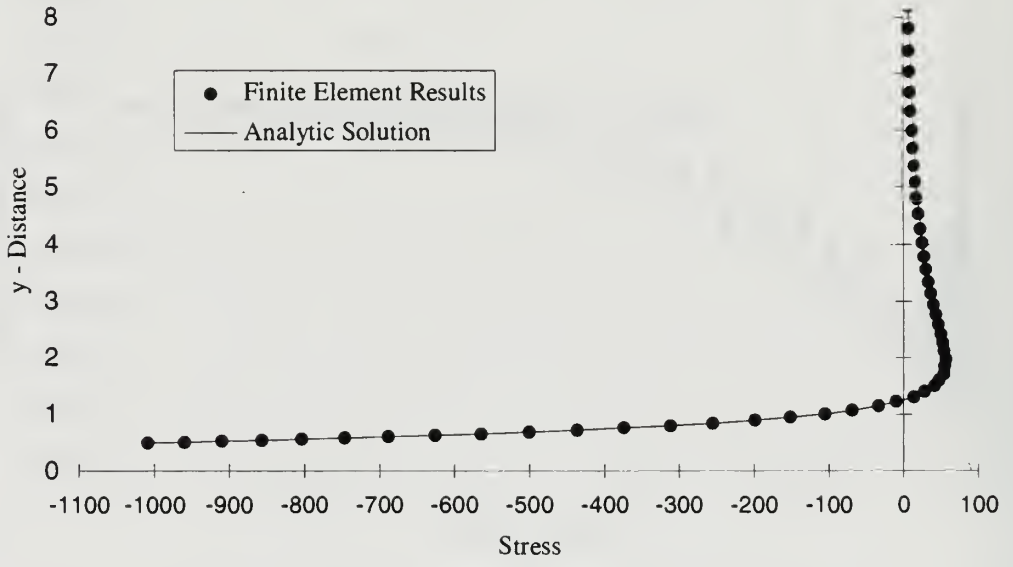

Figure 4.11 Axial Stress (σ_η) Along $\eta = \pi/2$.

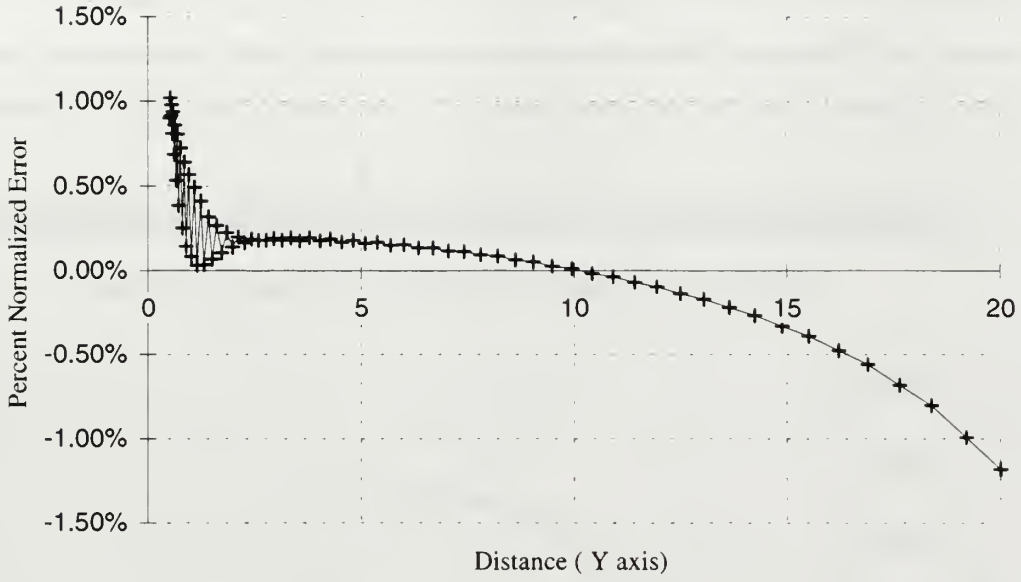

Figure 4.12. Finite Element Normalized Error of Axial Stress (σ_η) Along $\eta = \pi/2$.

2. Conclusion of Elastic Finite Element Model

The comparison of the finite element results with the analytic solution of the stress distribution around an elliptical hole shows that the IDEAS finite element program can be used to accurately analyze notch stresses under linear elastic loading. Even though the maximum error along the hole edge was 7.45%, this occurred at a point were the stresses were only 3% of the far-field applied stress. The focus of these finite element analyses was to obtain accurate stresses and strains in the vicinity of the plastic zone. Therefore, this error at the low stress regions becomes insignificant when compared to the magnitude of the applied loads and of the peak stresses.

B. VERIFICATION OF ELASTOPLASTIC FINITE ELEMENT MODEL

1. Uniaxial Test of Stress-Strain Curve

The first elastoplastic comparison of the I-DEAS™ Software was on a long narrow block to verify the input of the stress-strain curve. A finite element mesh of 3 elements

by 100 elements with the outer dimensions 1.0 m by 0.03 m, shown in Figure 4.13. This simple case illustrates that the elasto-plastic solution converges to the input stress-strain curve. Figure 4.14 shows the stress-strain curve used, along with the FEM calculations.

Figure 4.13. Finite Element Model of Uniaxial Tension.

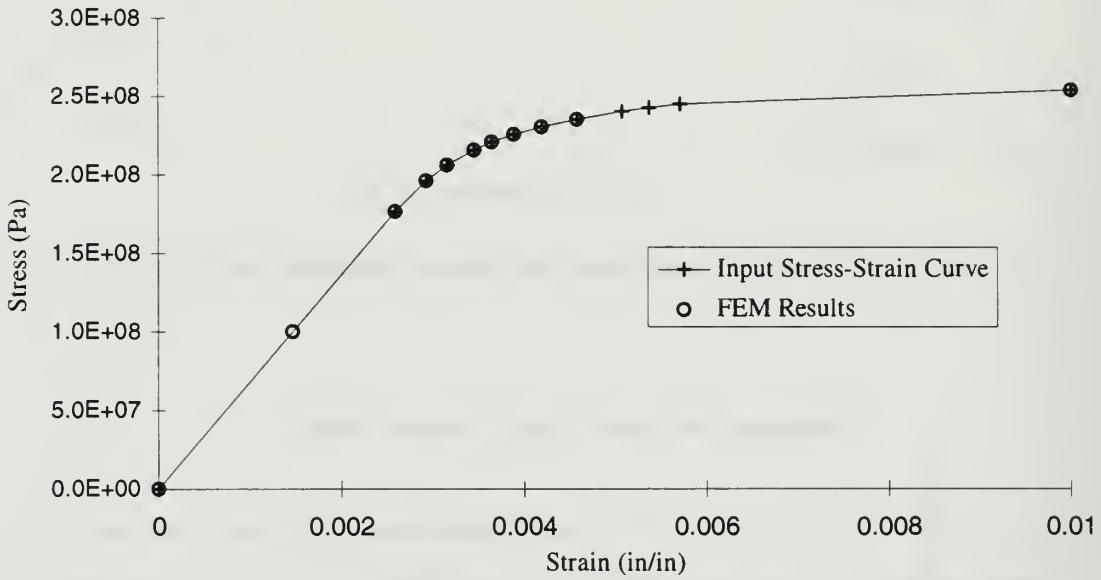

Figure 4.14. Results of Uniaxial Test Case.

2. Infinite Plate with a Circular Hole

a. Analytic Solution – Elasto-plastic Case

The elastic solution of the stress distribution of a circular hole in an infinite plate with a far-field applied load of $\sigma_r = \sigma$, as shown in Figure 4.15, can be obtained in closed form and is shown in Equation 4.6. To obtain the elasto-plastic stesses and strains, both incremental and deformation theory have been applied to this problem

$$\sigma_r = \sigma\left(1 - \frac{a^2}{r^2}\right) \qquad \sigma_\theta = \sigma\left(1 + \frac{a^2}{r^2}\right) \qquad (4.6)$$

[Ref. 11, 12, 13, and 14]. Tuba [Ref. 12] and Chakrabarty [Ref. 14] show that both these solutions are identical. The solution below is taken from Chakrabarty [Ref. 14].

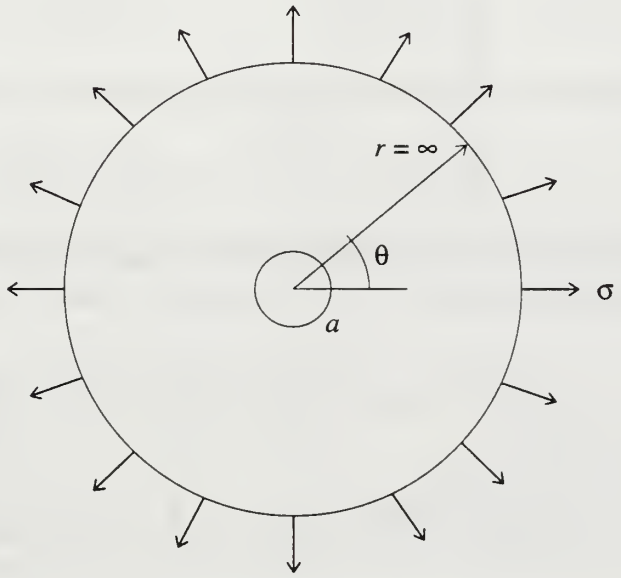

Figure 4.15 Infinite plate with circular hole

Applying the governing equations in polar form for axisymmetric loading, one obtains the stress components in terms of constant c_2 and c_3 that can be solved for the imposed boundary conditions:

$$\sigma_r = 2c_2 + \frac{c_3}{r} \qquad \sigma_\theta = 2c_2 - \frac{c_3}{r} \tag{4.7}$$

The elastic solution shows that at the hole edge, σ_θ is twice the far-field value σ, with all other components being zero. From the von Mises yield criteria, Equation 4.8, yielding will occur once σ is greater than one half of the yield stress σ_0, and a region of plastic deformation will extend from the edge of the hole out to a certain radius of $r > a$. If the radius of the elastic/plastic boundary is given as c then the boundary conditions for Equation 4.7 are $\sigma_r = \sigma_{rc}$ at $r = c$ and $\sigma_r = \sigma$ at r = ∞, where σ_{rc} is the yet to be determined value of the radial stress at the elastic/plastic boundary.

$$\sigma_0^{\,2} = \sigma_\theta^{\,2} - \sigma_\theta \sigma_r + \sigma_r^{\,2} \tag{4.8}$$

The constant c_3 in Equation 4.7 can now be solved for in terms of σ_0 and c, and the stresses in the elastic region reduce to:

$$\sigma_r = \sigma - \frac{\sigma_0 c^2}{\sqrt{3}\, r^2}\sqrt{1-\frac{\sigma^2}{{\sigma_0}^2}} \qquad \sigma_\theta = \sigma + \frac{\sigma_0 c^2}{\sqrt{3}\, r^2}\sqrt{1-\frac{\sigma^2}{{\sigma_0}^2}} \tag{4.9}$$

In the plastic region, the Von Mises stresses can be expressed in parametric form as:

$$\sigma_r = \frac{2}{\sqrt{3}}\sigma_e \sin\phi \qquad \sigma_\theta = \frac{2}{\sqrt{3}}\sigma_e \cos\left(\frac{\pi}{6}-\phi\right) \tag{4.10}$$

The stress-strain constitutive relationships given in Equation 3.18 are restated in polar form:

$$\begin{aligned}
\varepsilon_r &= \frac{1}{E}\left(\sigma_r - \nu\sigma_\theta\right) + \frac{3}{2}\left(\frac{1}{E_s^t}-\frac{1}{E}\right)\left[\sigma_r - \frac{1}{3}\left(\sigma_r+\sigma_\theta\right)\right] \\
\varepsilon_\theta &= \frac{1}{E}\left(\sigma_\theta - \nu\sigma_r\right) + \frac{3}{2}\left(\frac{1}{E_s^t}-\frac{1}{E}\right)\left[\sigma_\theta - \frac{1}{3}\left(\sigma_r+\sigma_\theta\right)\right]
\end{aligned} \tag{4.11}$$

The plastic secant modulus has been rewritten as follows:

$$\frac{1}{E_s} = \frac{\varepsilon_e^p}{\sigma_e} = \frac{\varepsilon_e^t - \varepsilon_e^e}{\sigma_e} = \frac{1}{E_s^t} - \frac{1}{E}$$

were E_s^t is the secant modulus of the total stress-strain curve. The solution of the stresses is independent of the elastic Poisson's ratio, ν, and therefore this can be set equal to 0.5. This transform simplifies the constitutive relations, while allowing solution for the correct stress values [Ref. 13]. With this simplification, and the substitution of the definition of the secant modulus as the ratio of the effective stress to the effective total strain, the stress-strain relations in the plastic region can be expressed as:

$$\bar{\varepsilon}_r = \varepsilon_e \sin\left(\phi - \frac{\pi}{6}\right) \qquad \bar{\varepsilon}_\theta = \varepsilon_e \cos\phi \tag{4.12}$$

where $\bar{\varepsilon}_r$ and $\bar{\varepsilon}_\theta$ are the strain values for an incompressible material ($\nu = 0.5$). Once the stresses have been found, then the actual strains can be found using Equation 4.11 and the correct value for Poisson's ratio ν.

The strain ε_e is related to the equivalent stress σ_e by Equation 3.23, or a similar stress-strain curve. Another such empirical relationship that can be used is a modified Ludwick curve [Ref. 14], which is separated into an elastic and a plastic range:

$$\sigma = \begin{cases} E\varepsilon & \varepsilon < \dfrac{\sigma_0}{E} \\ \sigma_0 \left(\dfrac{E\varepsilon}{\sigma_0} \right)^n & \varepsilon \geq \dfrac{\sigma_0}{E} \end{cases} \qquad (4.13)$$

A plot of a family of curves of this form is shown below in Figure 4.16, where σ_0 = 30,000, E = 30.0×10^6, and n varies from 0 to 0.5. At the elastic/plastic boundary, the

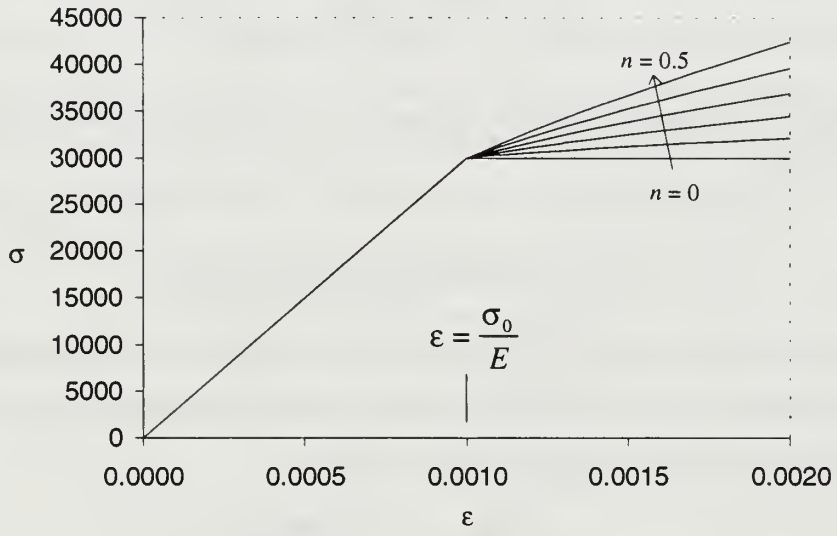

Figure 4.16 Modified Ludwick Stress-Strain Curve.

auxiliary angle ϕ is found by setting the radial component of the stress in Equation 4.9 equal with the radial stress component in Equation 4.10. The substitution of $r = c$, and $\sigma_e = \sigma_0$ results in:

$$\phi_c = \sin^{-1}\left(\frac{\sqrt{3}\sigma}{2\sigma_0} - \frac{1}{2}\sqrt{1 - \frac{\sigma^2}{\sigma_0^2}} \right) \qquad (4.14)$$

When stresses in Equation 4.10 are substituted into the equilibrium condition, the result is:

$$\frac{1}{\sigma_e}\frac{\partial \sigma_e}{\partial r}\tan\phi + \frac{\partial \phi}{\partial r} = \frac{1}{2r}\left(\sqrt{3} - \tan\phi\right) \qquad (4.15)$$

Likewise, when the strains in Equation 4.12, along with the stress-strain law of Equation 4.13, are substituted into the compatibility equation, the result is:

$$\frac{1}{\sigma_e}\frac{\partial \sigma_e}{\partial r} = n\tan\phi\frac{\partial \phi}{\partial r} + \frac{n}{2r}\left(\sqrt{3}\tan\phi - 3\right) \qquad (4.16)$$

The relationship between the auxiliary angle ϕ , r, and n (material constant from Equation 4.13) can now be found by eliminating the equivalent stress from Equations 4.15 and 4.16. The resulting differential equation is:

$$r\frac{\partial \phi}{\partial r} = \frac{\left(\sqrt{3} - \tan\phi\right)\left(1 + \sqrt{3}\ n\tan\phi\right)}{2\left(1 + n\tan^2\phi\right)} \qquad (4.17)$$

The solution to this can be solved by separation of variables, and can be reduced to r as function of ϕ:

$$\frac{a^2}{r^2} = \frac{1}{\sqrt{3}}\left(\sqrt{3}\cos\phi - \sin\phi\right)\left(\cos\phi + \sqrt{3}\,n\cos\phi\right)^{\frac{-4n}{1+3n^2}} e^{\left(-\sqrt{3}\frac{1-n^2}{1+3n^2}\phi\right)} \qquad (4.18)$$

The equivalent stress must also be found, and this is obtained by eliminating the radius from Equations 4.15 and 4.16. The resulting differential equation leads to the solution of the equivalent stresses as a function of ϕ, n, and σ:

$$\frac{1}{\sigma_e}\frac{\partial \sigma_e}{\partial \phi} = -n\left(\frac{\sqrt{3} - \tan\phi}{1 + \sqrt{3}\,n\tan\phi}\right) \qquad (4.19)$$

The relationship between ϕ and σ_e is now found as:

$$\sigma_e = K_t\sigma\left(\cos\phi + \sqrt{3}\,n\sin\phi\right)^{-n(1+3n)/\left(1+3n^2\right)} e^{\left(-\sqrt{3}\frac{n(1-n)}{1+3n^2}\phi\right)} \qquad (4.20)$$

The stress concentration factor is obtained by setting $\phi = \phi_c$ and thus $\sigma(\phi) = \sigma_0$ in Equation 4.20:

$$K_t = \frac{\sigma_0}{\sigma}\left\{(1+3n)\frac{\sigma}{2\sigma_0} + \frac{\sqrt{3}(1-n)}{2}\sqrt{1 - \frac{\sigma^2}{{\sigma_0}^2}}\right\}^{\frac{n(1+3n)}{1+3n^2}} e^{\sqrt{3}\frac{n(1-n)}{1+3n^2}\phi_c} \qquad (4.21)$$

For a given applied load of $\sigma_r = \sigma$, the plastic stresses in Equation 4.10 can be obtained by first solving for ϕ_c and K_t as given in Equations 4.14 and 4.21. The auxiliary angle ϕ in Equation 4.18 is solved for a given radius by an iterative method. Finally σ_e is solved from Equation 4.20, which is then substituted into Equation 4.10 to solve for the component stresses. For a work-hardening material ($n \neq 0$), the strains are then found by Equation 4.11.

b. Analytic Calculations

Two cases were solved analytically to be used with comparison to the finite element solution. The first involved an elastic perfectly plastic material that matched that used by Davis [Ref. 11] for his numerical results using incremental theory. The second case used the same elastic properties but changed the plastic property to a work hardening material. Table 4-1 below shows the material properties:

Material Constant	Value
σ_0	30,000
E	30×10^6
ν	0.3
σ	22,500
n, Case 1	0
n, Case 2	0.25

Table 4-1 - Material Properties of Infinite Plate with hole

For the two separate cases, the calculated values of ϕ_c, c, and K_t are listed below. Figure 4.17 shows a plot of Equation 4.18 for the two cases. Note that there are two solutions shown, and care must be taken to ensure that the correct root is solved for. The mathematical software Maple V® was used to solve ϕ for each input radius. This program allows the analyst to limit the range in which to search for a solution, and therefore only solutions for $0 < \phi < 60°$ were obtained without any difficulty. Once ϕ was found for a specific radius, the calculations of σ_e, followed by σ_r and σ_θ, was straight forward.

Maple V® was programmed to make all these calculations at a radial distance corresponding to each node location along the x-axis.

Variables	Case 1 ($n = 0$)	Case 2 ($n = 0.25$)
ϕ_c	0.32446	0.32446
c	1.51550	1.47886
K_t	1.3333	1.50195

Table 4-2 Solution Variables for Case 1 and Case 2.

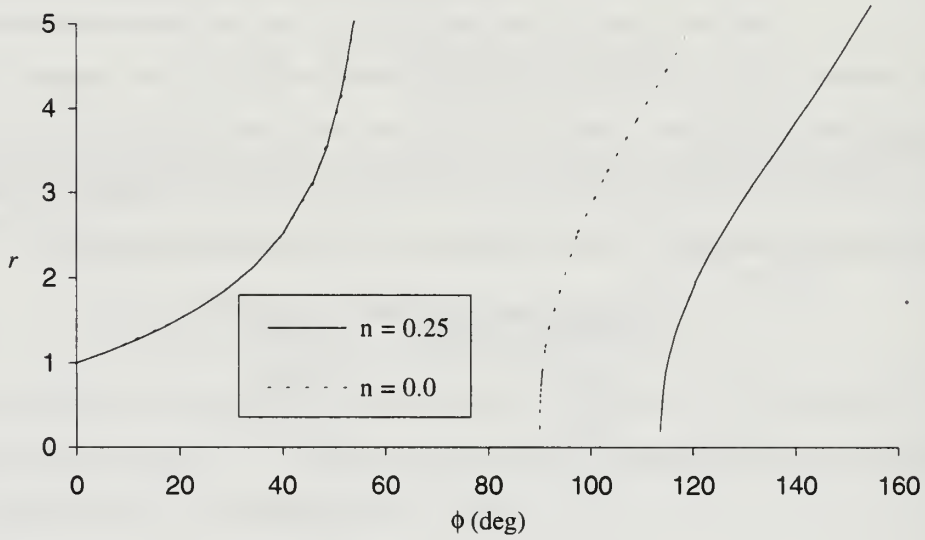

Figure 4.17 Solution of Equation 4.18.

c. Finite Element Solution

The infinite plate with a circular hole was modeled using a 60 degree section on an annulus with a inner hole radius of $a = 1.0$ and an outer radius of 30. Due to the axisymmetric loading, a variety of finite elements are available that would efficiently model the axisymmetric problem; however, the above geometry with quadrilateral plane stress elements was used in order to verify these elements and the I-DEAS™ software for more general notched geometries.

The first step was to determine beyond what mesh sizing the solution was mesh independent. Three separate meshes as listed in Table 4-3 were analyzed and are

shown in Figures 4.18 and 4.19. The coarse and medium element meshes each used equal numbers of elements on opposite sides of the geometry, while the fine mesh had one row of elements at the outermost radius that split into a finer meshing using triangular elements. This was possible since both the radial and cicumferential stresses rapidly approach the far-field value, and for the load used, reaches within 2% of the far-field value at a radial distance of 7.5a and within 0.5% of the far-field value at 15.13a. The finite element model extends radially to 30a, hence there is little gradient in the stresses and strains beyond a radial distance of 15a.

Mesh	Elements	Nodes
Coarse	200	661
Normal	800	2,521
Fine	1378	4,247

Table 4-3. Mesh sizes for hole in infinite plate.

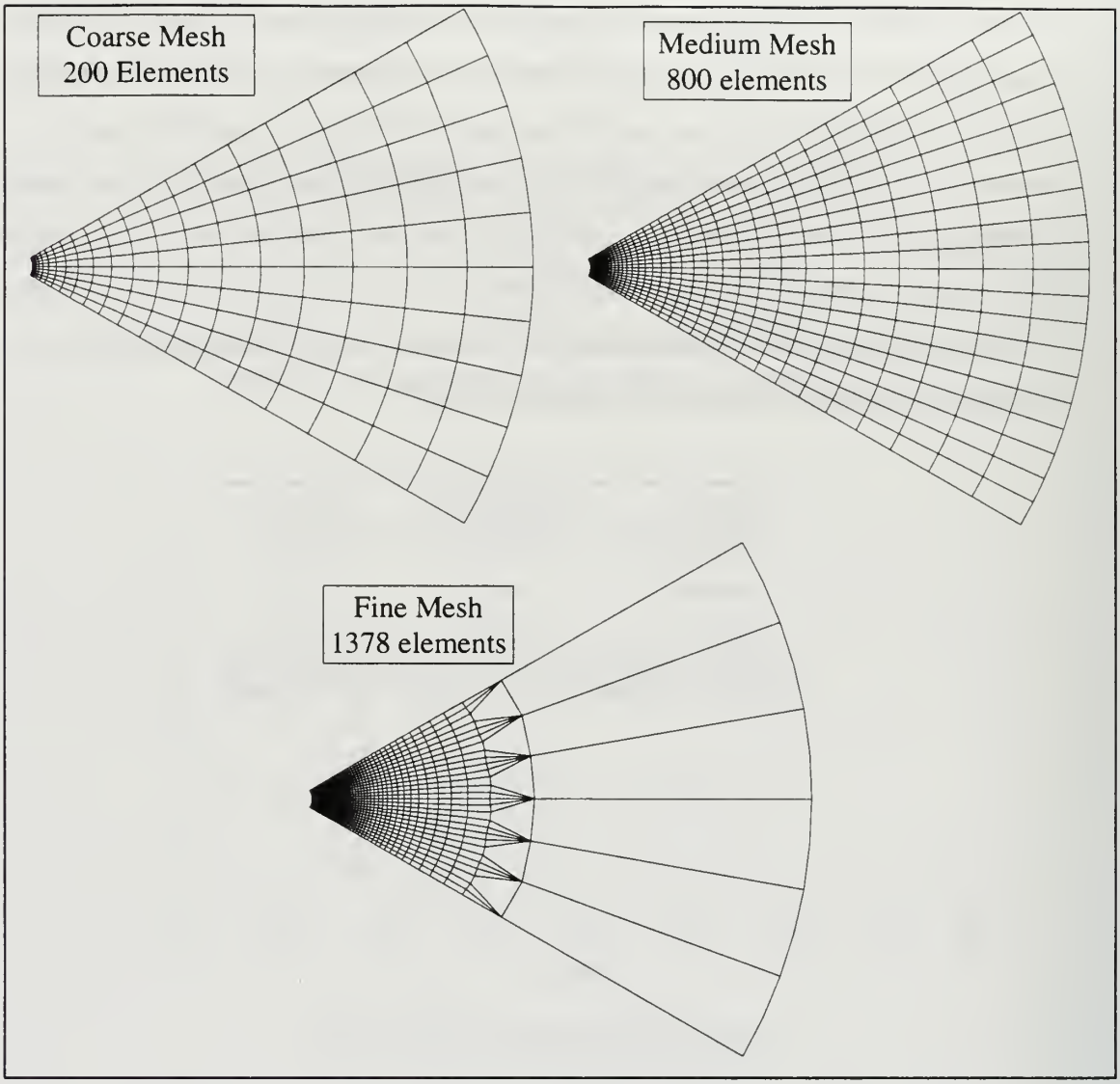

Figure 4.18. Layout of Element Meshes for Hole in an Infinite Plate.

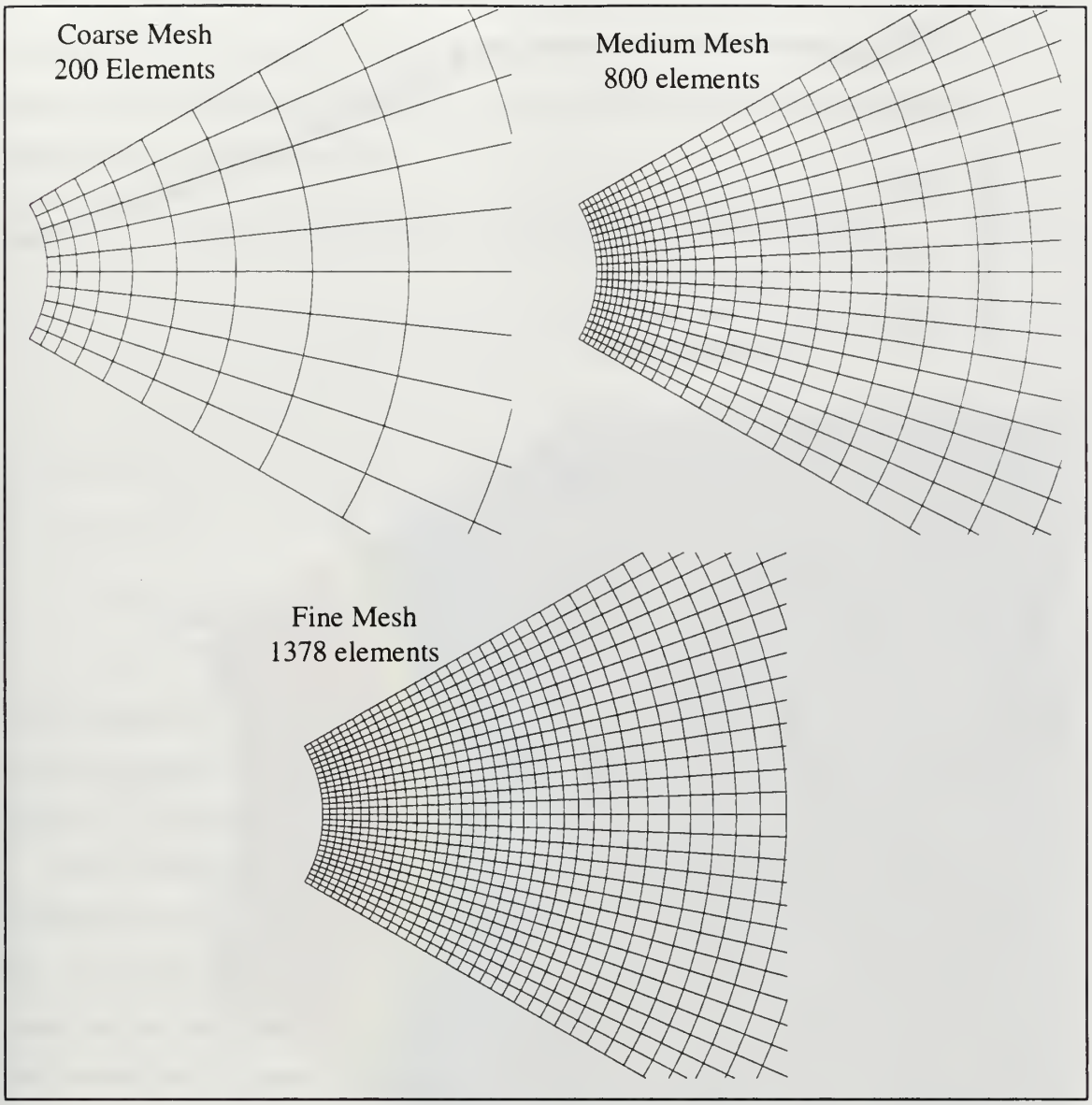

Figure 4.19. Exploded Views of Element Meshes Near Hole Boundary.

The results of the mesh comparisons is shown in Figure 4.20. The mesh refinement results in only a slight change in the solution, particularly at the elastic/elasto-plastic boundary. The solution change from the medium to fine mesh is insignificant, and it can be concluded that the 20 by 40 element mesh provides a result that will not improve significantly with an increase in the mesh density. For the rest of the comparisons to the analytic solution, only the 20 by 40 element mesh will be used.

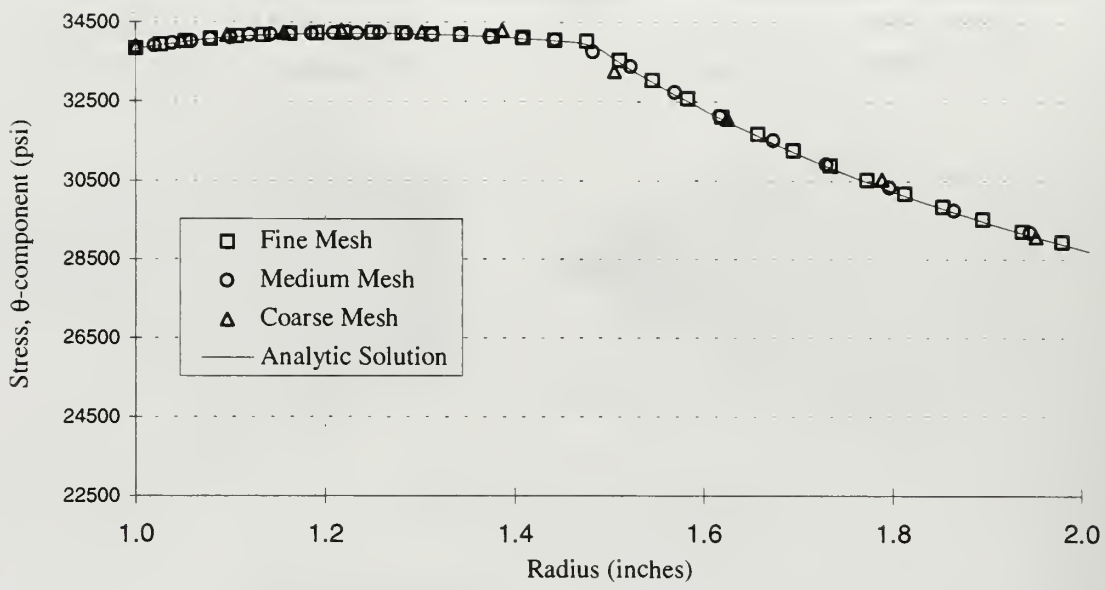

Figure 4.20 Circumferential stress for various mesh sizes.

The results of the FEM were taken along the one line of elements at $\theta = 0$. As would be suspected, the angular change in the FEM solution was insignificant, as shown in Figure 4.21, which shows the effective stress distribution throughout the finite element model. The radius of the elastic/plastic boundary, *c*, corresponding to an effective stress of 30,000 psi, was interpolated between nodal points to be 1.5185 inches for case one, and 1.5107 for case two, with the analytic values listed in Table 4-2. This is an error of only 0.2% for the former case, and 0.59% for the later. Note that the finite element value is linearly interpolated, and though the nodal values may be correct, this in itself will introduce a slight error.

For both case one and case two, the finite element solution was found to match the analytic solution very well. Figure 4.22 shows the finite element stresses with the analytic curves superimposed for the perfectly plastic model (case 1). The normalized error was less than 1% for each data point (see Figure 4.23). The stress distributions for case 2 are shown in Figure 4.24. Again, very good agreement is made with the analytic solution, and the normalized error remains less than 1% for the work hardening material (see Figure 4.25). For the elastic/perfectly-plastic model, the strains in the plastic region cannot be obtained analytically. However, for case 2, one simply solves Equation 4.11.

The strain distribution for case 2 is shown in Figure 4.26. As in the case of the stresses, the finite element method produces very accurate results. The error was normalized with respect to (*S*/*E*) as shown in Equation 4.22 for the same reason the stress error was normalized in the preceding section.

$$\text{Normalized Strain Error} = \frac{\varepsilon_{\text{Finite Element}} - \varepsilon_{\text{Analytic Value}}}{(S/E)} \times 100\% \qquad (4.22)$$

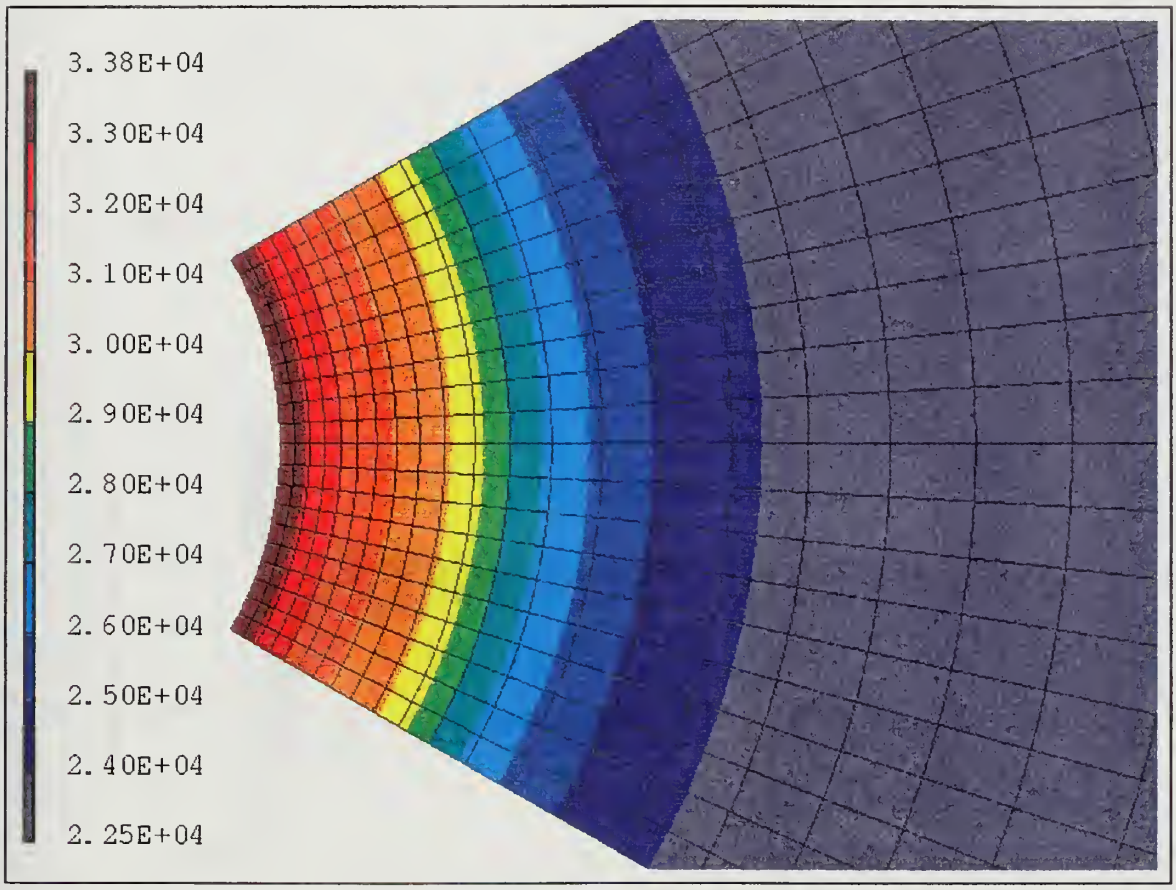

Figure 4.21. Effective Stress for Case 2.

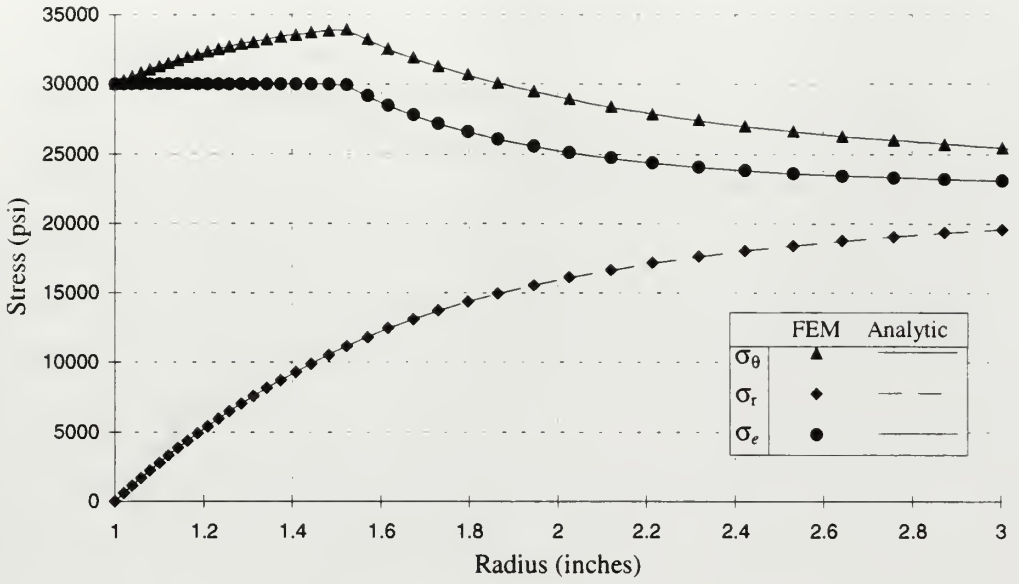

Figure 4.22. Comparison of FEM stresses with analytic solution for case 1.

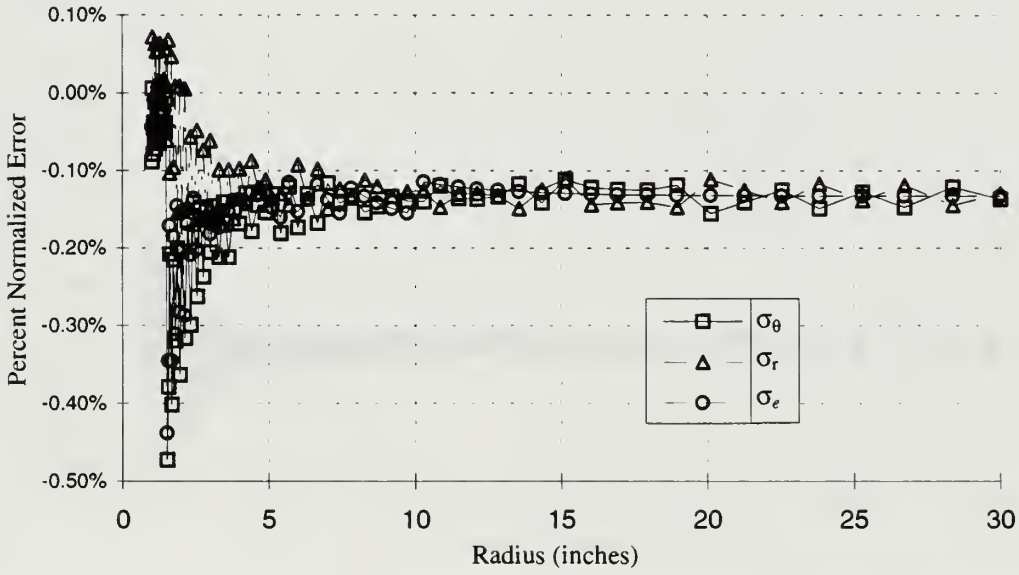

Figure 4.23. Normalized error of FEM stresses versus analytic solution for case 1.

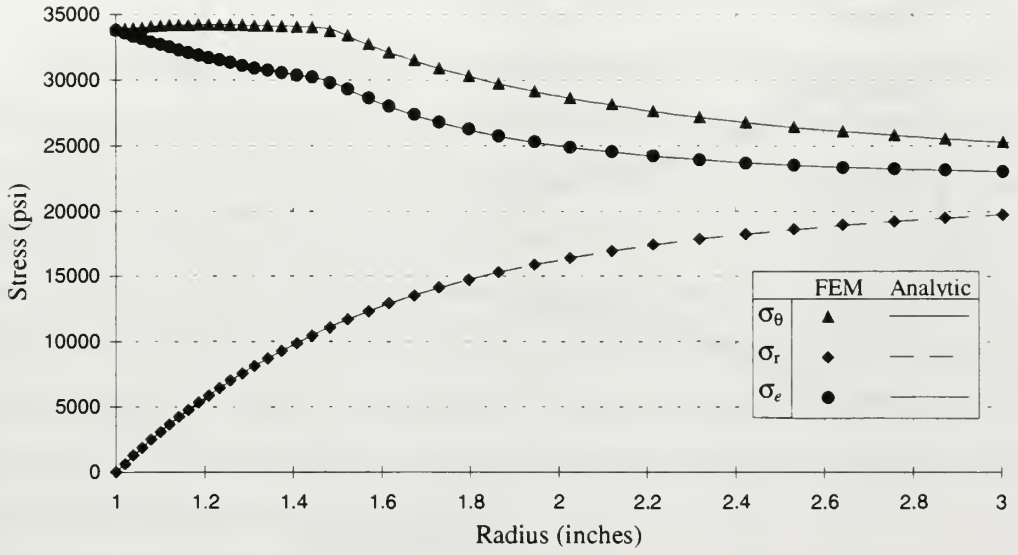

Figure 4.24. Comparison of FEM stresses with analytic solution for case 2.

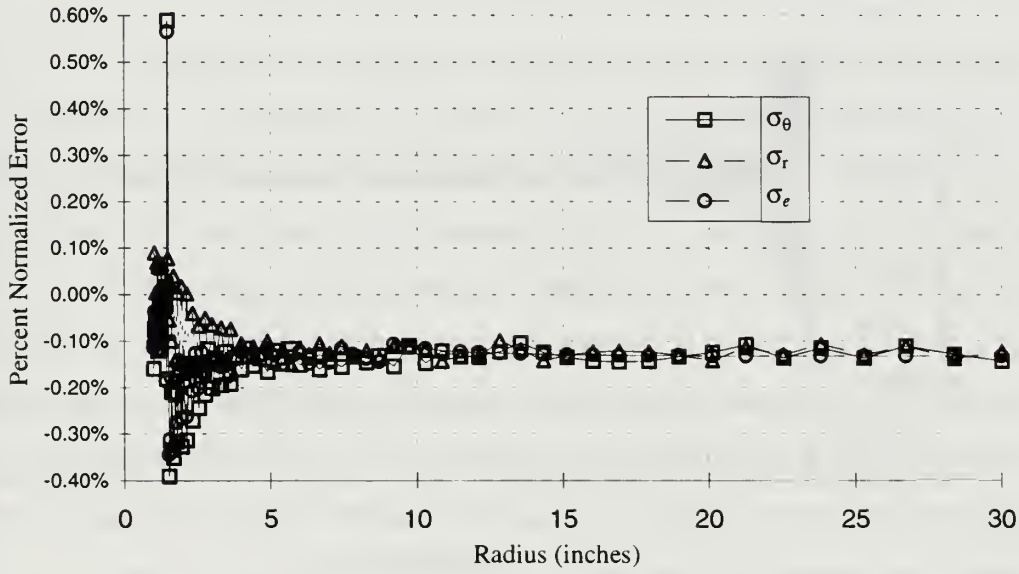

Figure 4.25. Normalized error of FEM stresses versus analytic solution for case 2.

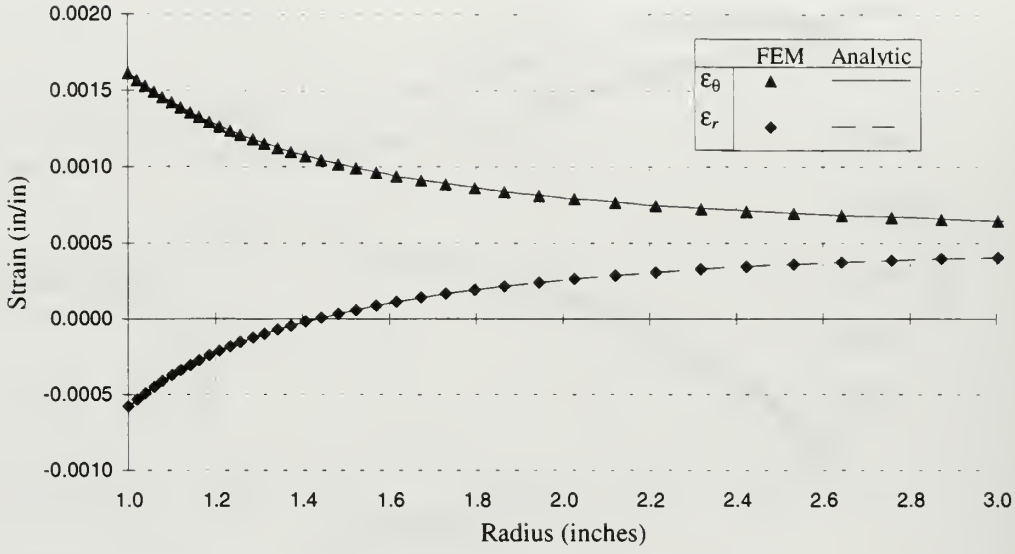

Figure 4.26. Comparison of FEM strains with analytic solution for case 2.

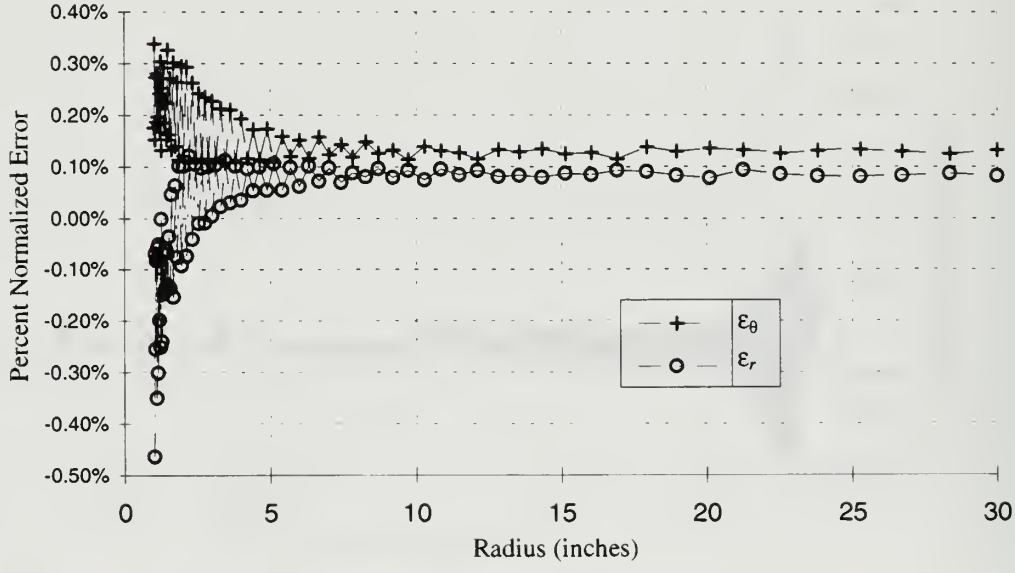

Figure 4.27. Normalized error of FEM strains versus analytic solution for case 2.

d. Conclusion on the Accuracy of the Finite Element Method

Comparisons of the I-DEAS Master Series™ finite element program to the specific problems shown reveal the excellent results obtainable for both linear and non-linear analysis by the finite element method. The differences between the finite element calculations with exact analytic solutions for both stress and strain calculations were minimal, even in regions of high gradients. It was also shown that a mesh-independent solution was readily obtainable after one or two mesh refinements. From these results of the application of the I-DEAS Master Series™ program to model problems, follow-on finite element analyses for notch geometries were performed with a very high degree of confidence in the accuracy of the solutions.

3. Comparison to Experimental Data

a. Finite Element Modeling of Experimental Specimen

Although the availability of recently published full-field stress data for basic notched and hole specimens under tensile loads is slim to non-existent, several works were completed more than thirty years ago using photoelastic techniques. Two notable works are from Durelli and Sciammarella [Ref. 15] and Theocaris and Marketos [Ref. 17]. A comparison to the Theocaris and Marketos experiment was chosen vice the Durelli and Sciammarella due to the fact that Theocaris and Marketos were able to show the maximum peak tensile stresses progressing away from the notch root. This peak σ_y stress progression occurs due to a multi-axial stress state and given stress distributions allowing for a higher σ_y stress before yielding occurs. This was also the result of all the finite element analyses completed. The test specimens used by Theocaris and Marketos were two sheets of aluminum alloy 57S, one with a hole diameter to width ratio of 1/2, the other 1/3. The later ratio of 1/3 was chosen, and the dimensions are shown below in Figure 4.28.

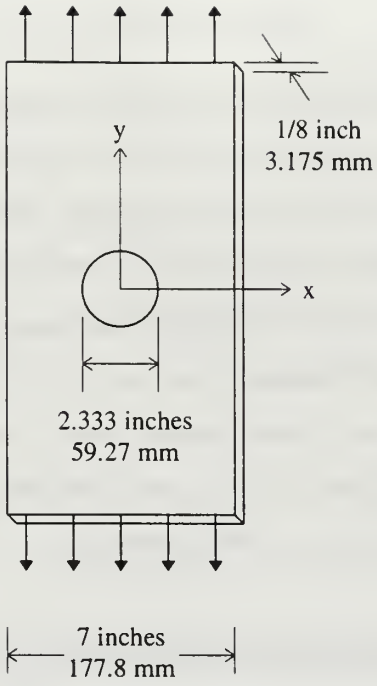

Figure 4.28. Dimensions of Plate with a Central Hole, [After Ref. 17].

The stress-strain curve of the Aluminum alloy 57S as given by Theocaris and Marketos [Ref. 17] is shown in Figure 4.29, with a curve fit to the Ramberg-Osgood equation resulting in the coefficients listed in Table 4-4.

Coefficient	Value
E (kg/mm^2)	7,000
K (kg/mm^2)	33.1
n	0.048

Table 4-4 Ramberg-Osgood Material Coefficients for Aluminum 57S.

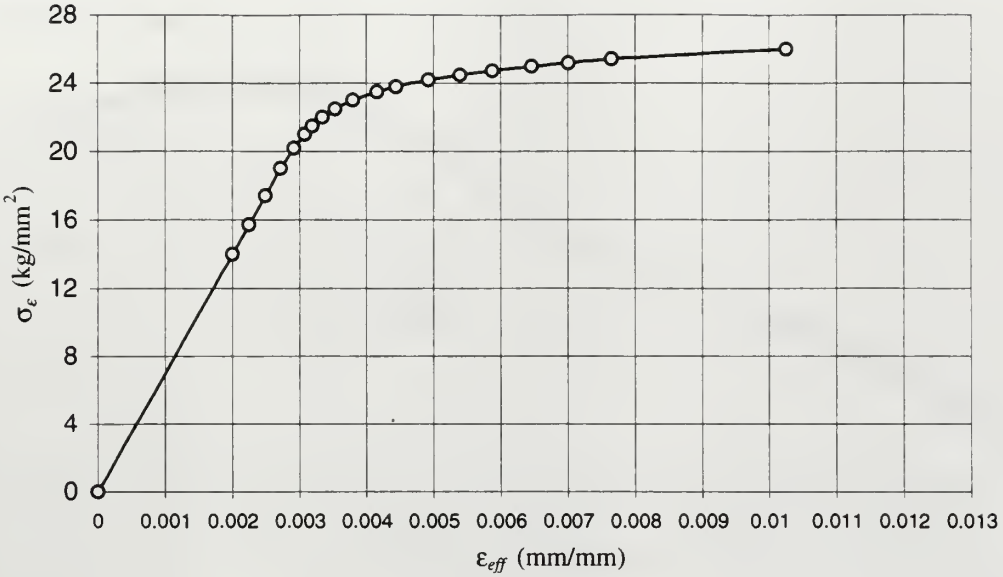

Figure 4.29. Equivalent Stress-Strain Curve for Aluminum 57S, [After Ref. 17].

The first step, as in the case of the model of the hole in an infinite plate, was to determine at what mesh density mesh independence was achieved. Three separate meshes were generated and analyzed: a 20 by 20 mesh, a 30 by 30 mesh, and a 40 by 40 mesh. These are shown in Figure 4.30. Figure 4.31 shows the y-component of stress for a load well into the plastic range. The change in the FEM stresses from the 30 by 30 mesh to the 40 by 40 mesh are insignificant, hence the 30 by 30 mesh will be used for the comparison to the experimental data.

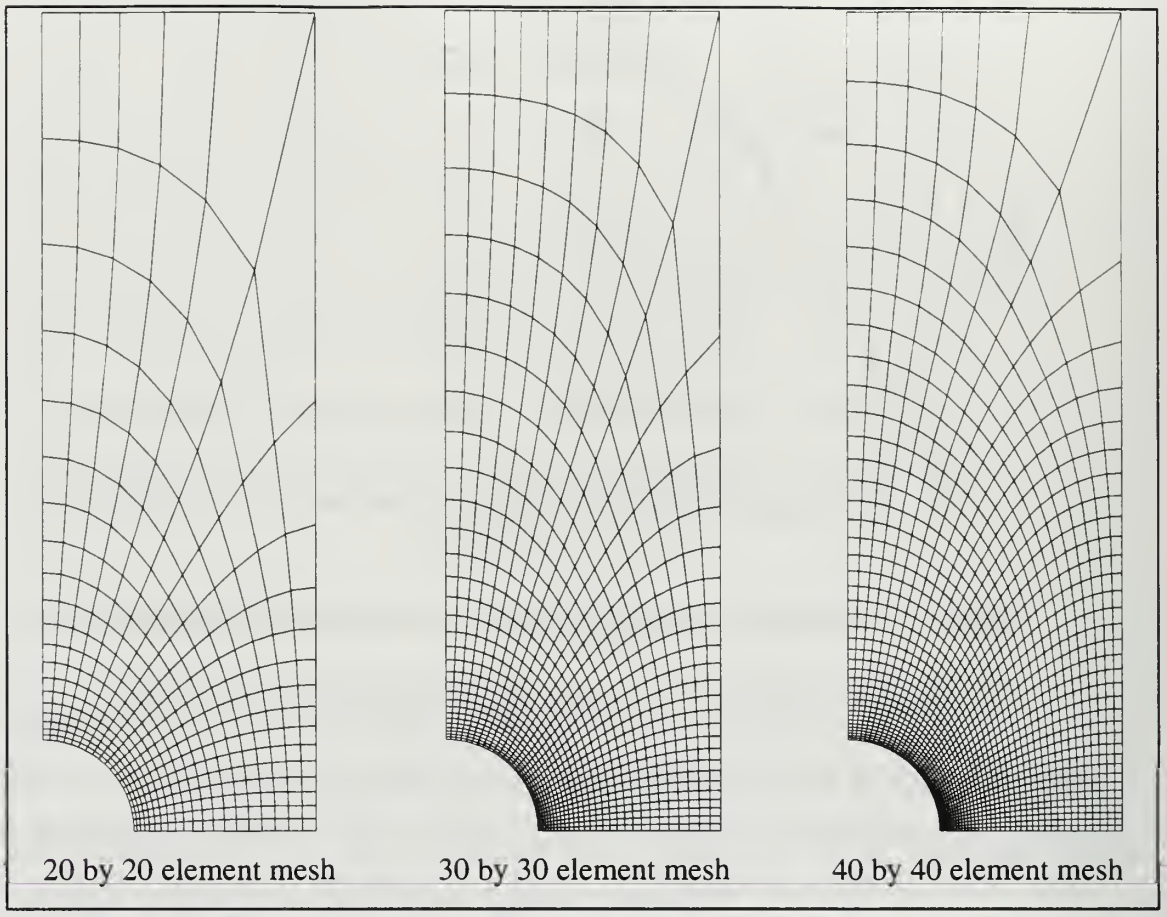

Figure 4.30. Comparison of Finite Element Mesh Sizes for a Hole in Finite Width Strip.

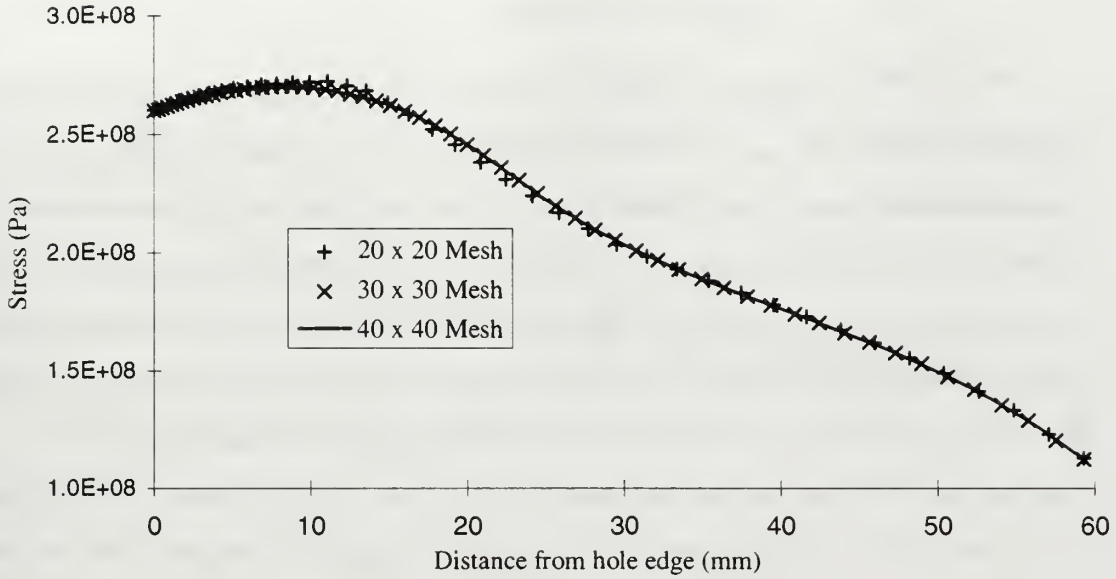

Figure 4.31. Distribution of σ_y for Various Mesh Sizes.

Table 4-5 shows the applied loads used by Theocaris and Marketos. The first load resulted in the initial onset of plastic deformation, while the last load creates a plastic zone that extends a distance 3/4 of the hole radius from the edge of the hole and covering approximately 1/3 of the minimum cross section.

Load Set	Applied Force (N)	S (MPa)	S_{NET} (MPa)
I	19162.97	67.89	101.84
II	21384.95	75.76	113.65
III	25520.79	90.42	135.63
IV	30399.66	107.70	161.55
V	34286.34	121.47	182.21
VI	38926.48	137.91	206.87

Table 4-5. Load history for Theocaris Photoelastic Experiment, [Ref. 17].

b. Finite Element Results

A comparison of the σ_y stress was made for all six load sets, and these are shown in Figures 4.32 and 4.33. Several differences are noticeable between the FEM results and the Theocaris and Marketos data. First, although Theocaris and Marketos show a peak σ_y stress that progresses inward as the plastic deformation increases, they also show that it initially decreases before reaching a maximum for the last three applied loads. The FEM shows that the maximum value of σ_y moves away from the hole edge, but it also shows that σ_y constantly increases until it peaks. The second difference between the FEM and the Theocaris and Marketos data is the magnitude of the decrease in σ_y near the edge opposite the hole. This results in significant disagreement between the two values, approaching an 80% difference for the first applied load. Figure 4.34 shows the difference between the FEM calculations and the experimental data. One test of the accuracy of both results is to determine if equilibrium has been satisfied at the minimum cross section. The stress distribution curves were numerically integrated to determine the resulting force. These results are listed in Table 4-6. The values are only for half of the plate, hence the total applied force will be twice these values. Even though these calculations are only approximate, it is easily seen that the FEM has satisfied equilibrium, while the Theocaris and Marketos results have underestimated the stress distribution for the first three load sets. It should also be noted that the photoelastic analysis shows fringes in the regions of strain gradients, and since this is a region of relatively uniform stress and strain, the accuracy of the method degrades.

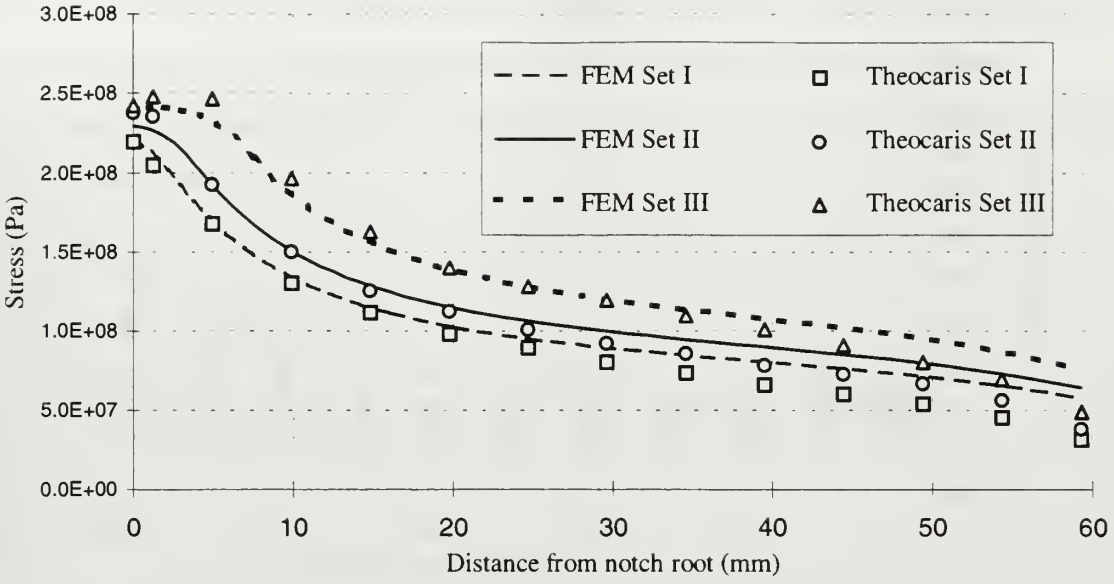

Figure 4.32. Distribution of σ_y for Theocaris model, load sets I to III.

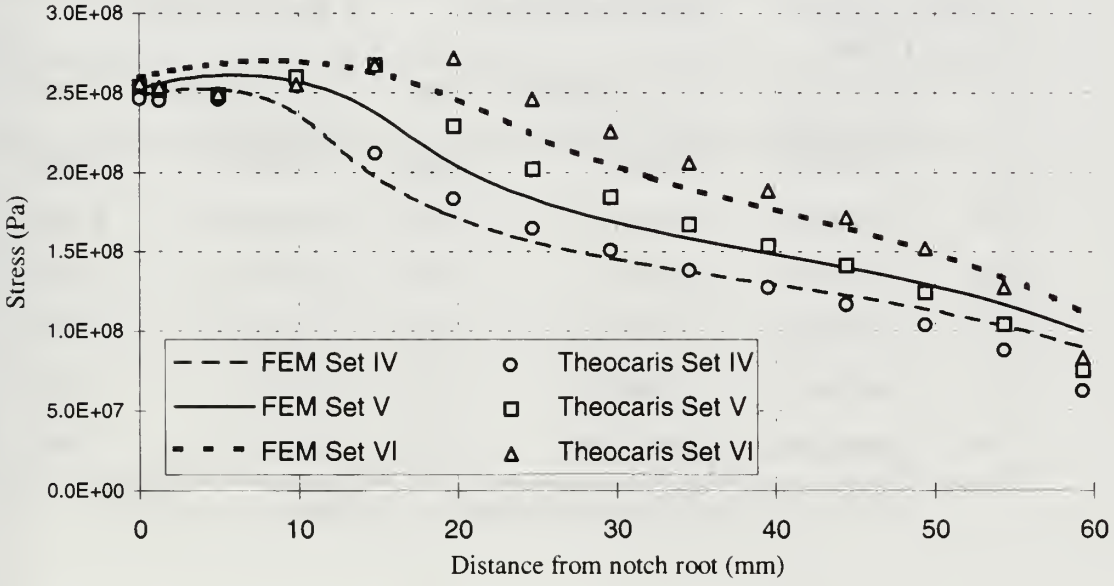

Figure 4.33. Distribution of σ_y for Theocaris model, load sets IV to VI.

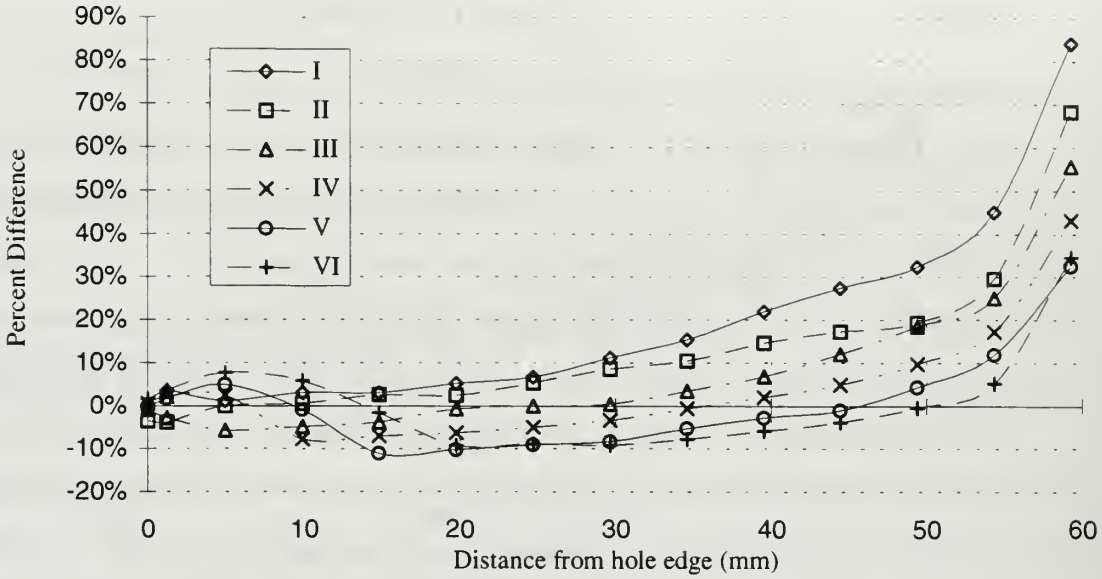

Figure 4.34. Difference of FEM and Theocaris data for σ_y.

Load Set	Applied Force	FEM Calculations		Theocaris Data	
	F_y at Far Edge (N)	F_y at minimum section (N)	Error	F_y at minimum section (N)	Error
I	19162.97	19166.13	0.02%	17254.83	-9.96%
II	21384.95	21387.70	0.01%	20004.95	-6.45%
III	25520.79	25522.31	0.01%	24975.24	-2.14%
IV	30399.66	30401.50	0.01%	30473.38	0.24%
V	34286.34	34286.69	0.00%	35225.31	2.74%
VI	38926.48	38925.78	0.00%	39660.45	1.89%

Table 4-6. Equilibrium calculations at minimum cross-section.

c. Conclusion on the Accuracy of the Finite Element Method

The finite element analysis compared favorably with the experimental data of Theocaris and Marketos. Within 20 mm of the hole edge, the error was less than 10% for all but one load set. Additionally, the results at the edge itself were within 4%. In addition to the experimental errors referred to in the beginning of this Chapter, the data

used in this study was taken from published graphs, resulting in an additional error added to the comparison. Considering these shortcomings, the FEM analysis provided quantitative results as reasonably as could be expected, and matched the qualitative trends exceptionally well.

V. NUMERICAL CALCULATION OF STRAIN ENERGY DENSITY

A. INTEGRATION ROUTINE

In order to analyze the strain energy density from the finite element data, an integration routine must be used to calculate the plastic strain energy density as shown in equation 3.25. The accuracy of any integration routine will be dependent on the number of data points integrated and the scheme implemented. This is especially true at the 'knee' of the stress-strain curve, or just past yielding where the curve bends. To increase accuracy, a third order accurate integration scheme was used by approximating the first and second derivative of each point by a central difference scheme, and using these values to perform the numerical integration. This scheme is similar to Simpson's rule, but applied for non-equally spaced points. To develop the integration routine, a function $I(x)$ is assumed in which:

$$I(x) = \int f(x)\, dx \tag{5.1}$$

Expanding $I(x)$ about the i^{th} point by Taylor series, we get:

$$\begin{aligned} I(x_i + \Delta x_i) &= I(x_i) + \Delta x_i I'(x_i) + \frac{\Delta x_i^{\,2}}{2!} I''(x_i) + \frac{\Delta x_i^{\,3}}{3!} I'''(x_i) + H.O.T. \\ I(x_i - \Delta x_{i-1}) &= I(x_i) - \Delta x_{i-1} I'(x_{i-1}) + \frac{\Delta x_{i-1}^{\,2}}{2!} I''(x_i) - \frac{\Delta x_{i-1}^{\,3}}{3!} I'''(x_i) + H.O.T. \end{aligned} \tag{5.2}$$

were the subscripts refer to each data point as shown in Figure 5.1.

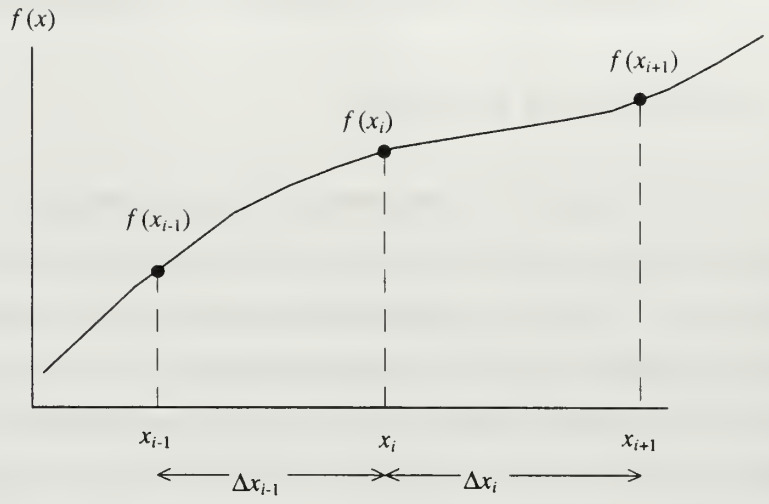

Figure 5.1 Integration points for numerical scheme.

However, from Equation 5.1, we know that:

$$I' = f(x) \qquad I''(x) = f'(x) \qquad I'''(x) = f''(x)$$

Substituting these into Equation 5.2 and solving for the integration between the i^{th} - 1 and the i^{th} + 1 point and defining this value as I_i results in:

$$I_i = \int_{x_{i-1}}^{x_{i+1}} f(x)\,dx$$

$$I_i = I(x_i + \Delta x_i) - I(x_i - \Delta x_{i-1}) + H.O.T.$$

$$I_i = (\Delta x_i + \Delta x_{i-1}) f(x_i) + \left(\frac{\Delta x_i^{\,2} - \Delta x_{i-1}^{\,2}}{2!}\right) f'(x_i) + \left(\frac{\Delta x_i^{\,3} + \Delta x_{i-1}^{\,3}}{3!}\right) f''(x_i) + H.O.T. \qquad (5.3)$$

The first and second derivatives of the function are approximated by a central difference scheme as follows:

$$f'(x_i) = \frac{\Delta x_{i-1}^{\,2}\left(f(x_{i+1}) - f(x_i)\right) + \Delta x_i^{\,2}\left(f(x_i) - f(x_{i-1})\right)}{\Delta x_{i-1}\Delta x_i\left(\Delta x_{i-1} + \Delta x_i\right)} \qquad (5.4)$$

and

$$f''(x_i) = 2\frac{\Delta x_{i-1}\left(f(x_{i+1}) - f(x_i)\right) + \Delta x_i\left(f(x_{i-1}) - f(x_i)\right)}{\Delta x_{i-1}\Delta x_i\left(\Delta x_{i-1} + \Delta x_i\right)} \qquad (5.5)$$

Equations 5.4 and 5.5 are substituted into Equation 5.3, then summed over every other data point to obtain the final integration value:

$$\int_{x_1}^{x_N} f(x) = \sum_{\substack{i=2 \\ \text{even } i}}^{i=N-1} I_i \qquad (5.6)$$

B. RESULTS OF NUMERICAL SCHEME ON UNIAXIAL CASE

A comparisons of the above numerical integration routine to a standard trapezoidal integration routine were made, using the uniaxial strain energy density equation with the Ramberg-Osgood stress-strain relationship. The stress-strain curve integrated is shown below in Figure 5.2, with the limits for both stress and strain labeled. The material constants were $n = 0.053$, $K = 95$ksi, and $E = 10 \times 10^3$ ksi. For the modified Simpson's rule integration routine, two forms of the strain energy integral were used, Equation 2.6 and 2.14. The actual value is given by Equation 2.17. Note that for integration by the trapezoid rule, both of these forms of the strain energy density produce identical values; however, for the applied integration routine, an upper and lower bound is calculated. This is shown in Figure 5.3, which applied the routine to equally spaced points. Note that the actual implementation of this routine will produce improved results due to a more efficient distribution of the data points; i.e., few points along the linear portion and a closer distribution in the region of higher curvature. Since the modified Simpson's integration routine produced better results than the trapezoidal rule for higher data points, this was chosen as the means of integration to calculate the strain energy density. Additionally, the basic form of the strain energy density integral as given in Equation 2.5 was able to be incorporated within the I-DEAS Master Series™ post-processing module; hence, this was the final form used to calculate the strain energy density.

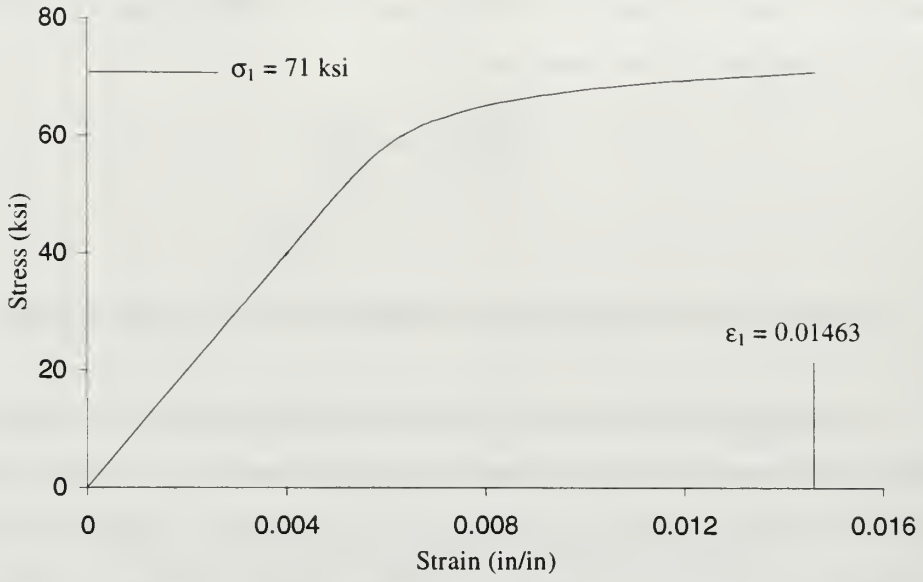

Figure 5.2. Stress-Strain Curve for Integration Comparison.

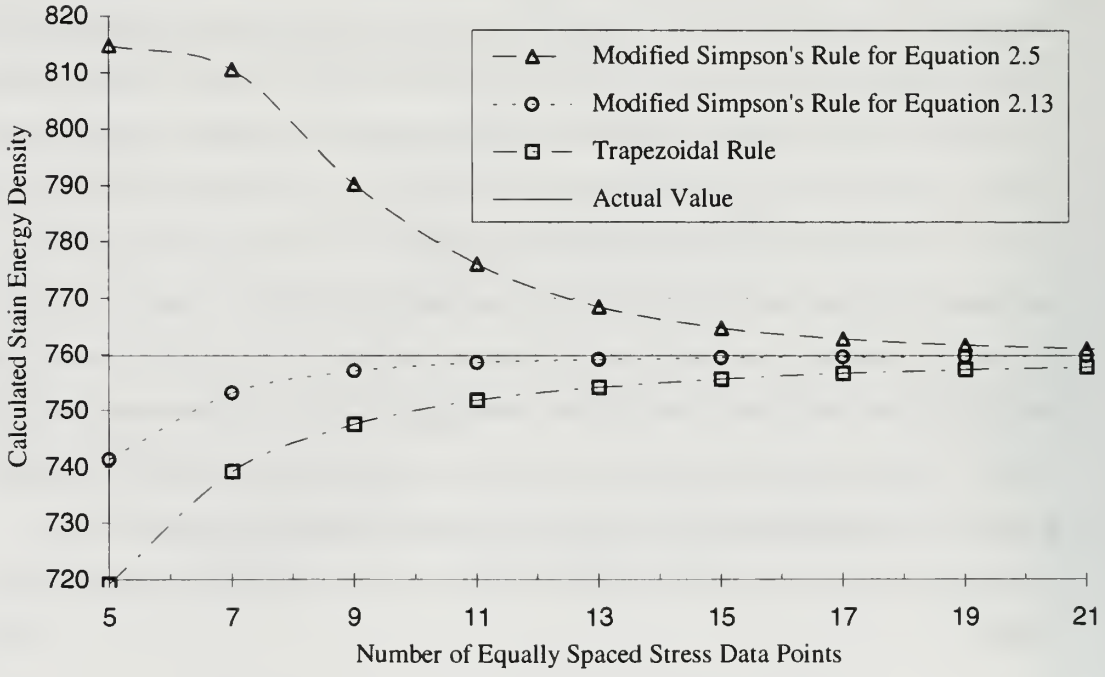

Figure 5.3. Comparison of Integration Routines.

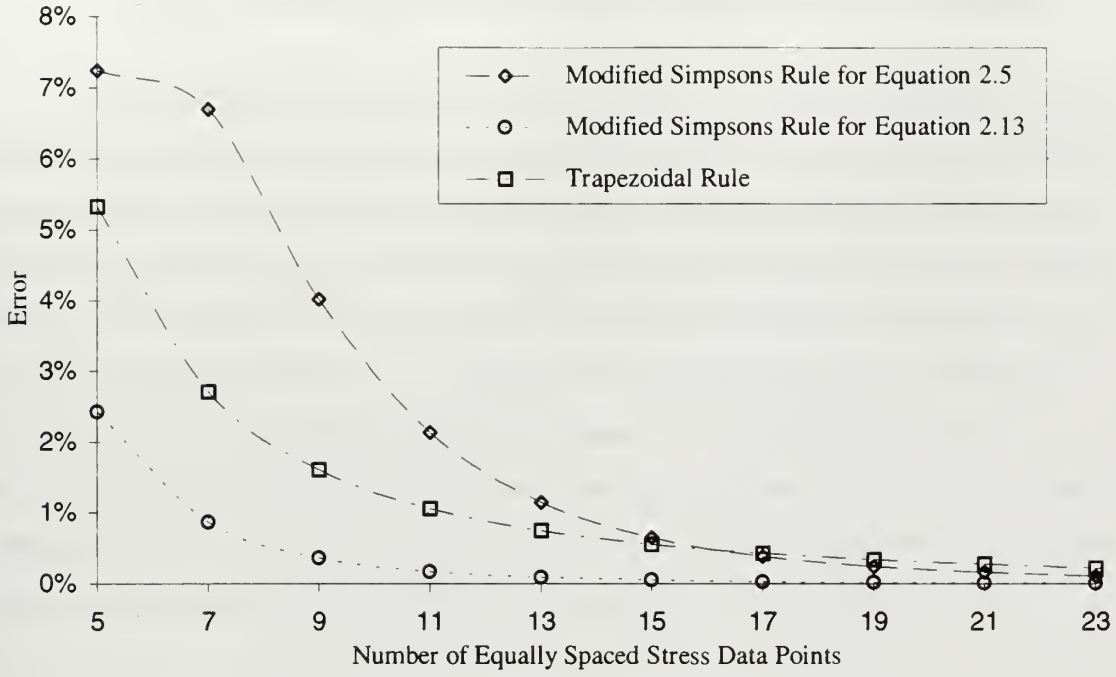

Figure 5.4. Percent Error of Integration Routines.

VI. CALCULATIONS AND RESULTS OF STRAIN ENERGY DENSITY

In order to test the validity of the Glinka strain energy density proposal, the strain energy density for a given loading was calculated based on an elasto-plastic material (W_p) and an elastic material (W_e), and comparisons between the two calculations were made. The strain energy density calculations were performed at each node throughout the FEM model, with the plastic strain energy density (W_p) being numerically integrated at each load step as shown in Chapter V. In addition to the strain energy density calculations, comparisons were made between the notch stresses and strains based on the finite element method and values obtained via both the Glinka and the Neuber method. These comparisons will be made in Chapter VII. The finite element analysis was performed on a plate with symmetrical, semi-circular edge notches.

A. NOTCH GEOMETRY AND MATERIAL SELECTION

Two separate geometries were evaluated, one had a notch radius of 1.0 inch, and a plate width of 6.0 inches (r/D = 1/6), and the second had a notch radius of 1.0 inch and a plate width of 10.0 inches (r/D = 1/10). These two layouts are shown below in Figure 6.1, with the shaded regions representing the finite element geometry. For each geometry, plane stress (thin plate) and plane strain (thick plate) analyses were performed. The strain-hardening material used modeled 7075-T6 Aluminum. This was represented in the I-DEAS Master Series™ finite element program as 20 data points, shown in Figure 6.2. This figure also shows the yield stress, determined to be 66 ksi based on a plastic strain offset of 0.002. However, it should be noted that the stress-strain curve departs from linearity at 40 ksi. The 20 data points were obtained by curve fitting the Ramberg-Osgood equation to actual stress-strain data from the Military Handbook V [Ref. 110]; then calculating these points from the resulting Ramberg-Osgood equation. Although this may have resulted in the stress-strain curve used by the FEM analysis differing from the actual 7075-T6 data, it ensured that the notch root strains and plastic strain energy density could be calculated from the finite element stresses using the Ramberg-Osgood equation. This enabled correlating predicted strains based on the Ramberg-Osgood equation and

either the Neuber or Glinka method to the finite element results. The material property coefficients, including values resulting from the data fit to the Ramberg-Osgood equation, are listed in Table 6-1.

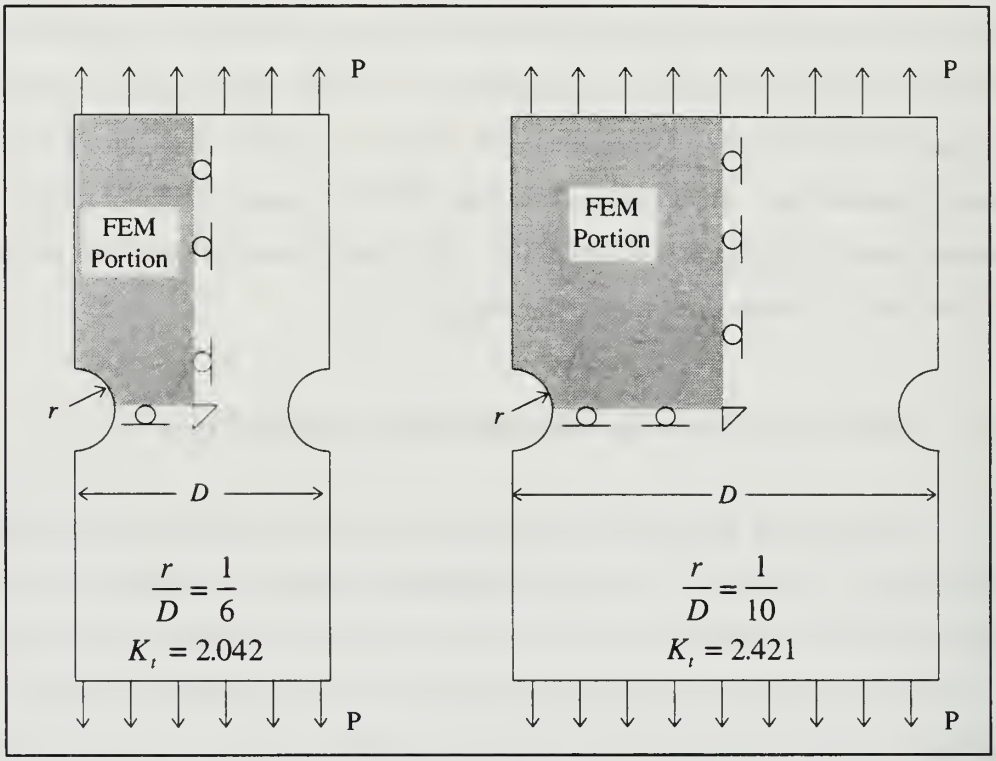

Figure 6.1. Notch Geometry and Finite Element Boundary Conditions.

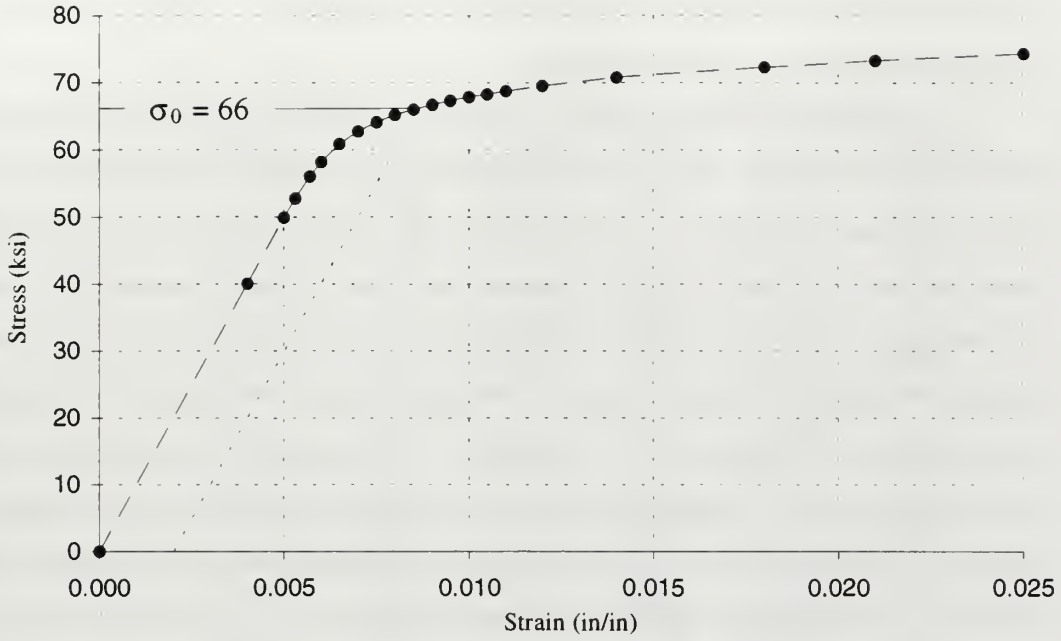

Figure 6.2 Stress-Strain Curve for 7075-T6 Aluminum.

Coefficient	Value
E (ksi)	10,000.0
K (ksi)	92.0
σ_0 (ksi)	66.18
n	0.053

Table 6-1. 7075-T6 Material Constants.

B. FINITE ELEMENT MODELING

Due to the two lines of symmetry for this geometry, the finite element model was reduced to one quarter of the physical model by applying appropriate constraints along each boundary, as shown in Figure 6.1. For each configuration, 21 increments were used to increase the loading from an initial nominal stress of 12 ksi to a final value of 49.5 ksi, or 75 percent of the yield stress. This load increment ensured convergence of the finite element solution and provided a small enough step to numerically integrate the strain energy density with reasonable accuracy. The first two load points were in the elastic range, and plastic deformation began at the third load step. The stress concentration factor K_t was determined from the finite element analysis at the first load step, and found to be

2.042 and 2.421 for the narrow and the wide plate, respectively. Table 6-2 shows the load schedule for each of the geometries.

As in the previous finite element analyses, a mesh comparison was performed for each of the geometries. The number of elements and nodes for each geometry used in the comparison are shown below in Table 6-3. For the wide plate (r:D = 1:10), the medium mesh was obtained directly from the coarse mesh by an I-DEAS Master Series™ routine of splitting elements in the region of highest elastic strain energy density. The mesh layouts are shown in Figures 6.3 and 6.4. Comparisons of both stresses and strains were made for each of the mesh sizes at load step 21. The comparison showed that the mesh refinement resulted in little change in the stresses and strains throughout the model. Figures 6.5 and 6.6 show the stress and strain distributions along the minimum cross section for the each plate. For the narrow plate at the notch root itself, the stress decreased by 0.16% going from the coarse to medium mesh, and decreased by 0.03% going from the medium to fine mesh. For the strains, the medium mesh resulted in a 0.24% decrease in strain compared to the coarse mesh, and there was no change compared to the fine mesh. Similar results are shown for the mesh refinement for the wide plate. The mesh adaptation used on the coarse mesh to obtain the medium mesh resulted in a decrease of the notch root stress by only 0.22%. The strain at the notch root decreased 0.58% from the medium mesh to the coarse mesh. These results showed that the medium mesh for both geometries was sufficient to provide mesh independent solutions. Hence, for all further finite element analysis, the medium meshes were used.

Load Step	Notch $r:D$ = 1:6			Notch $r:D$ = 1:10		
	P (ksi)	S (ksi)	K_tS (ksi)	P (ksi)	S (ksi)	K_tS (ksi)
1	8.00	12.00	24.50	9.60	12.00	29.05
2	13.00	19.50	39.81	15.60	19.50	47.21
3	15.00	22.50	45.94	18.00	22.50	54.47
4	16.00	24.00	49.00	19.20	24.00	58.10
5	17.00	25.50	52.06	20.40	25.50	61.73
6	18.00	27.00	55.13	21.60	27.00	65.36
7	19.00	28.50	58.19	22.80	28.50	68.99
8	20.00	30.00	61.25	24.00	30.00	72.63
9	21.00	31.50	64.31	25.20	31.50	76.26
10	22.00	33.00	67.38	26.40	33.00	79.89
11	23.00	34.50	70.44	27.60	34.50	83.52
12	24.00	36.00	73.50	28.80	36.00	87.15
13	25.00	37.50	76.56	30.00	37.50	90.78
14	26.00	39.00	79.63	31.20	39.00	94.41
15	27.00	40.50	82.69	32.40	40.50	98.04
16	28.00	42.00	85.75	33.60	42.00	101.68
17	29.00	43.50	88.81	34.80	43.50	105.31
18	30.00	45.00	91.88	36.00	45.00	108.94
19	31.00	46.50	94.94	37.20	46.50	112.57
20	32.00	48.00	98.00	38.40	48.00	116.20
21	33.00	49.50	101.06	39.60	49.50	119.83

Table 6-2. Load Increment Schedule.

Geometry	Mesh	Element	Nodes
Narrow Plate	Coarse Mesh	298	965
($r:D$ = 1:6)	Medium Mesh	1,128	3,507
	Fine Mesh	2,291	7,046
Wide Plate	Coarse Mesh	456	1,453
($r:D$ = 1:10)	Medium Mesh	1,064	3,233

Table 6-3. Number of Elements and Nodes for Mesh Comparison.

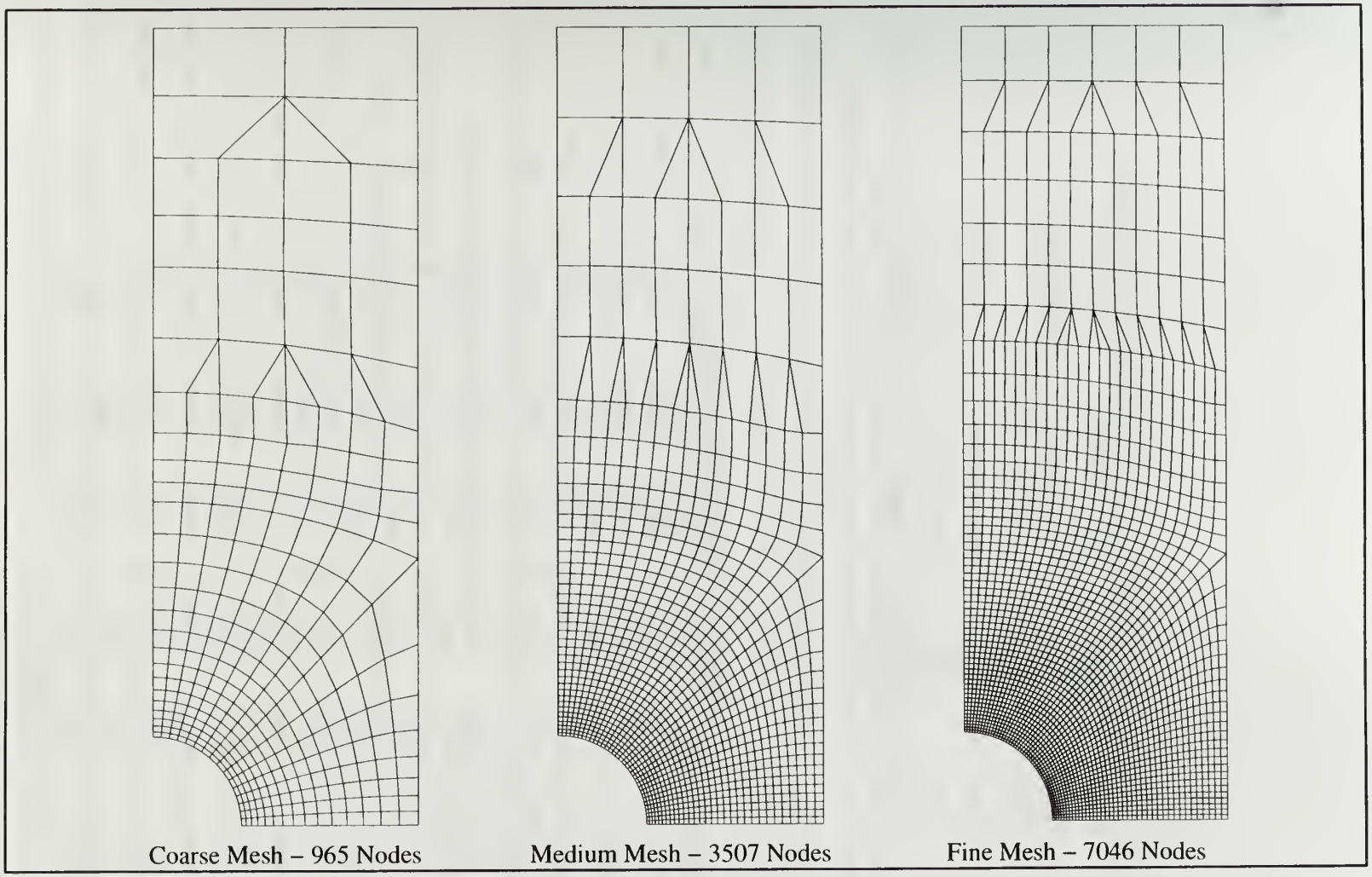

Figure 6.3. Mesh Lalyouts for Narrow Notched Plate.

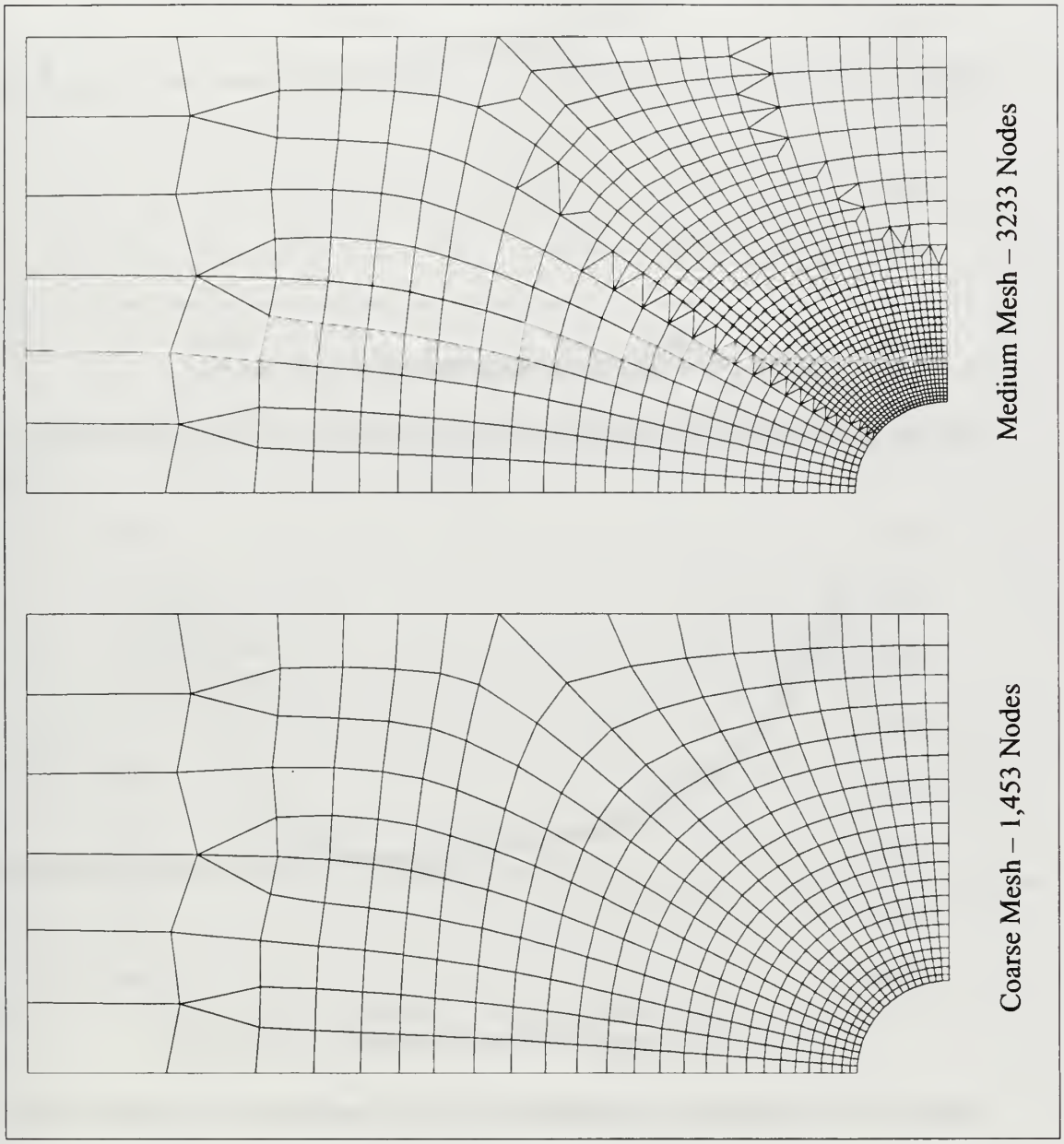

Figure 6.4. Mesh Layouts for Wide Plate.

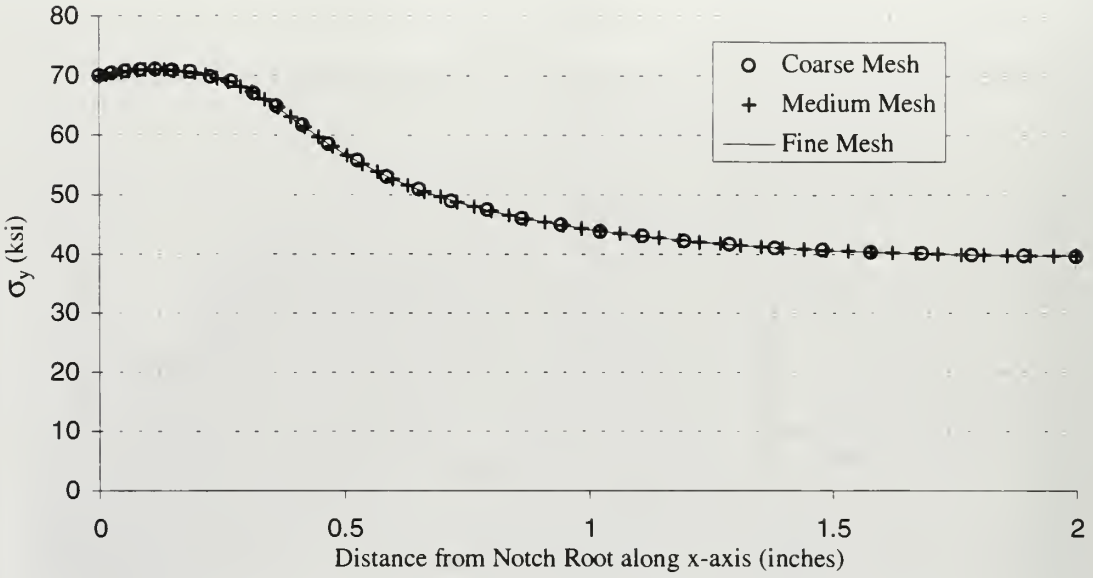

Figure 6.5. Distribution of σ_y for Mesh Comparison of Narrow Plate FEM Model.

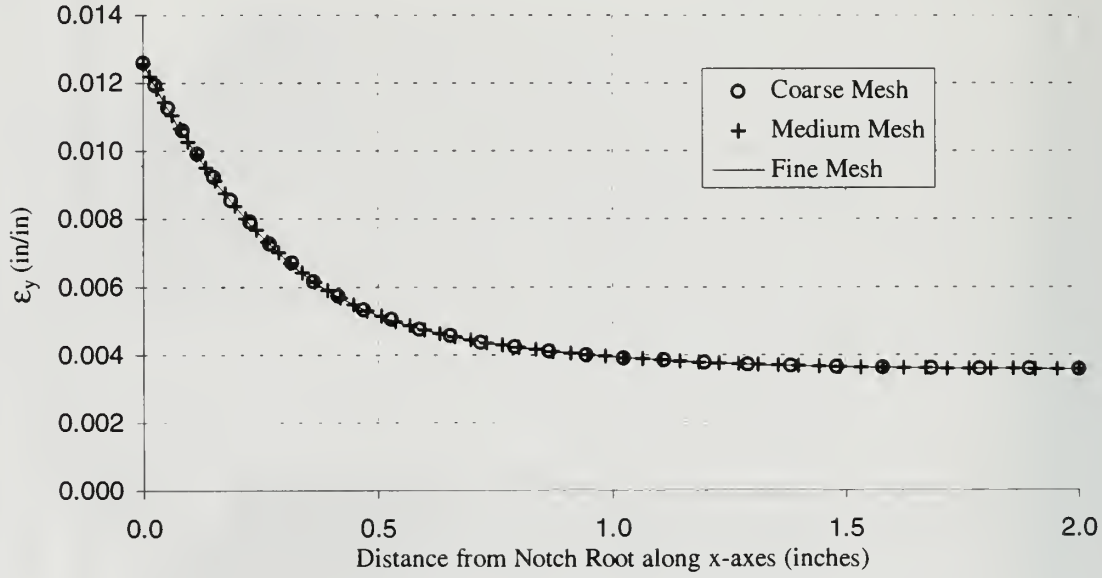

Figure 6.6. Distribution of ε_y for Mesh Comparison of Narrow Plate FEM Model.

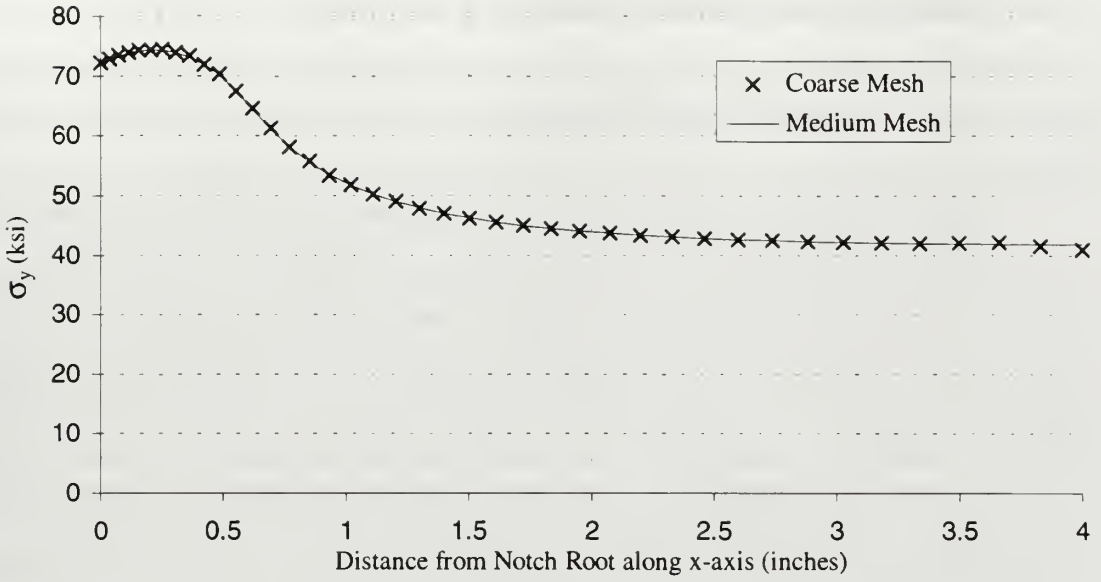

Figure 6.7. Distribution of σ_y for Mesh Comparison of Wide Plate FEM Model.

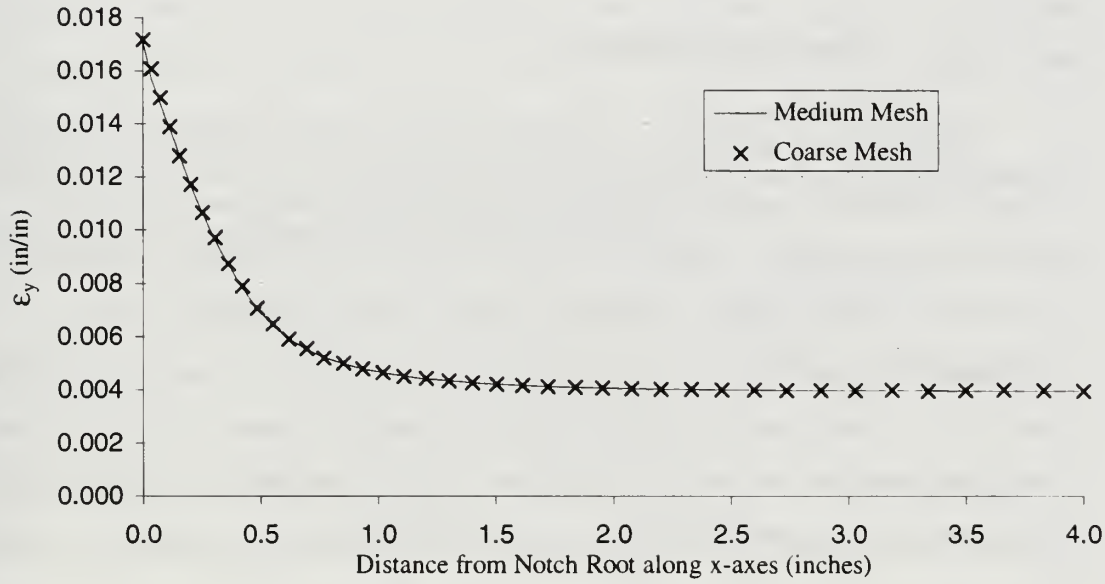

Figure 6.8. Distribution of ε_y for Mesh Comparison of Wide Plate FEM Model.

C. RESULTS OF FINITE ELEMENT ANALYSIS

1. Computational Procedures

The elastic strain energy density (W_e) at each node was initially calculated at the first load step. To determine W_e at later load steps, this value was simply multiplied by a factor of $(P_i/P_0)^2$, where P_i is the load at the i^{th} step, and P_0 is the initial load. Plastic strain energy density (W_p) was calculated incrementally with the integration procedure shown in Chapter V. To calculate a strain energy density increment ΔW_p, two new data points were required, in addition to last point of the previous increment. Since the first load step was under elastic conditions, W_p is equal to W_e; hence, the first load step resulted in the first plastic strain energy density calculation without requiring any integration. Subsequent calculations were performed at all odd load steps.

2. Plane Stress Condition

For both plate widths, the plastic strain energy density was found to be greater than the elastic strain energy density in the vicinity of the notch root. Figures 6.9 and 6.10 are plots of W_p at load step 21 for the narrow and wide plates, respectively, under plane stress conditions. These show that the plastic strain energy density throughout the model has its maximum value at the notch root, but rapidly approaches the far-field value away from the notch. Figures 6.11 and 6.12 show W_p for several load steps along the minimum cross section of the plates, with W_e included at the final load step. This shows that not only does W_e give under estimated values at the notch root, but also

$$W_{ERROR} = \frac{W_p - W_e}{W_p} \qquad (6.1)$$

follows a different distribution shape than W_p. At the notch root itself for the final load step ($S = 0.75\sigma_0$), the difference between W_p and W_e reaches a value of 16.8% and 23.2% for the narrow plate and wide plate respectively. Figures 6.13 and 6.14 show contour plots of the difference in W_p as compared to W_e, as shown in Equation 6.1, so that positive

values indicate that the actual W_p is higher than that estimated by the Glinka Method. These values are taken at the final load step (S = 0.75 σ_0). In the plastic region, the greatest difference between the two calculations occurs not at the notch root itself, as may be expected, but slightly offset along the x-axis. This maximum error is also on the order of twice the value of that at the notch root. The location of the maximum difference between W_p and W_e corresponds fairly well with the location of the maximum σ_y value. It should be noted that although the contour plots show the maximum global error occurring slightly above the notch near the plate edge, this is also a region of very low to zero strain energy density, and therefore these errors are actually insignificant. Figures 6.15 and 6.16 show the error in strain energy density for each load step across the x-axis (at y = 0). These plots show that, as previously stated, the maximum error occurs at the notch root for small plastic yielding, then gradually progresses inward along the x-axis. Global errors for the previous load steps followed the save trends as that of the final load step. Starting with zero error at the initiation of plastic deformation, the regions of significant error (greater than 1%) start at the notch root, and move inward, while at the same time proceeding at an angle toward the vertical centerline of the plate. This trend also corresponds to the region of high σ_e and the growth of the plastic zone (this growth is well documented by Theocaris and Marketos [Ref. 18]).

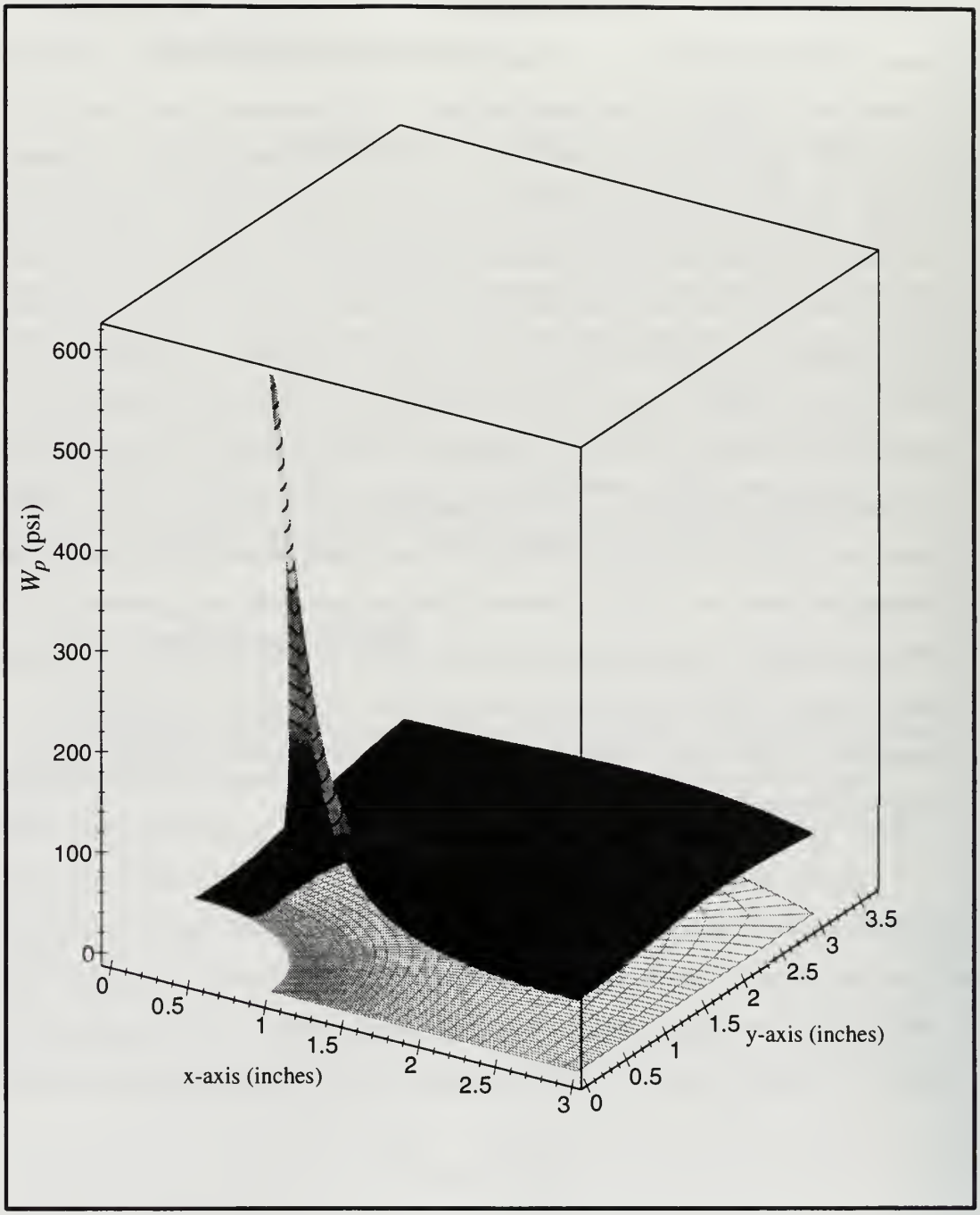

Figure 6.9. Plastic Strain Energy Density W_p for Narrow Plate in Plane Stress at Load Set 21.

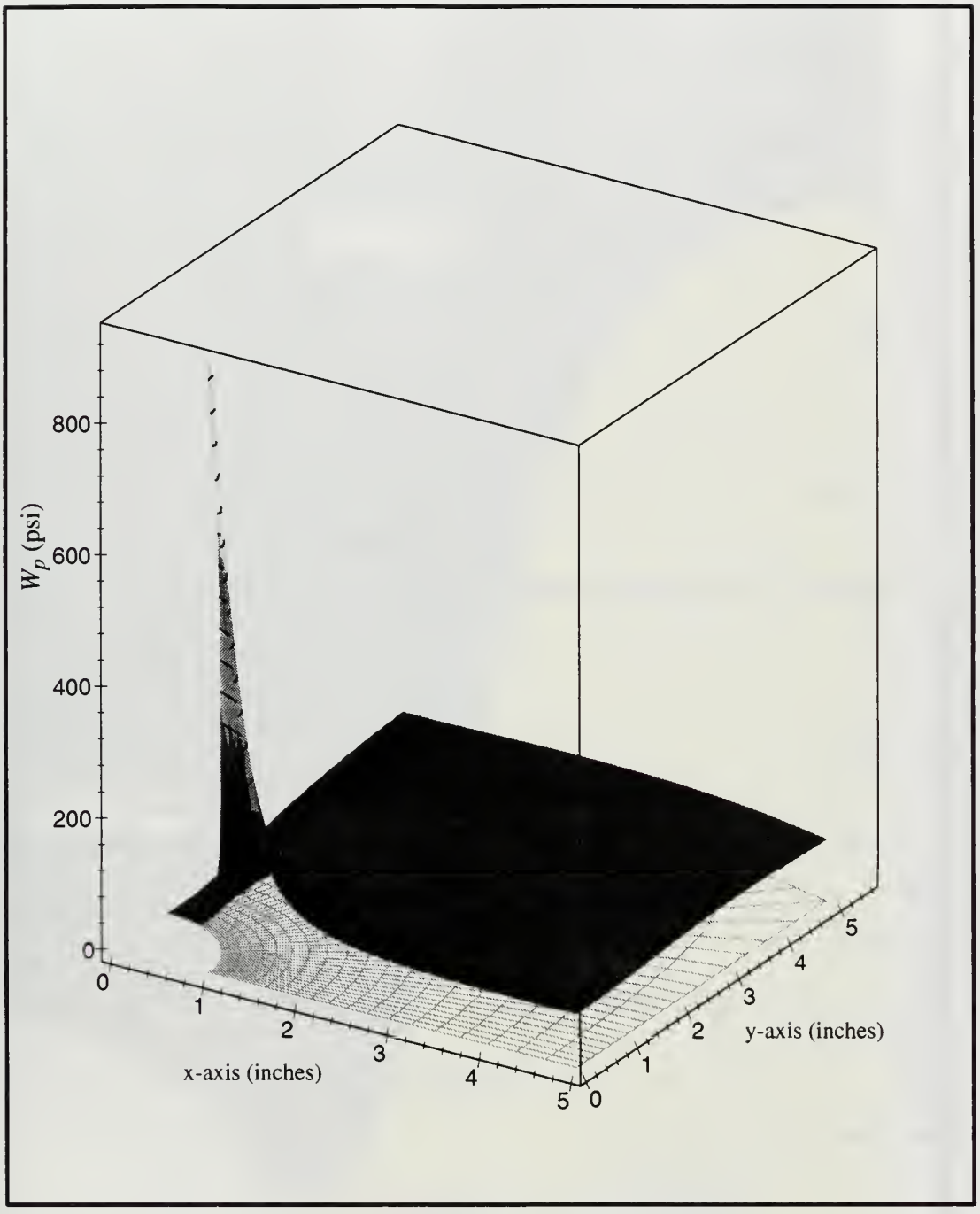

Figure 6.10. Plastic Strain Energy Density W_p for Wide Plate in Plane Stress at Load Set 21.

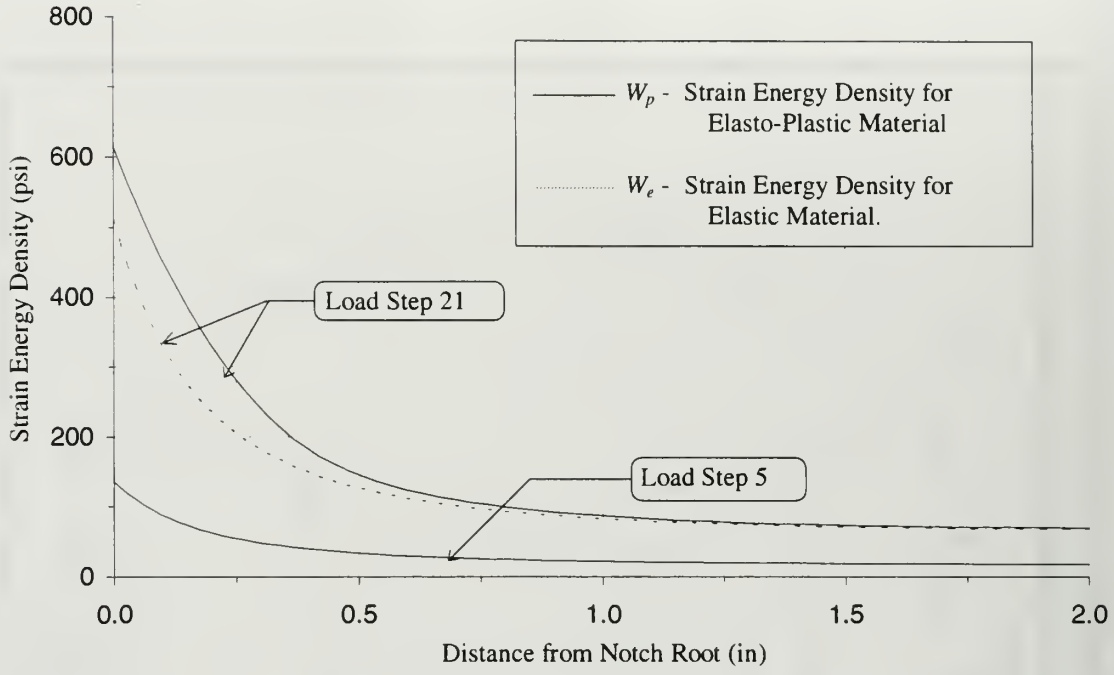

Figure 6.11. Strain Energy Density along x-axis for Narrow Plate in Plane Stress.

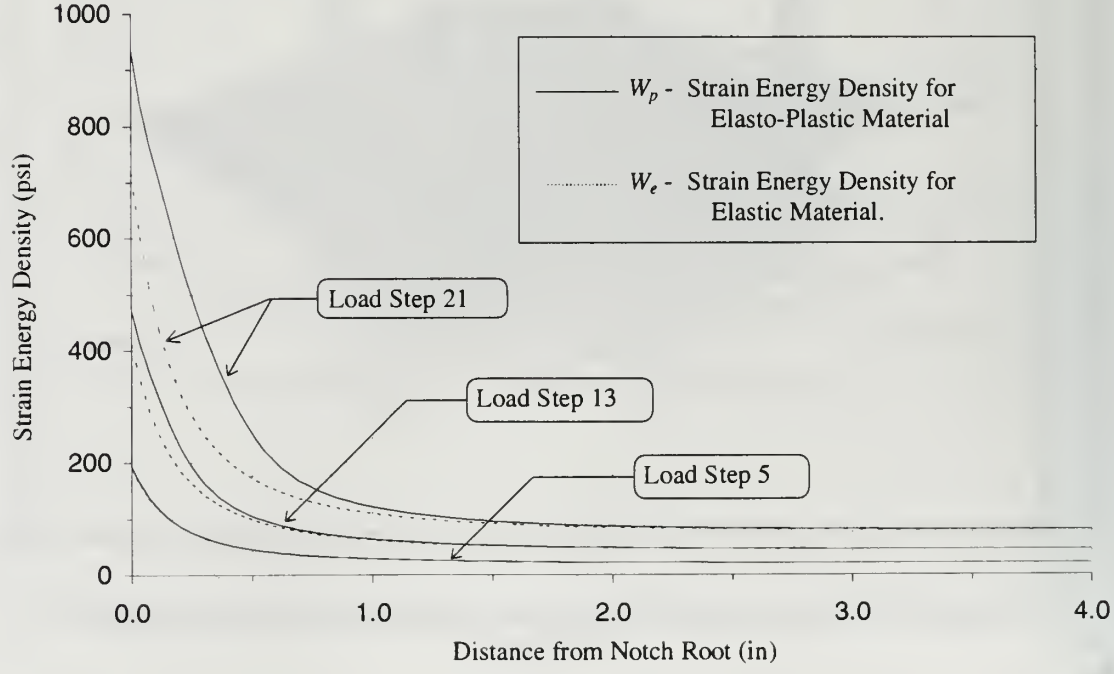

Figure 6.12. Strain Energy Density along x-axis for Wide Plate in Plane Stress.

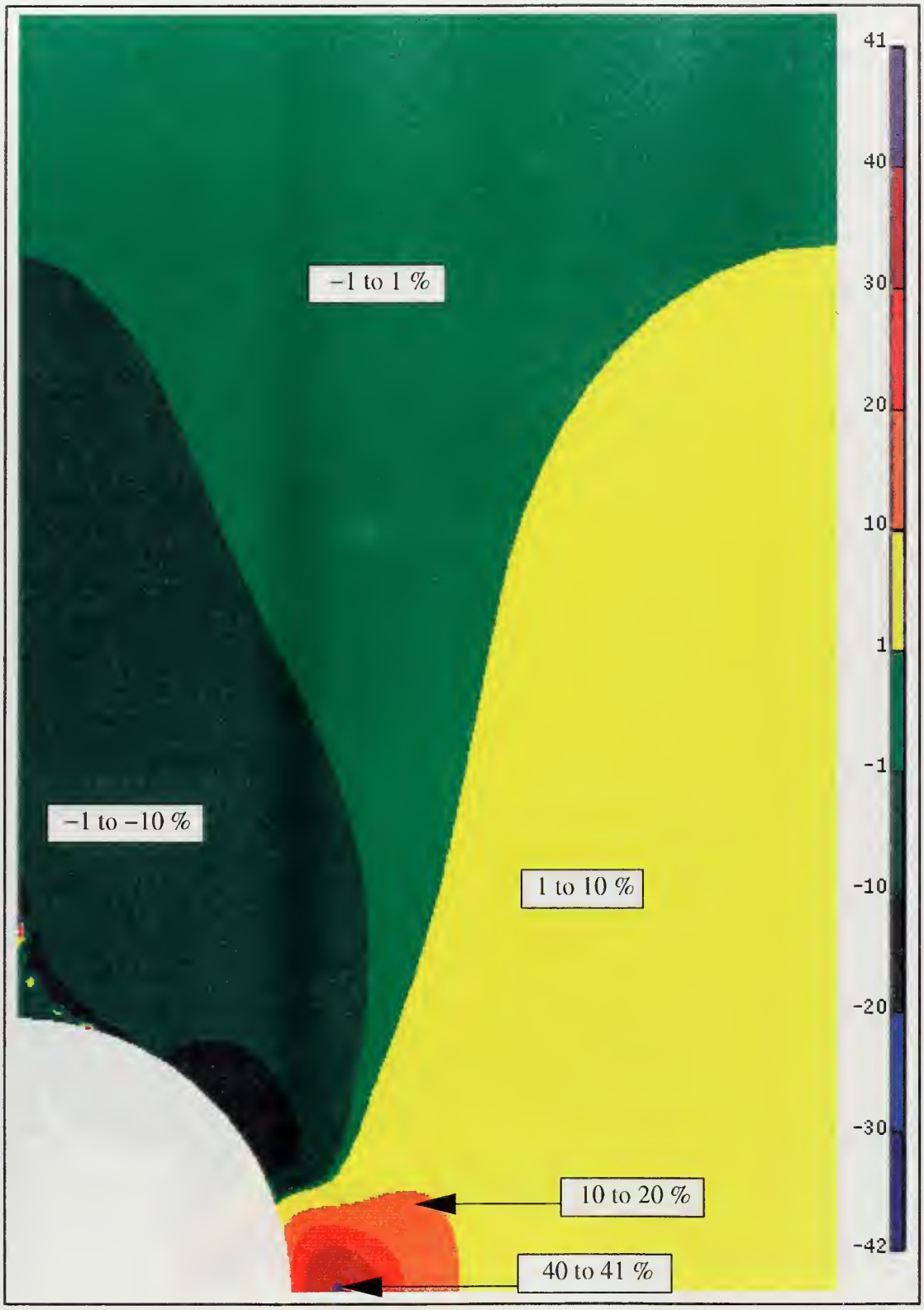

Figure 6.13. Difference Between W_p and W_e for Narrow Plate in Plane Stress at Load Step 21.

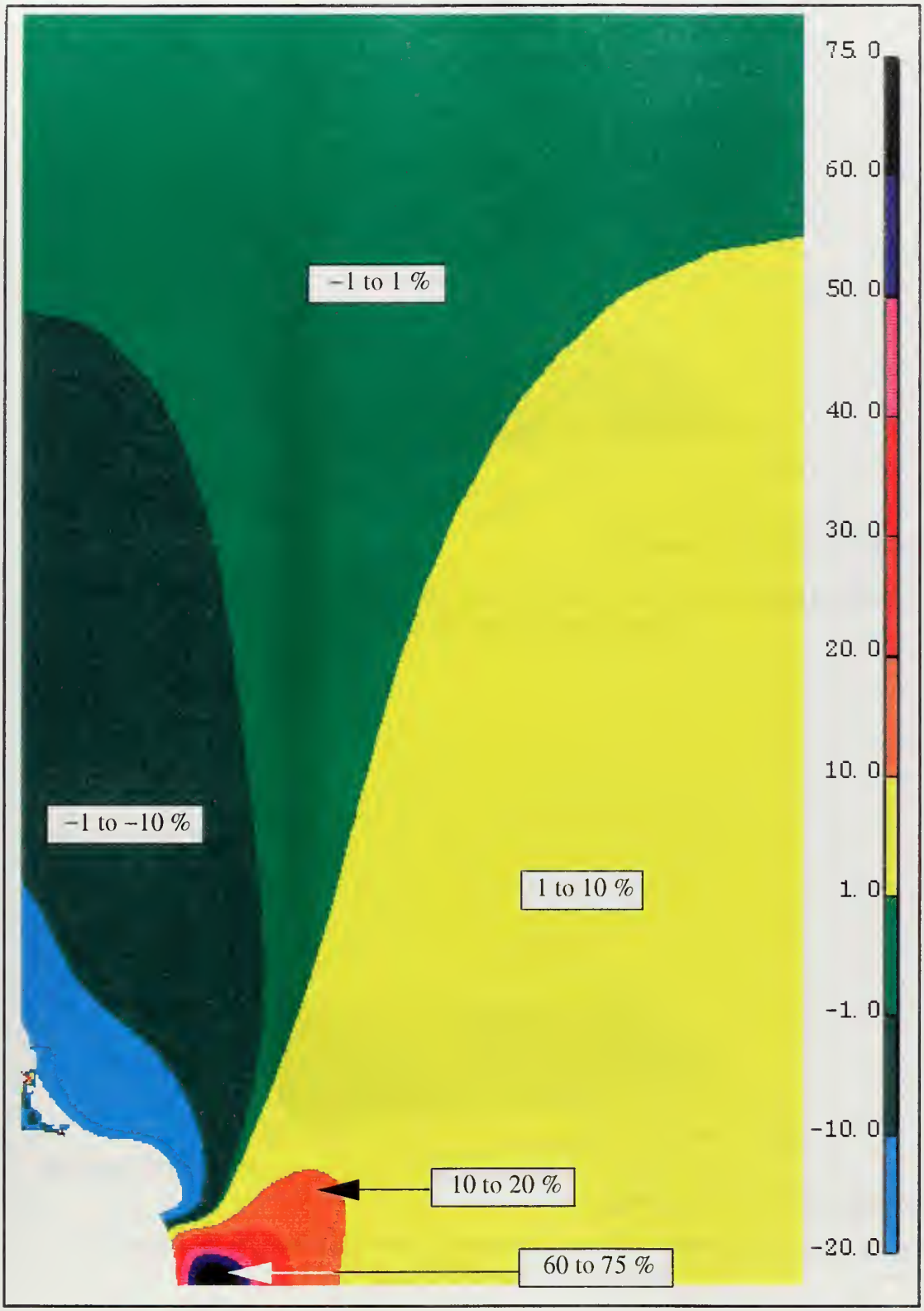

Figure 6.14. Difference Between W_p and W_e for Wide Plate in Plane Stress at Load Step 21.

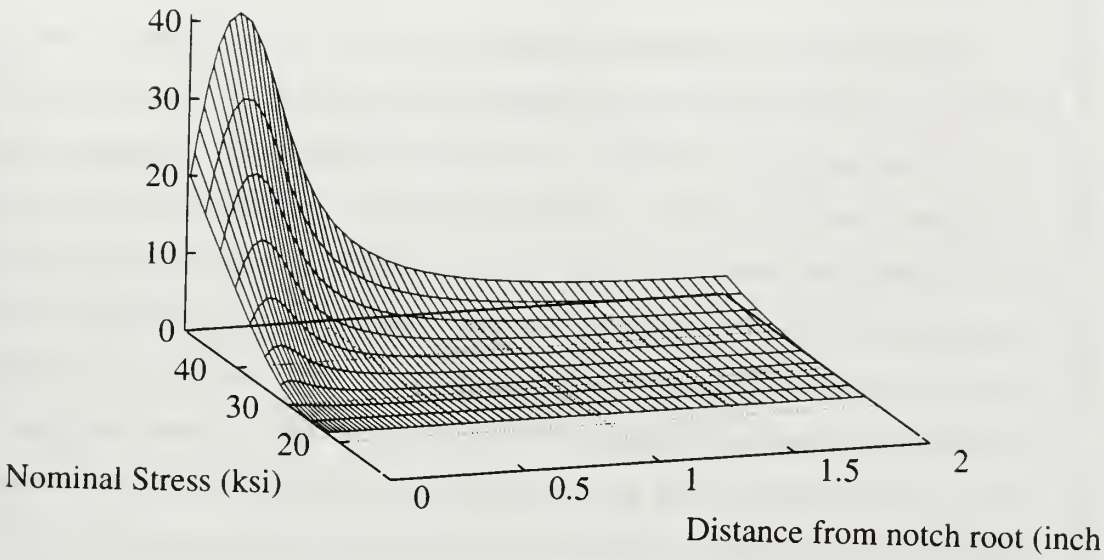

Figure 6.15. Percent Difference Between W_p and W_e for Narrow Plate in Plane Stress Along Minimum Cross Section.

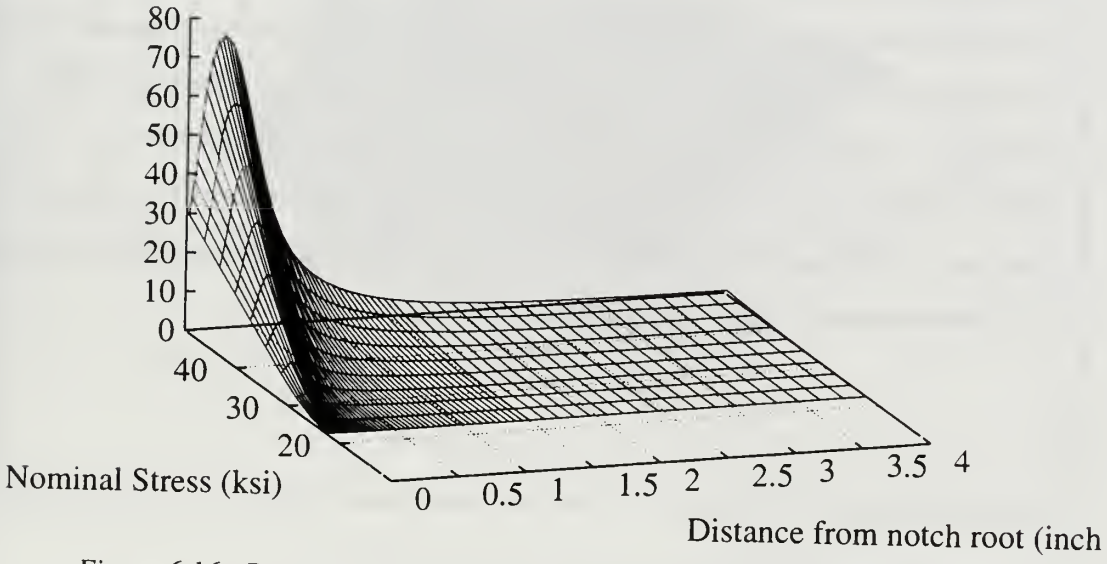

Figure 6.16. Percent Difference Between W_p and W_e for Wide Plate in Plane Stress Along Minimum Cross Section.

3. Plane Strain Condition

The results of the strain energy density calculations showed better agreement between W_p and W_e than for the plane stress condition. Figures 6.17 and 6.18 are plots of W_p at the final load step. As in the plane stress case, there appears a high peak value at the notch root, with a rapid drop-off to the far-field value. Figures 6.19 and 6.20 show W_p for several load steps along the minimum cross section of the plates, with W_e included at the final load step. Closer agreement between the two strain energy densities is shown than for the plane stress condition. The plane strain problem results in a configuration that is physically more constrained than that of the plane stress problem, and hence the amount of plastic growth at the notch under plane strain conditions will be less than that of the plane stress condition. Therefore, the basis that the strain energy density distribution in the plastic region remains relatively unchanged due to a high volume of elastic material surrounding the plastic region should be even more valid for the plane strain condition than that of the plane stress condition. This was in fact shown to be the case when comparing the finite element plastic strain energy density W_p with that of W_e, as can be seen in Figures 6.21 and 6.22, which are contours of the difference between the two energies. As in the case of the plane stress condition, W_p for the plane strain condition is shown to be greater than that of W_e. However, both the amount of error and region of significant error (greater than 1%), is much improved over the plane stress condition. At the notch root itself, the difference between the two calculations was only 7.76% for the narrow plate and 10.6% for the wide plate.

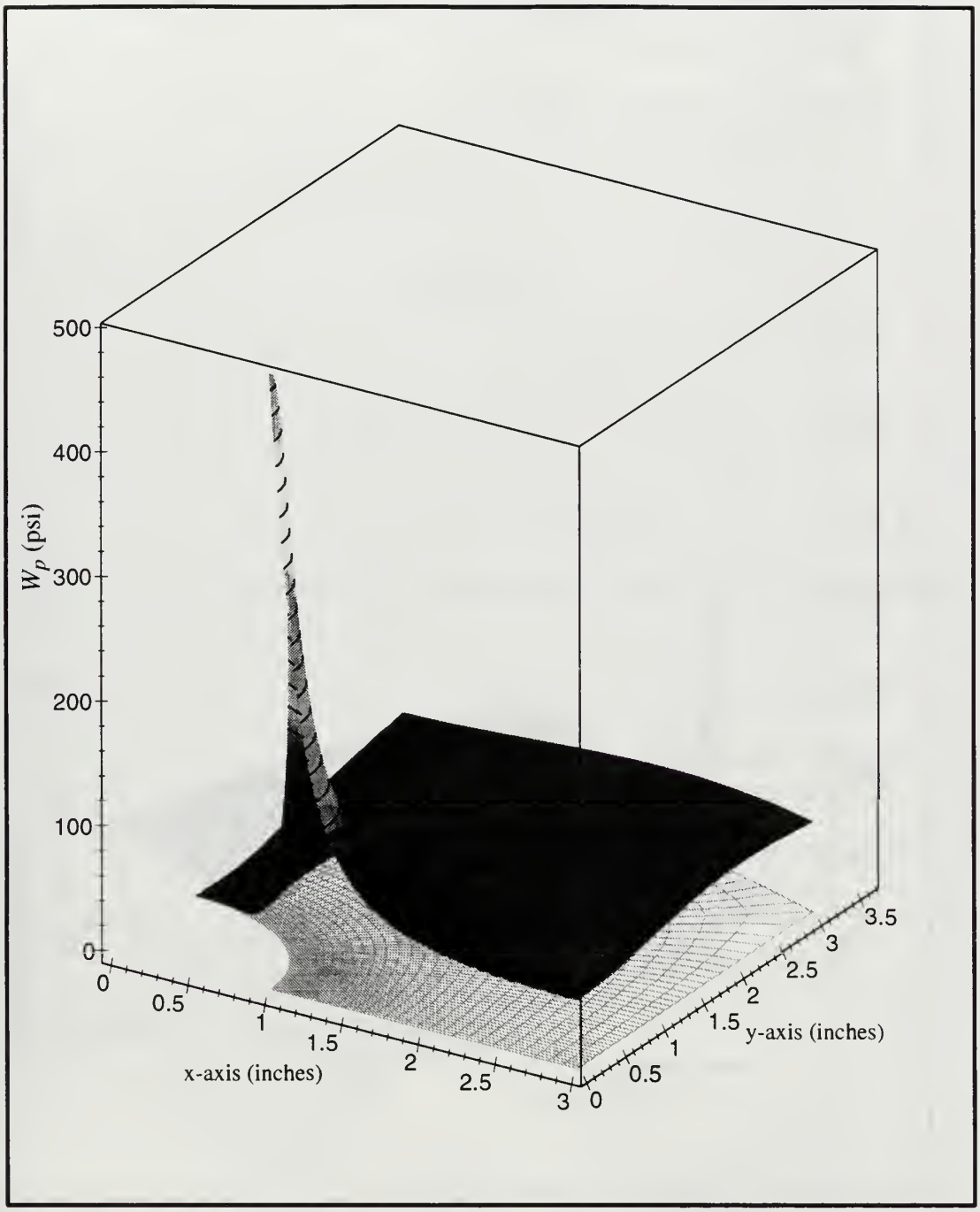

Figure 6.17. Plastic Strain Energy Density W_p for Narrow Plate in Plane Strain at Load Set 21.

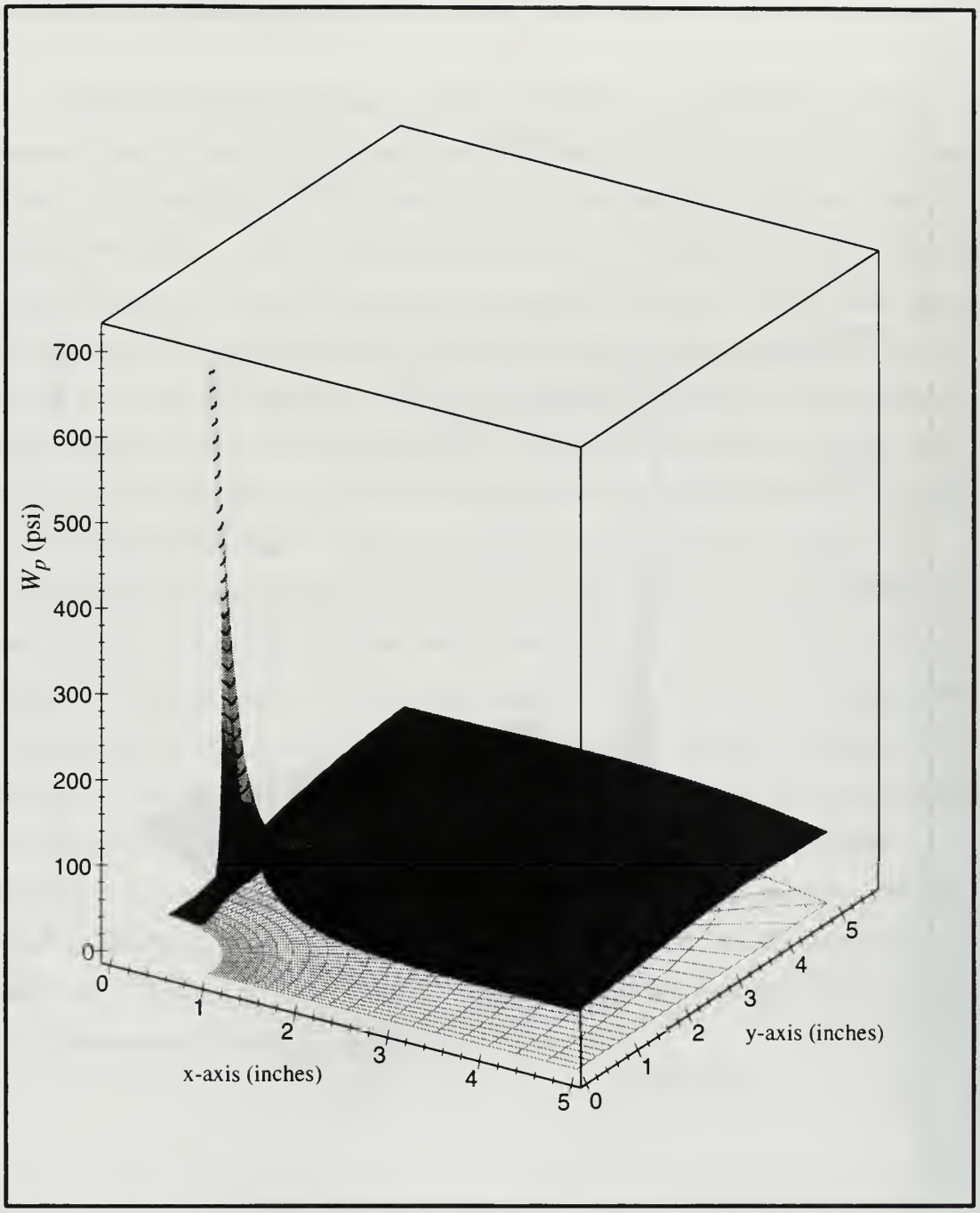

Figure 6.18. Plastic Strain Energy Density W_p for Wide Plate in Plane Strain at Load Set 21.

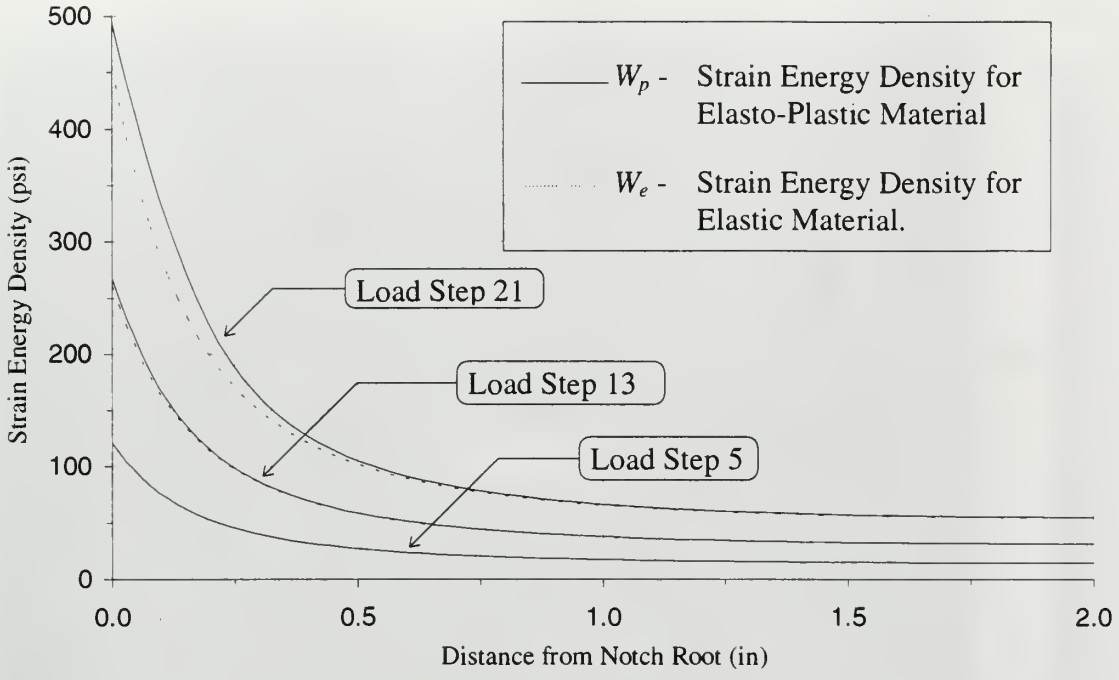

Figure 6.19. Strain Energy Density along x-axis for Narrow Plate in Plane Strain.

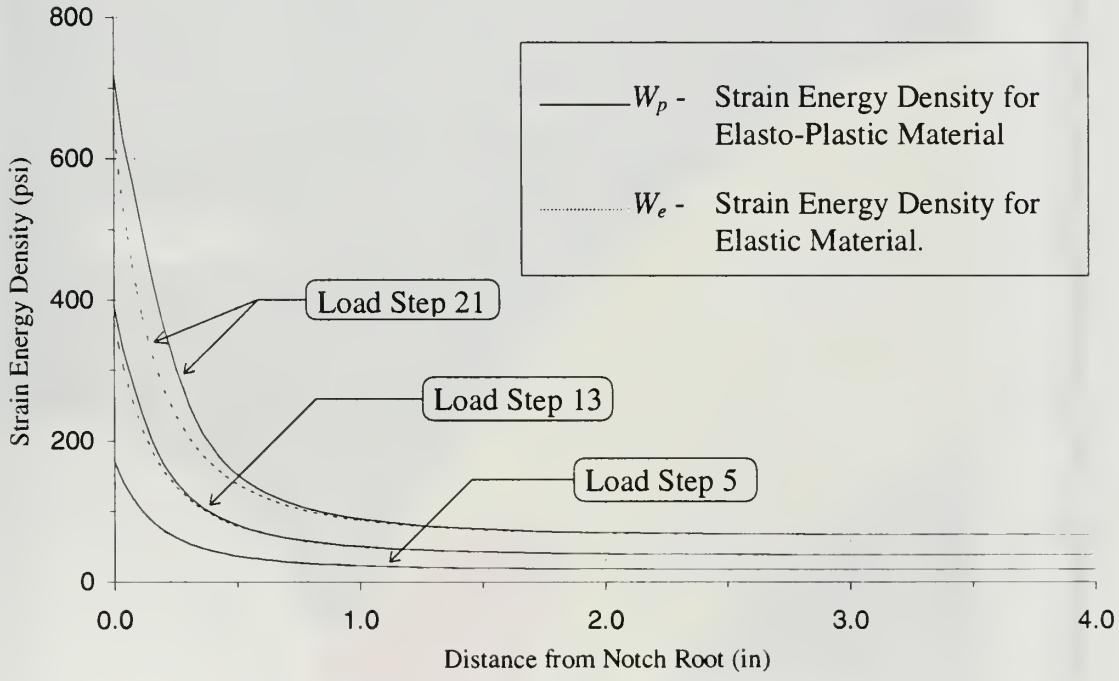

Figure 6.20. Strain Energy Density along x-axis for Wide Plate in Plane Stress.

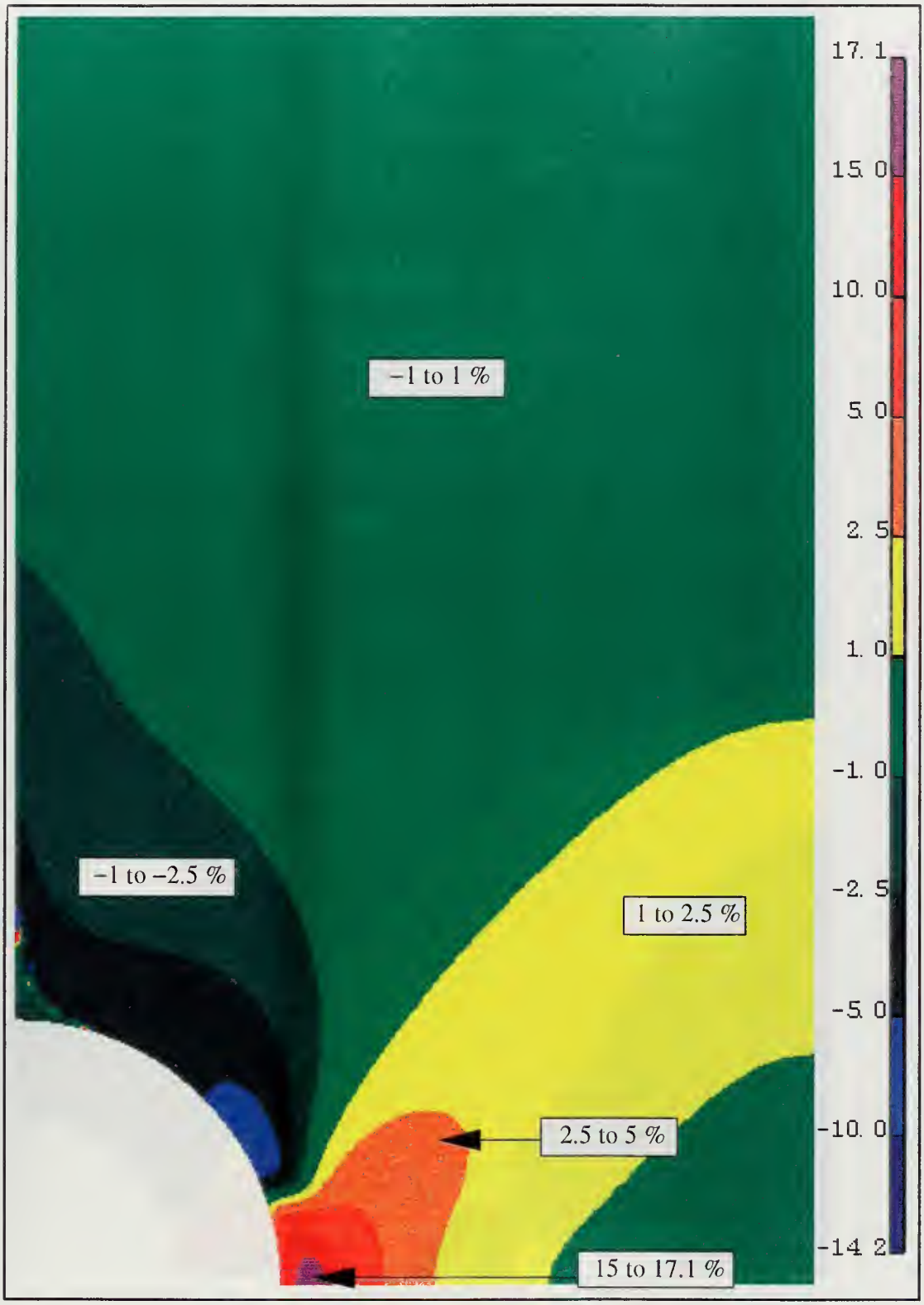

Figure 6.21. Difference Between W_p and W_e for Narrow Plate in Plane Strain at Load Step 21.

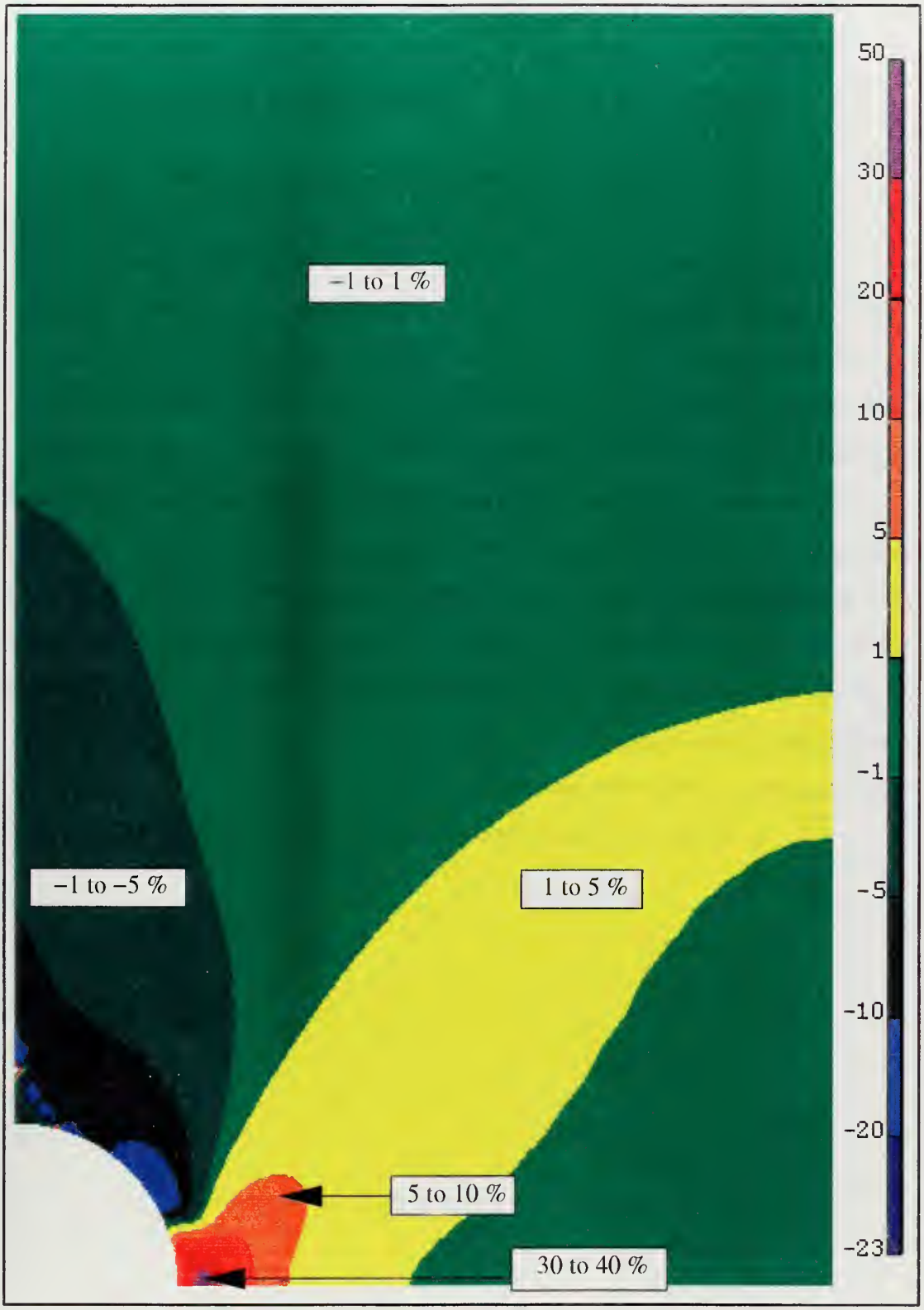

Figure 6.22. Difference Between W_p and W_e for Wide Plate in Plane Strain at Load Step 21.

VII. STRESS AND STRAIN CALCULATIONS

A. PLANE STRESS CONDITION

1. Finite Element Method Results

The stress distributions for plane stress for both geometries are shown in Figures 7.1 through 7.4. These plots depict either σ_y or σ_x along the minimum cross section (y = 0) as a function of the nominal loading. As stated in Chapter IV, the maximum σ_y value progresses inward from the notch root as yielding increases. This can be attributed to the σ_x component, which starts from zero at the notch root and rapidly approaches its maximum value inward from the notch root. This increase in the σ_x component results in a higher allowable σ_y than at the notch root before yielding occurs. If one considers the limiting case of a perfectly plastic material; then at the notch root, σ_y, would remain at the value of the yield stress after initial yielding. However, at some point inward from the notch root, σ_y would be higher than the yield stress due to the σ_x component. The other limiting case is an elastic only material, where σ_y would linearly increase with loading. As can be seen from the stress distributions, the results of the work-hardening material falls somewhere between these two extremes.

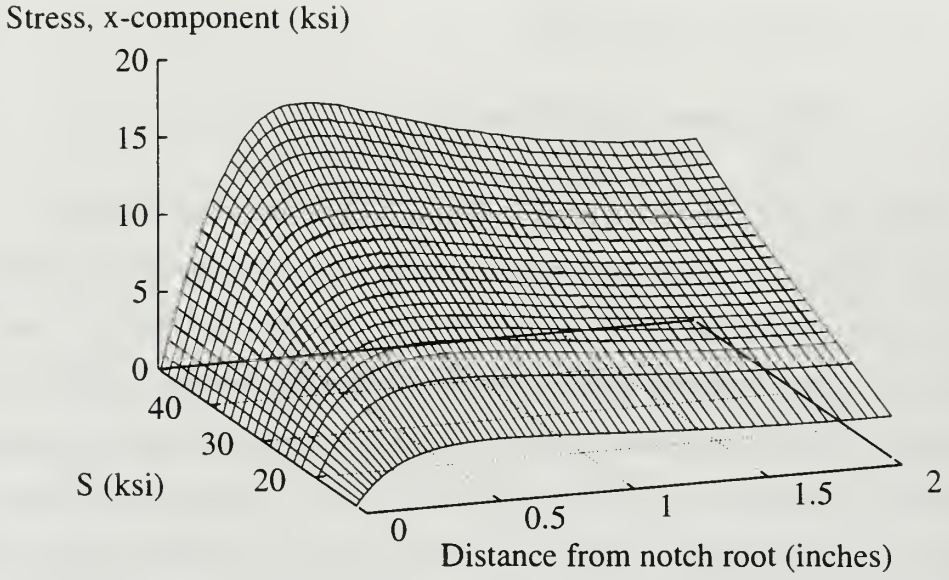

Figure 7.1. Distribution of σ_x Along Minimum Cross Section for Narrow Plate in Plane Stress.

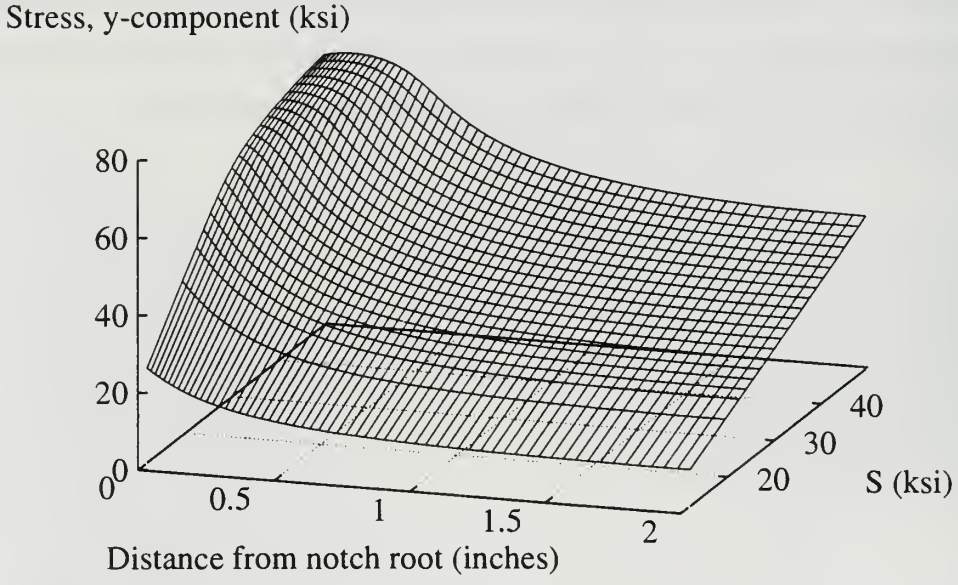

Figure 7.2. Distribution of σ_y Along Minimum Cross Section for Narrow Plate in Plane Stress.

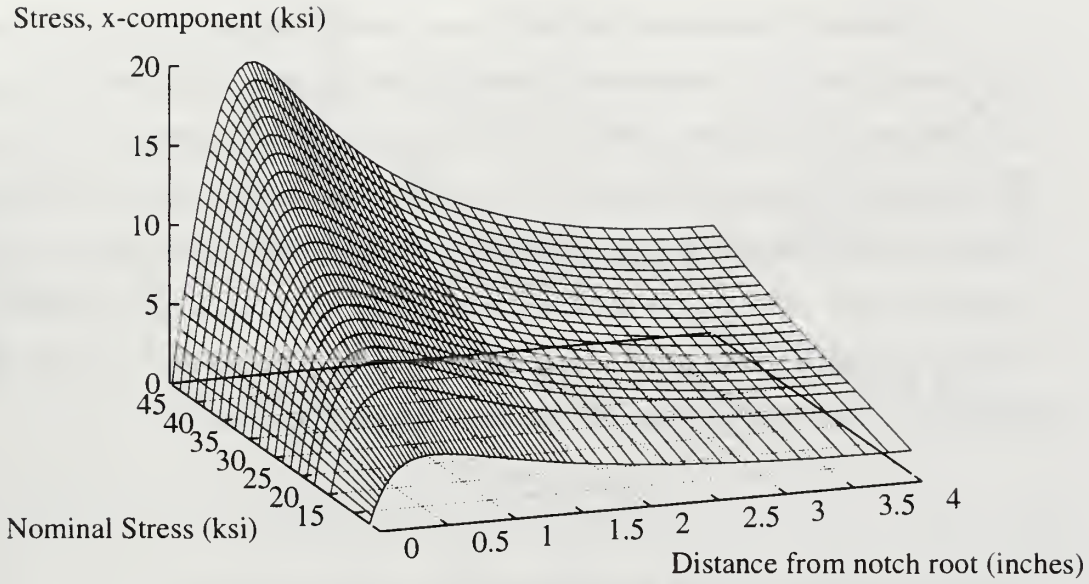

Figure 7.3. Distribution of σ_x Along Minimum Cross Section for Wide Plate in Plane Stress.

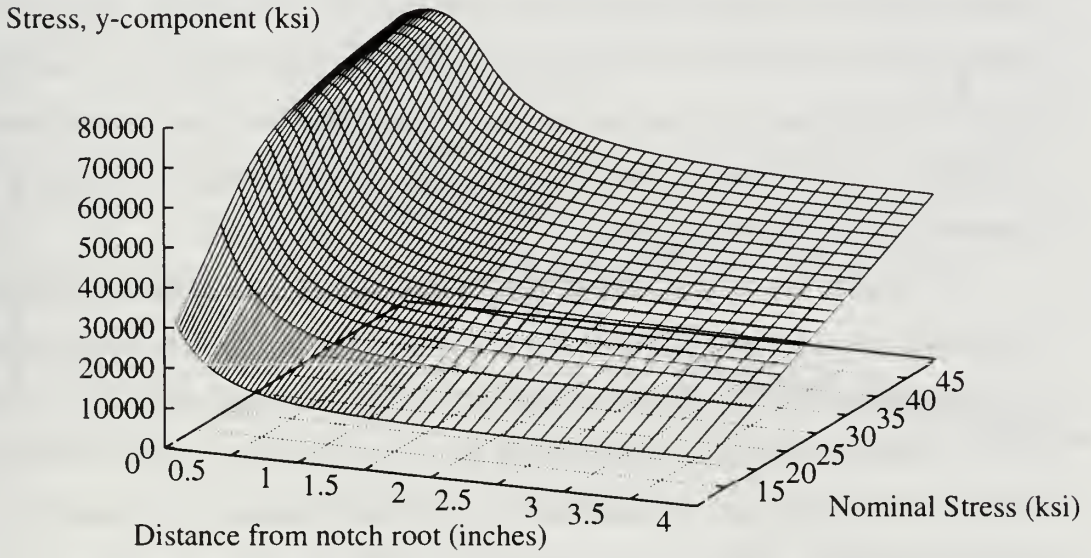

Figure 7.4. Distribution of σ_y Along Minimum Cross Section for Wide Plate in Plane Stress.

2. Notch Root Stress and Strain Calculations and Comparisons

In addition to comparing the plastic strain energy density W_p to the predicted strain energy density W_e, comparisons were also made between the finite element stress and strain results with those predicted by the Glinka and Neuber methods. The form of the Glinka method used was Equation 2.18, while for the Neuber method, Equation 2.4 was used. If the nominal stresses are high enough then $S \neq Ee$, and Equations 2.18 and 2.4 are not valid. They may be modified, however, by using the Ramberg-Osgood equation instead of Hooke's law to determine the nominal strains [Ref. 1, page 138]. For example, the Neuber's Method, from Equation 2.2 would become:

$$K_t^2 S\left[\frac{S}{E}+\left(\frac{S}{K}\right)^{1/n}\right]=\frac{\sigma^2}{E}+\sigma\left(\frac{\sigma}{K}\right)^{1/n} \qquad (7.1)$$

Likewise, the Glinka method, from Equation 2.12, would result in:

$$K_t^2 S\left[\frac{S}{E}+\frac{2}{n+1}\left(\frac{S}{K}\right)^{1/n}\right]=\frac{\sigma^2}{E}+\frac{2\sigma}{n+1}\left(\frac{\sigma}{K}\right)^{1/n} \qquad (7.2)$$

However, when these modified forms were applied to the loading levels analyzed in this thesis, the amount of improvement was minimal to none. For example, when this adjustment was calculated for the final load level in the case of the narrow plate under plane stress conditions, the error in notch root strains at the final load step decreased from -11.85% to -11.66% for the Glinka method, and for the Neuber method the error actually increased from 14.71% to 14.88%.

In Chapter VI, the strain energy density calculations showed that the predicted strain energy density based on elastic material properties (W_e) was less than the actual strain energy density (W_p). From this comparison of strain energy densities, it was known that the Glinka method would under predict the stresses and strains at the notch root. The stress and strains were also predicted based on the Neuber method. As was stated in Chapter II, the Neuber method has been shown to overestimate the stresses and strains. This was also true for all of the configurations analyzed in this thesis. These results of the Glinka method under predicting the stresses and strains and the Neuber method over predicting the stresses and strains are shown in Figures 7.5 and 7.6.

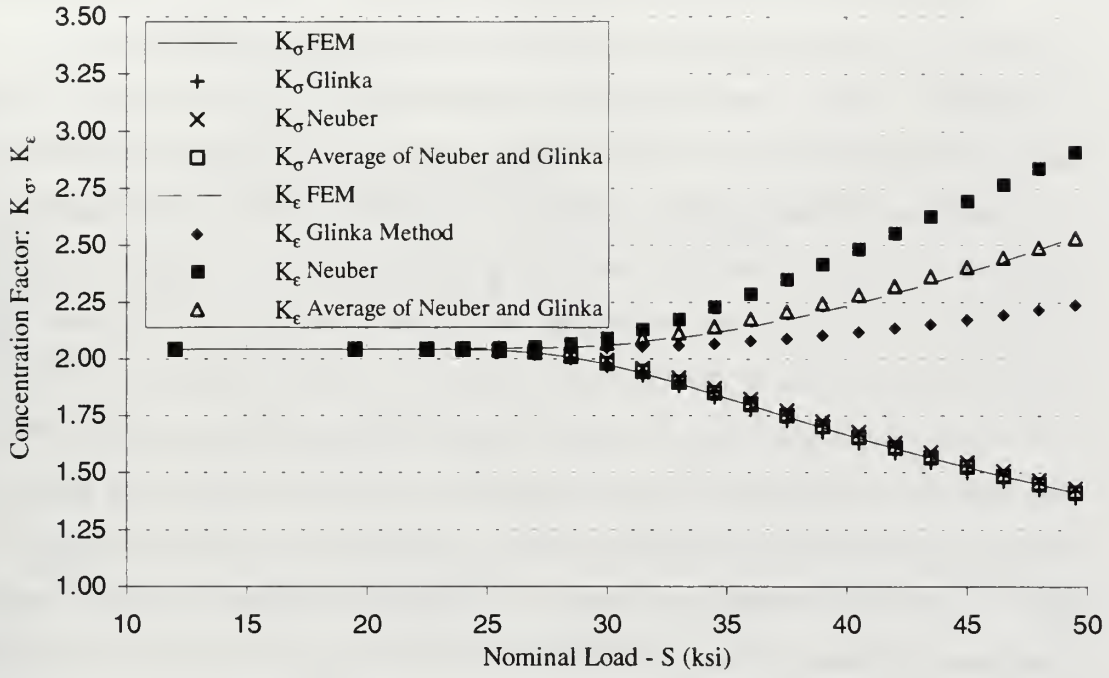

Figure 7.5. Stress/Strain Concentration Factors for Narrow Plate in Plane Stress.

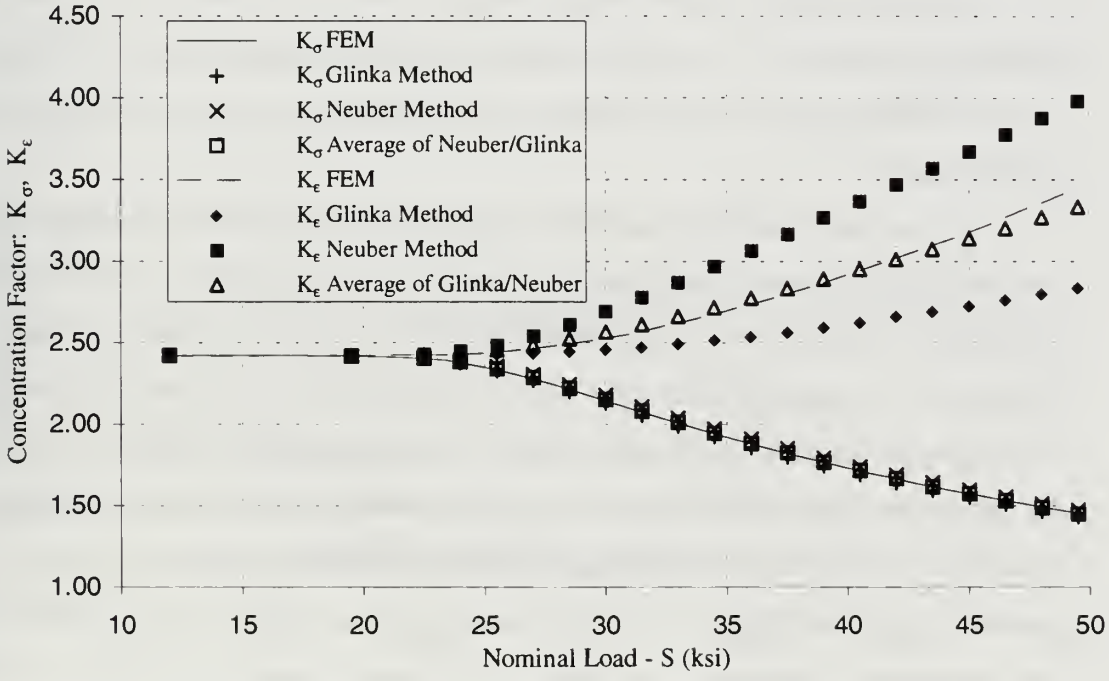

Figure 7.6. Stress/Strain Concentration Factors for Narrow Plate in Plane Stress.

These plots show the stress and strain concentration factor as a function of the nominal load for the FEM analysis, the Glinka method and the Neuber method. Additionally, a stress based on the average of the Glinka and Neuber determined stresses, and a strain determined from the Ramberg-Osgood equation and this average stress was determined for all configurations. It should be noted that whenever strain values are based on an average of the Glinka and Neuber methods, this implies that it is based on the average of the calculated stresses, and not the average of the strains. The amount of error for the stress and strain predictions for both methods is shown in Figures 7.7 through 7.10. Note that the strain is more sensitive than the stress for both calculations. This is self-evident from the fact that for the uniaxial stress-strain curve beyond the yield point, strain is highly sensitive to changes in stress. This sensitivity is plotted in Figures 7.11 and 7.12, which shows the percent error of the Glinka method predictions with respect to the percent difference in strain energy density. Note that this sensitivity is also dependent on loading condition as it relates to the current stress-strain relationship. For example, as the loading increases, the error in stress prediction appears to asymptote to a single value after an initial increase, while the error in strain is almost linear with respect to the error in strain energy density. As a material approaches perfectly plastic, then from Equation 2.6, any change or error in W_p will result in a linear change in ε, since σ will approach a constant value.

For the notch geometry and plane stress condition, the Glinka and Neuber method give an upper and lower bound to both the stress and strain predictions. Results based on the average of the stresses of the Glinka and Neuber method are in good agreement to the FEM results. It should be noted after about a S/σ_0 ratio of 0.5 to 0.6, the rate at which the error increases for the Glinka method appears to be constant, while even though the error for the Neuber method continually increases, that rate at which it increases diminishes. This results in the error for the average of these two methods to reach a maximum between a S/σ_0 ratio of 0.54 to 0.64, then decrease as the loading increases. However, it does not appear to asymptote toward zero, but to merely change sign as the error from the Glinka method becomes greater than that from the Neuber method.

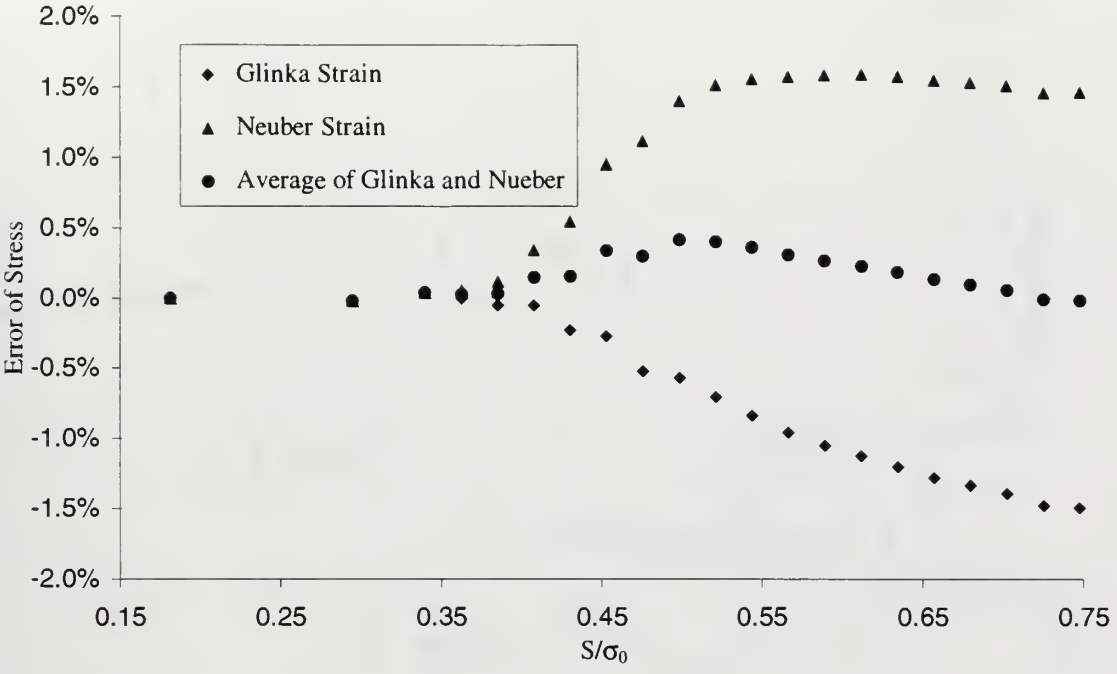

Figure 7.7. Error in Notch Stress σ_y for Glinka and Neuber Method, Narrow Plate in Plane Stress.

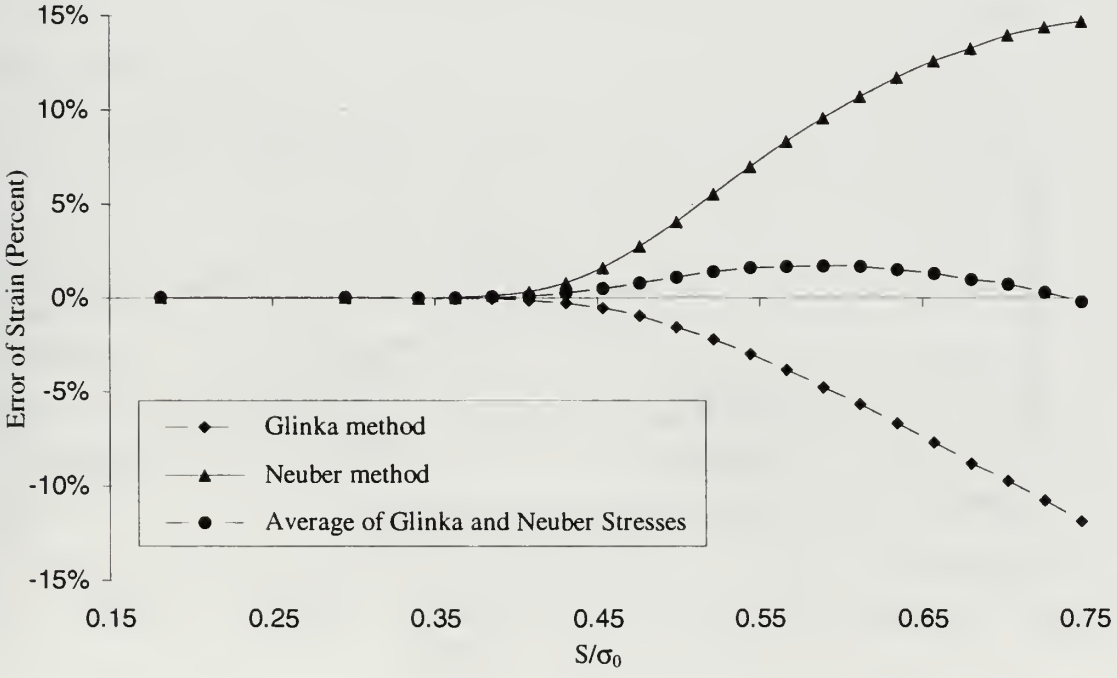

Figure 7.8. Error in Notch Strain ε_y for Glinka and Neuber Method, Narrow Plate in Plane Stress.

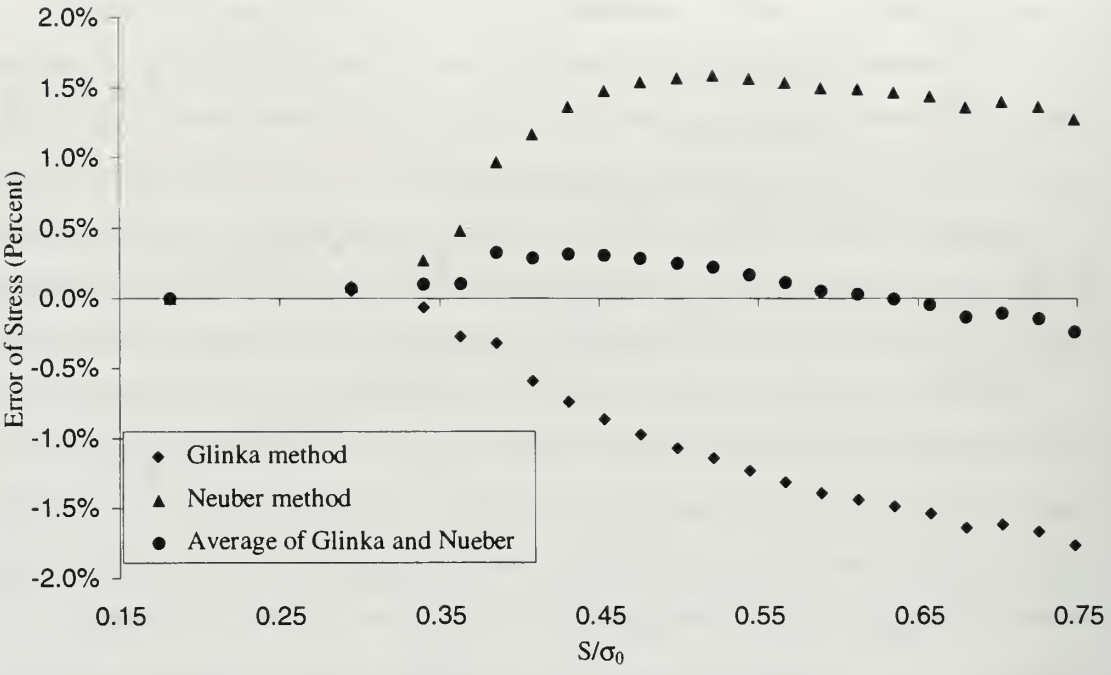

Figure 7.9. Error in Notch Stress σ_y for Glinka and Neuber Method, Wide Plate in Plane Stress.

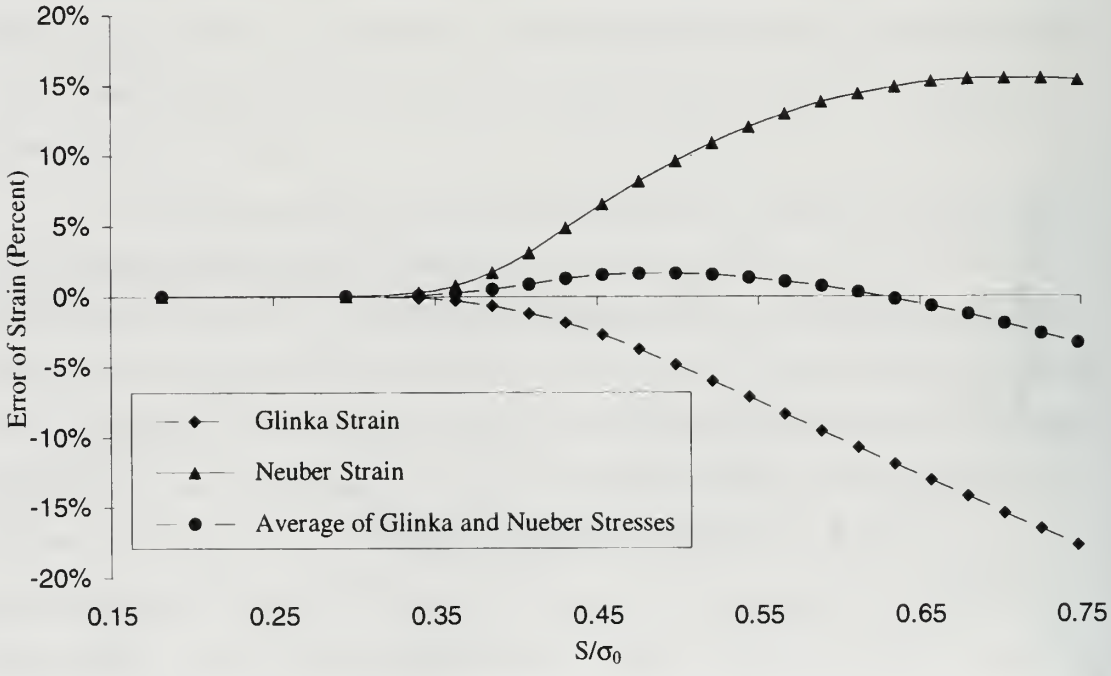

Figure 7.10. Error in Notch Strain ε_y for Glinka and Neuber Method, Wide Plate in Plane Stress.

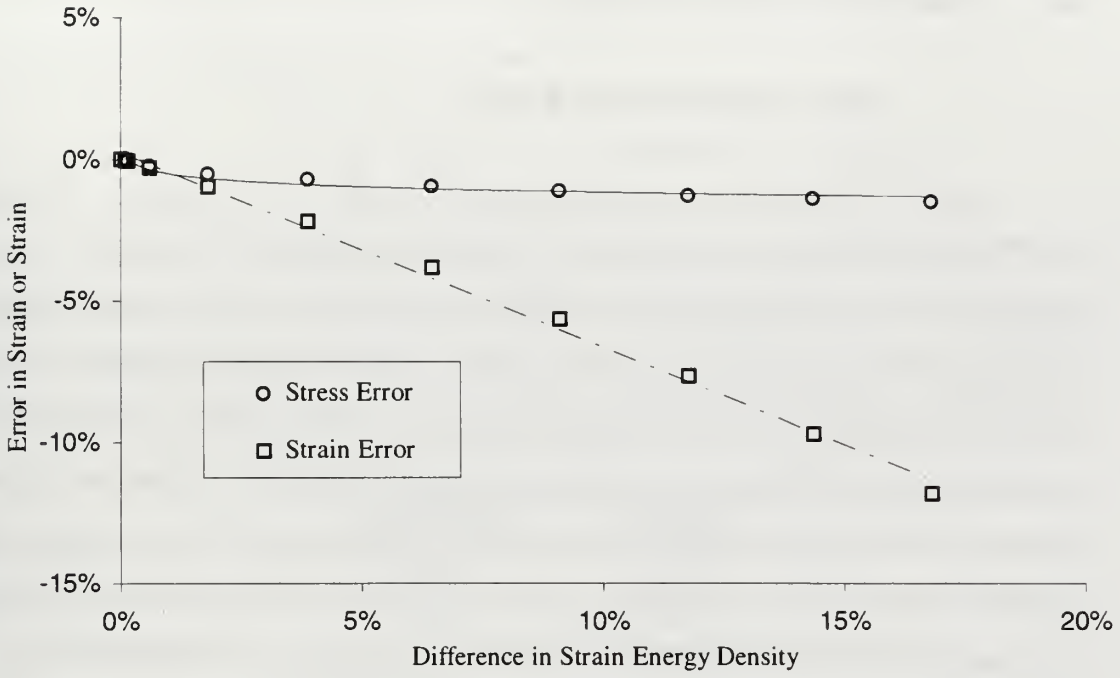

Figure 7.11. Sensitivity of Stress and Strain Error with respect to Strain Energy Density Error, Narrow Plate in Plane Stress.

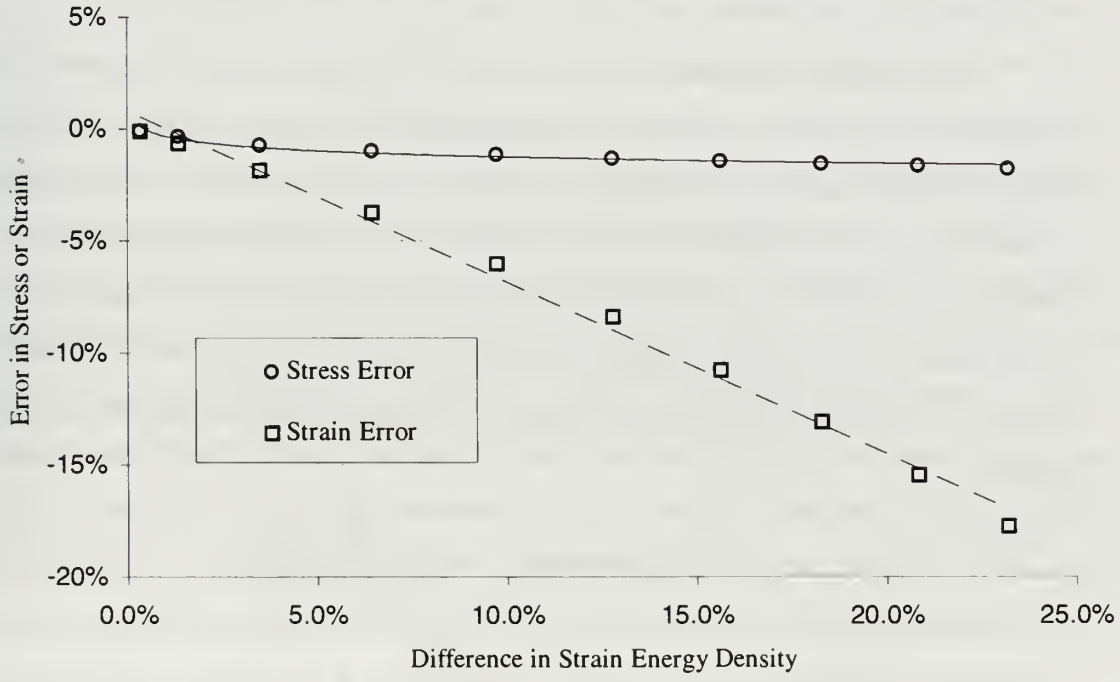

Figure 7.12. Sensitivity of Stress and Strain Error with respect to Strain Energy Density Error, Wide Plate in Plane Stress.

B. PLANE STRAIN CONDITION

1. Finite Element Method Results

The stress distribution for the plane strain case are shown in Figures 7.13 through 7.18. These plots depict either σ_x, σ_y or σ_z along the minimum cross section (y = 0) as a function of the nominal loading. When compared to the plane stress condition, the plane strain results in higher axial stresses. This is due to the σ_z stress, which results in a higher hydrostatic pressure for a given loading, thus reducing the amount of plastic growth. The reduced plastic growth likewise results in the stresses increasing at a higher rate than in the plane stress condition. Additionally, the plane strain condition results in higher stress gradients in the vicinity of the notch. As in the plane stress condition, the σ_y stress peaks at a point inward from the notch root as plastic growth occurs. For the plane strain condition, this also occurs for the σ_z stress.

2. Notch Root Stress and Strain Calculations

For the plane strain analysis at the notch root, W_p is a function of σ_y and ε_y. For the plane strain condition, however, ε_y is a function of both σ_y and σ_z, and the strain energy density equation does not reduce to the simple uniaxial version. To solve the plane strain problem, Glinka [Ref. 4, 5, 6] uses the transformation as suggested by Dowling, et al. [Ref. 19] that relates the uniaxial stress-strain curve to a plane strain stress-strain curve. From this transformed stress-strain curve, ε_y can be found directly from σ_y. To obtain ε_y, ε_y and σ_y are related to the uniaxial stress-strain curve as shown below:

$$\sigma_y = \frac{\sigma}{\sqrt{1-\mu+\mu^2}} \qquad \varepsilon_y = \frac{\varepsilon(1-\mu^2)}{\sqrt{1-\mu+\mu^2}} \tag{7.3}$$

where $$\mu = \frac{\nu + E\dfrac{\varepsilon_p}{2\sigma}}{1 + E\dfrac{\varepsilon_p}{\sigma}}$$

The Ramgerd-Osgood relationship can then be fitted to these transformed stresses and strains, and new parameters are determined:

$$\varepsilon_y = \frac{\sigma_y}{E^*} + \left(\frac{\sigma_y}{K^*}\right)^{1/n^*} \qquad \text{where} \quad E^* = \frac{E}{(1-\nu^2)} \qquad (7.4)$$

For the 7075-T6 material parameters, the plane strain transformed parameters are shown below in Table 7-1. Once these values are found, the stresses at the notch root can then be found by substituting all the normal coefficients with the transformed coefficients in Equation 2.18 and Equation 2.4, then using Equation 7.4 to determine the strains.

Coefficient	Value
E^* (ksi)	11,222
K^* (ksi)	106.77
n^*	0.0541

Table 7-1. Plane Strain Transformed Material Coefficients.

Since the results of the strain energy density comparison was much improved for the plain strain condition, it was expected that the stress calculations using the Glinka method would also be improved. This was indeed the case, as is shown in Figures 7.19 and 7.20,, which compares the stress concentration factor as a function of the nominal loading. Note that again an average value of the two methods was calculated, and plotted for comparison. Another plot of the strain values is shown in Figures 7.21 and 7.22. Here, K_fS is plotted versus the calculated notch root strain ε_y. Overlaid on this plot is the uniaxial stress-strain curve, the transformed plane strain stress-strain curve, and the notch stress versus notch strain results. Not only does this show that the Glinka method gives better results than the Neuber method, it also shows that the FEM notch root stresses and strains follow the transformed stress-strain curve. Therefore, one can conclude that the transformation used to obtain the plane strain results is valid at the notch root. The error in both the stress and strain calculations for both geometries is shown in Figures 7.23 through 7.26. These show that the Glinka method provides results three times more accurate than the Neuber method. Additionally, strains calculated based on the average stresses of the two methods give slightly more accurate values than the Glinka method

itself. This process also results in strains that are slightly higher than those of the FEM analysis, vice those of the Glinka method, which are slightly lower than the FEM analysis.

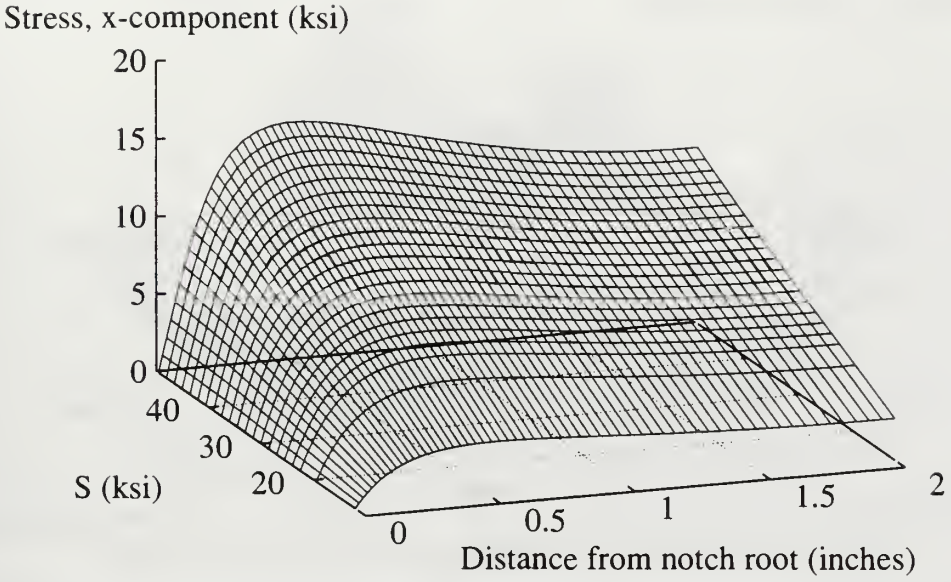

Figure 7.13. Distribution of σ_x Along Minimum Cross Section for Narrow Plate in Plane Strain.

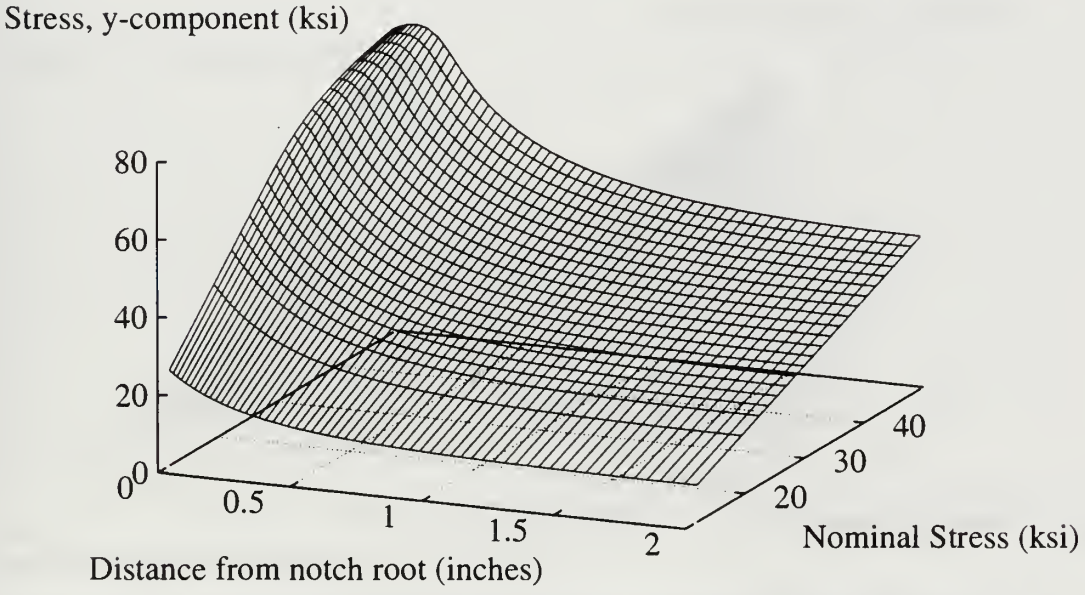

Figure 7.14. Distribution of σ_y Along Minimum Cross Section for Narrow Plate in Plane Strain.

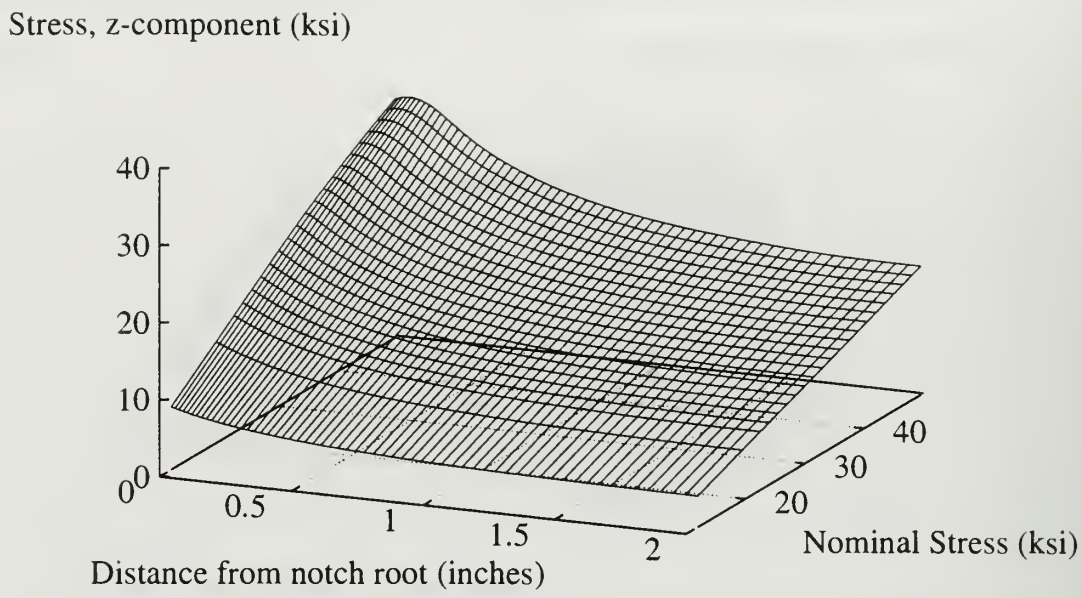

Figure 7.15. Distribution of σ_z Along Minimum Cross Section for Narrow Plate in Plane Strain.

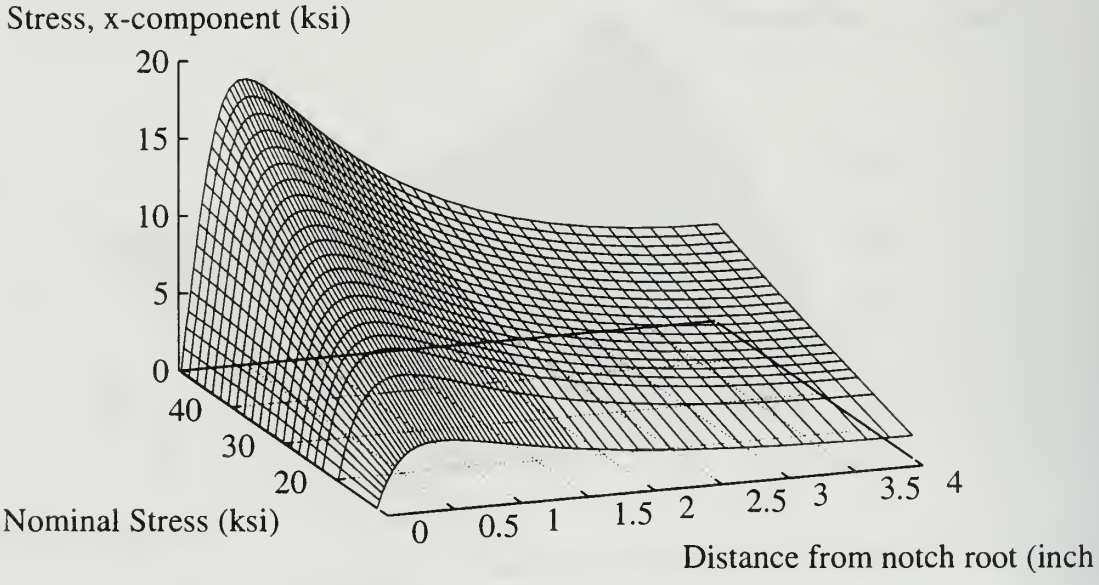

Figure 7.16. Distribution of σ_x Along Minimum Cross Section for Wide Plate in Plane Strain.

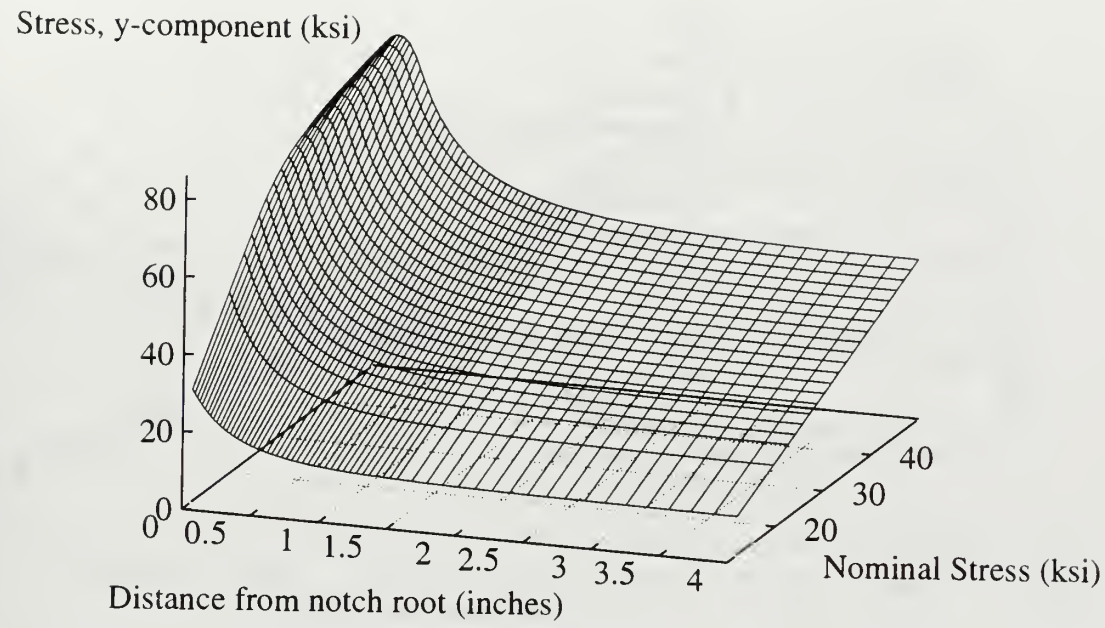

Figure 7.17. Distribution of σ_y Along Minimum Cross Section for Wide Plate in Plane Strain.

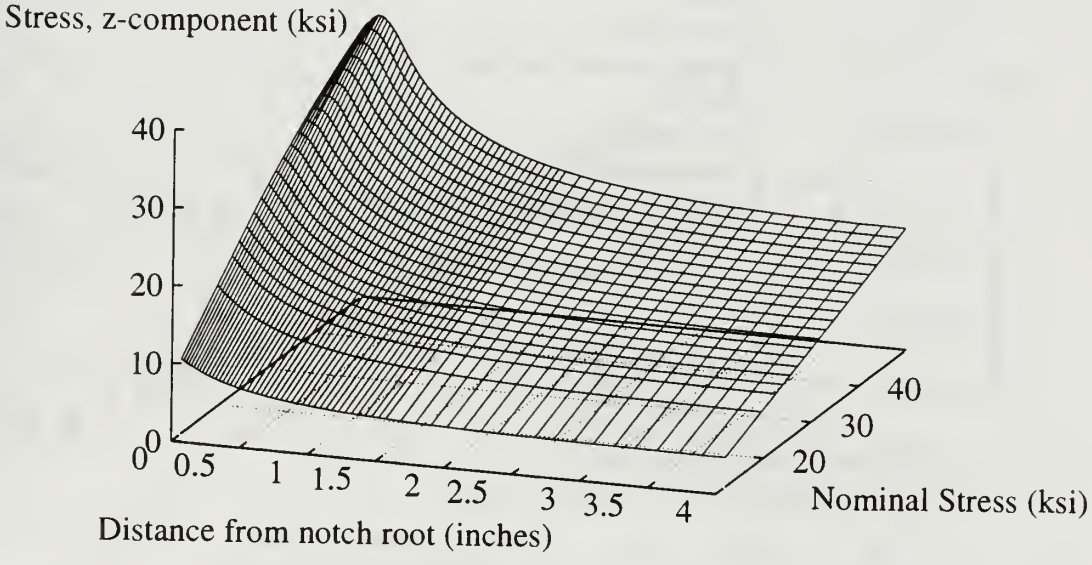

Figure 7.18. Distribution of σ_z Along Minimum Cross Section for Wide Plate in Plane Strain.

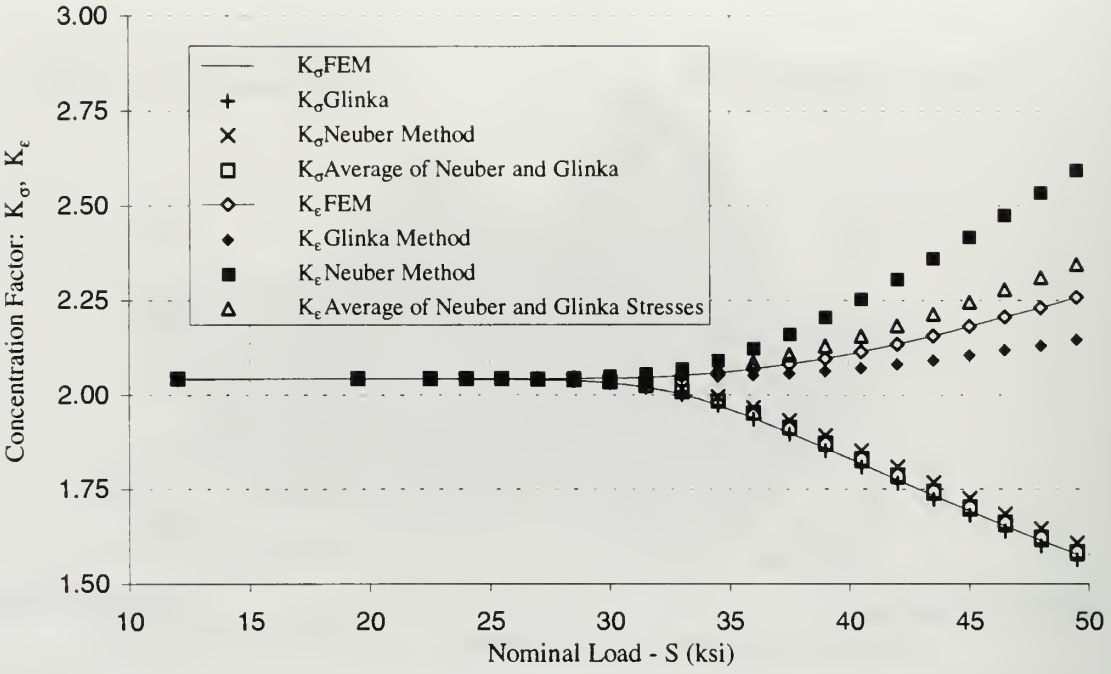

Figure 7.19. Stress/Strain Concentration Factors for Narrow Plate in Plane Strain.

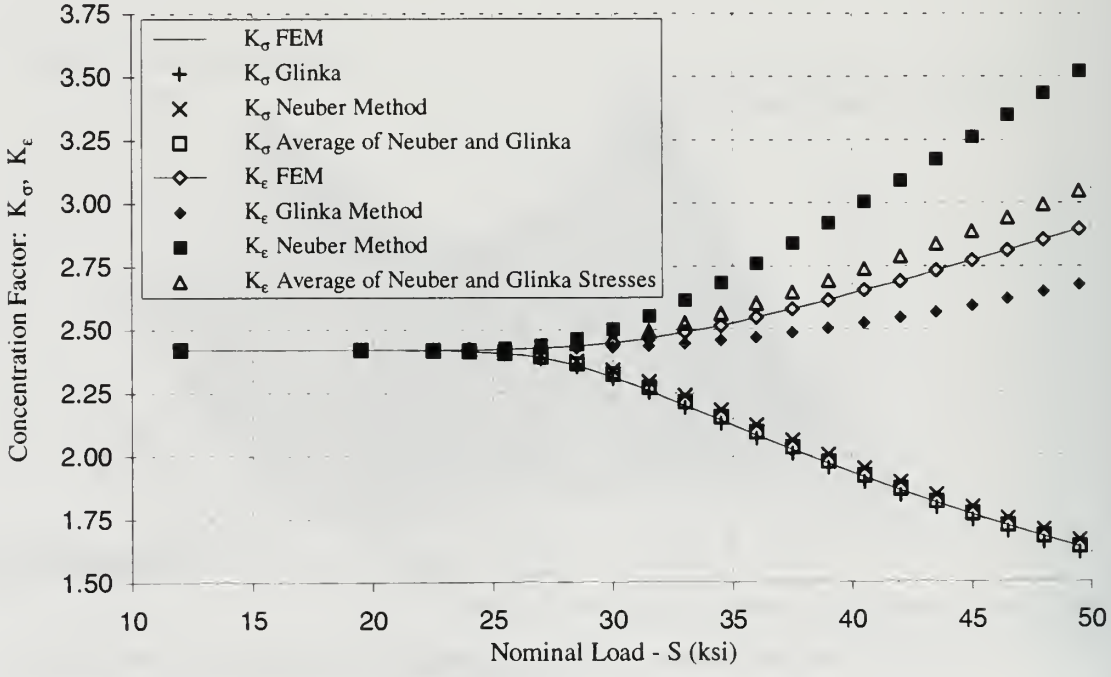

Figure 7.20. Stress/Strain Concentration Factors for Wide Plate in Plane Strain.

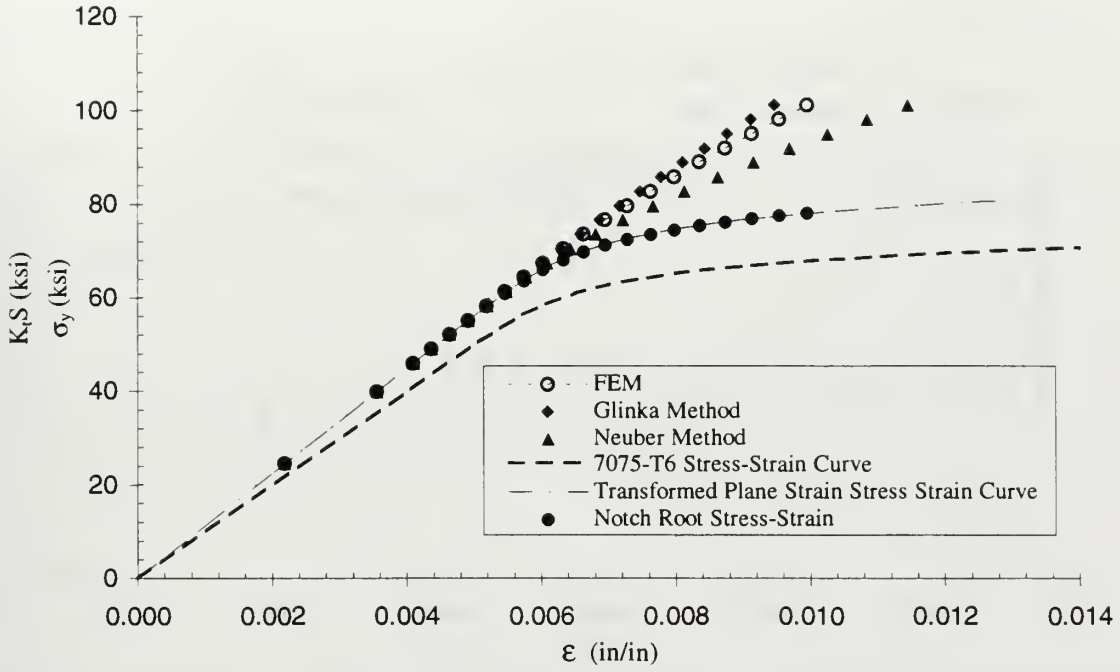

Figure 7.21. Stress and Stress Concentration versus Notch Root Strain ε_y for Narrow Plate in Plane Strain.

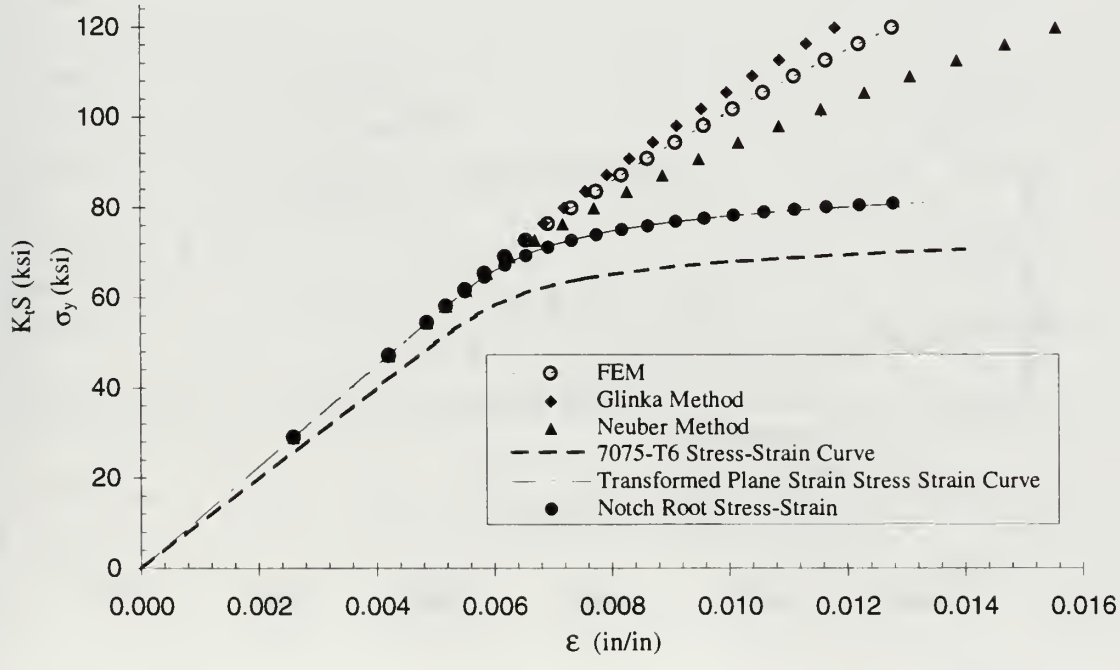

Figure 7.22. Stress and Stress Concentration versus Notch Root Strain ε_y for Wide Plate in Plane Strain.

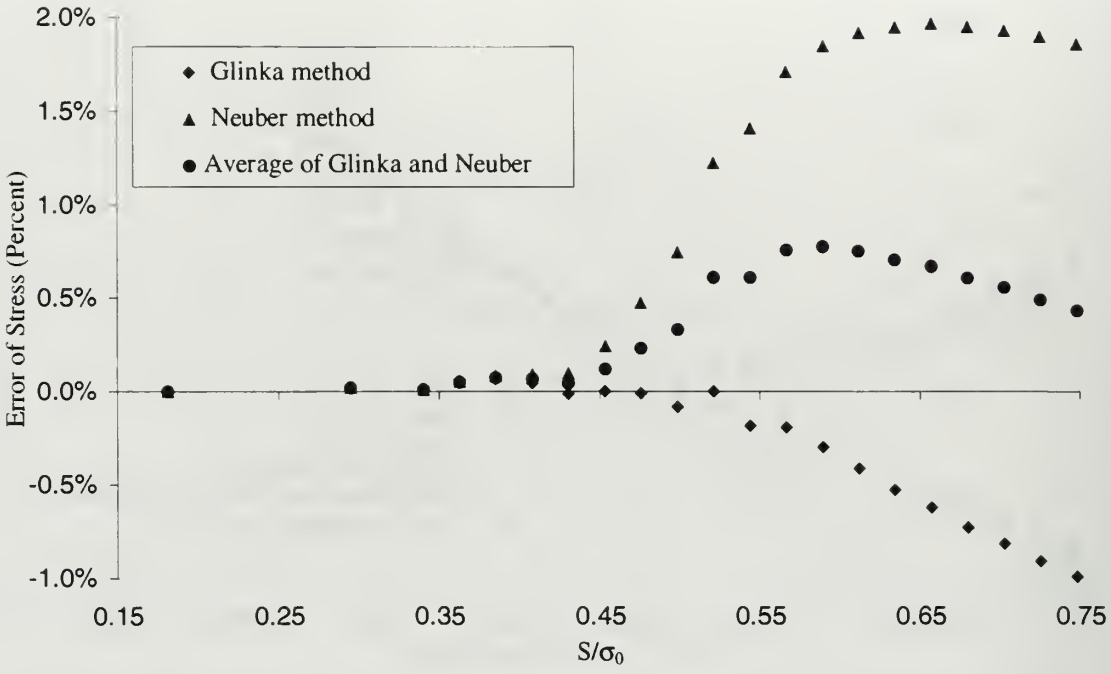

Figure 7.23. Error in Notch Stress σ_y for Glinka and Neuber Method, Narrow Plate in Plane Strain.

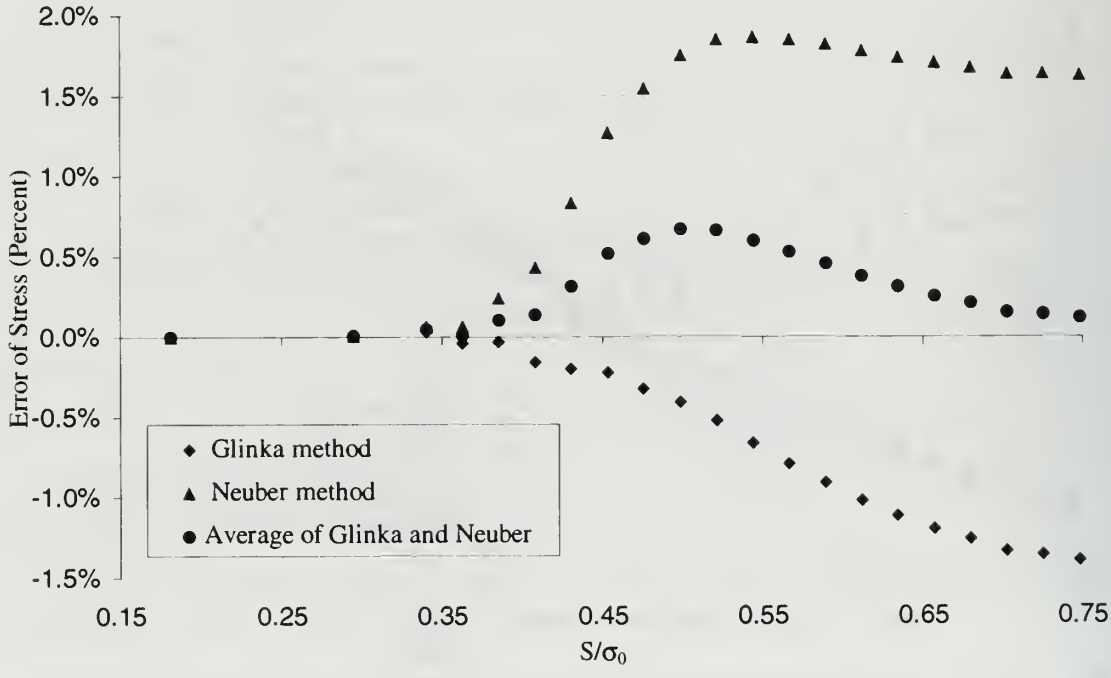

Figure 7.24. Error in Notch Stress σ_y for Glinka and Neuber Method, Wide Plate in Plane Strain.

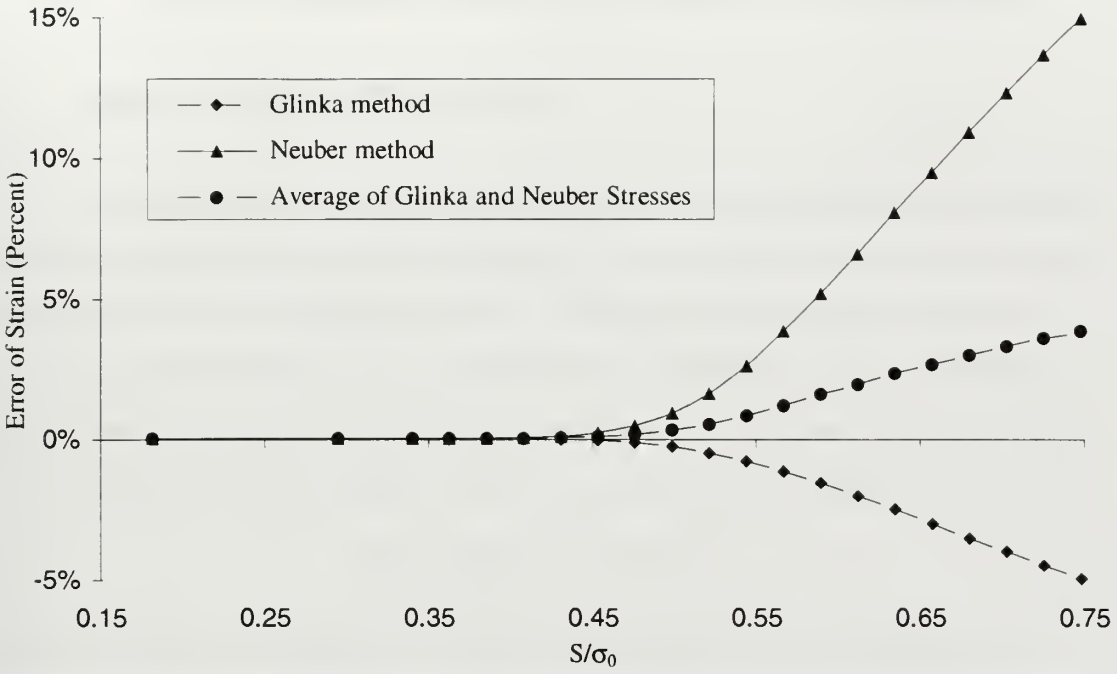

Figure 7.25. Error in Notch Strain ε_y for Glinka and Neuber Method, Narrow Plate in Plane Strain.

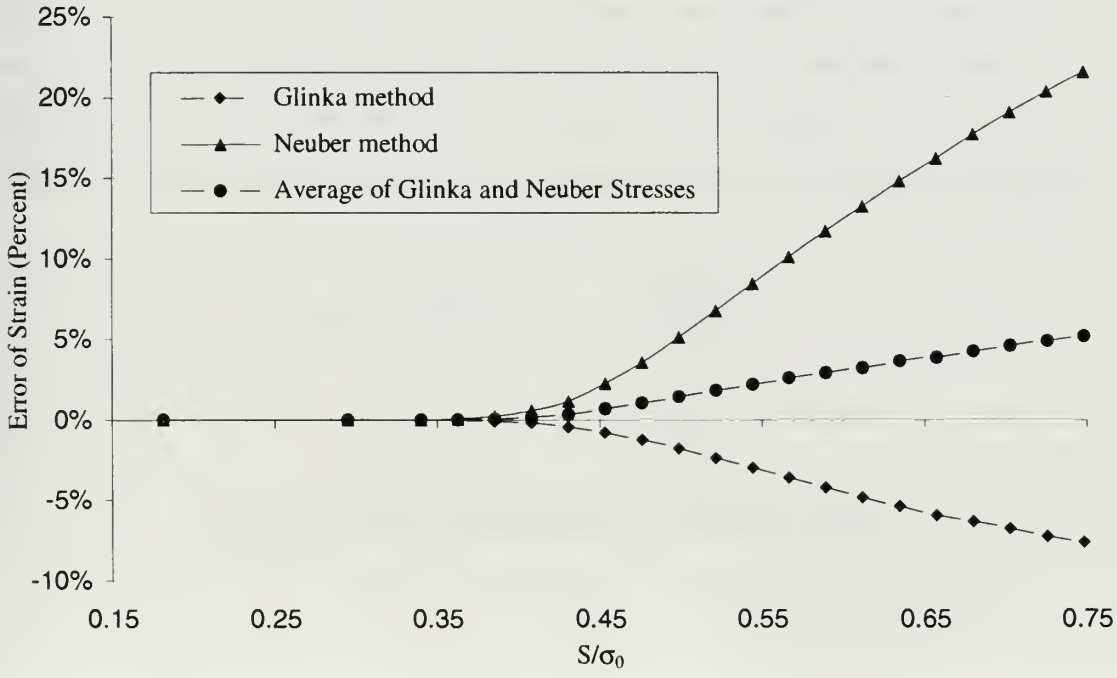

Figure 7.26. Error in Notch Strain ε_y for Glinka and Neuber Method, Wide Plate in Plane Strain.

VIII. APPLICATION OF RESULTS TO FATIGUE CALCULATIONS

A. STRAIN LIFE CALCULATIONS

To determine the consequences of the Glinka method on fatigue life calculations, the results obtained in Chapter VII for the plane stress condition were applied to a strain life analysis as given in Equation 8.1 [Ref. 1]. From this relationship, the number of reversals to crack initiation (N_f) is based on the strain amplitude ($\Delta\varepsilon$). The fatigue strength coefficient (σ'_f), fatigue ductility coefficient (ε'_f), fatigue strength exponent (b), and fatigue ductility exponent (c) are material properties and are listed in Table

$$\frac{\Delta\varepsilon}{2} = \frac{\sigma'_f}{E}\left(2N_f\right)^b + \varepsilon'_f\left(2N_f\right)^c \qquad (8.1)$$

9.1. For all fatigue calculations, it was assumed that the cyclic stress-strain curve remained constant (i.e., no hysteresis effects). Although this does not accurately depict the cyclic 7075-T6 aluminum properties, it does provide a means to compare the individual methods as they apply to fatigue calculations using the results shown in Chapter VII. Additionally, the fatigue life calculations are based on fully reversed loading, with the load levels as shown in Table 6-2 used as the amplitude of the alternating load. With these assumptions, the strain values obtained previously in Chapter VII were simply half of the strain amplitudes for the cyclic fatigue calculations.

Coefficient	Value
σ_f' (ksi)	191.0
ε_f'	0.19
b	-0.126
c	-0.52

Table 8-1. Fatigue Properties of 7075-T6 Aluminum.

B. RESULTS OF STRAIN LIFE FATIGUE PREDICTIONS

Figures 8.1 and 8.2 show reversals to failure (crack initiation), N_f, as predicted by the FEM, Glinka method, and Neuber method. These figures show the predicted life as a function of the far-field loading. The fatigue life range covers from over 6,000,000 cycles at the initial load for the narrow plate, which can be considered an infinite life, to less than 1,000 cycles at the high loads. Figures 8.3 and 8.4 show the error in fatigue predictions based on the Glinka and Neuber results as compared to the FEM analysis. It is not surprising that the greatest error occurs at the higher loading, which corresponds to where the highest differences in strain calculations occur. Additionally, the Glinka method produces greater errors at the higher loads than the Neuber method. While the Neuber method appears to have a maximum error just under 40% between an applied load of ±30 ksi to±35 ksi, the Glinka method continually gets worse, obtaining a 91% error for the wide plate at fully reversed load of ±39.6 ksi.

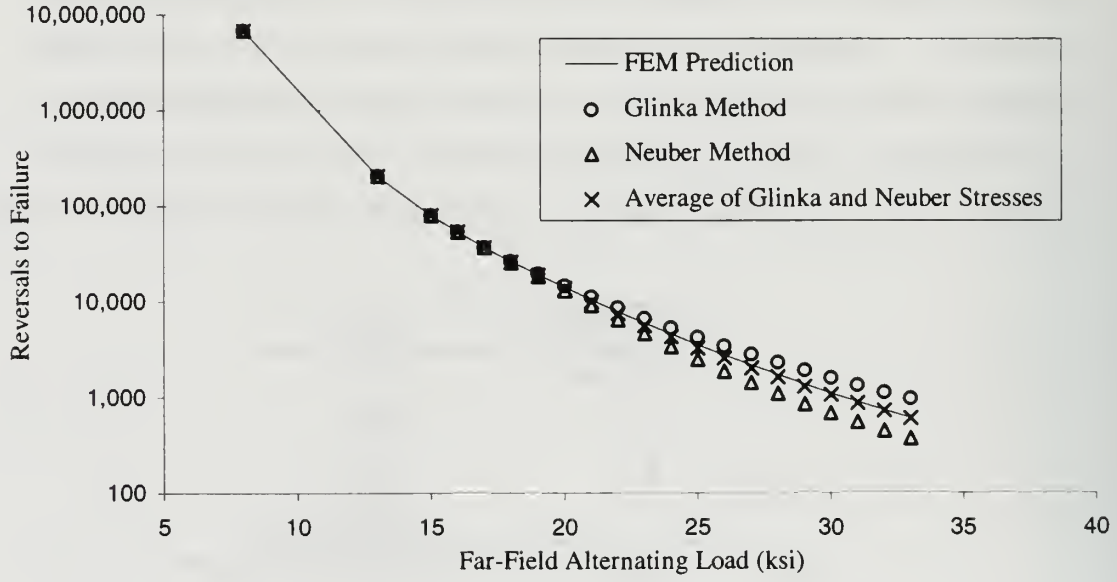

Figure 8.1. Reversals to Failure for Narrow Plate in Plane Stress.

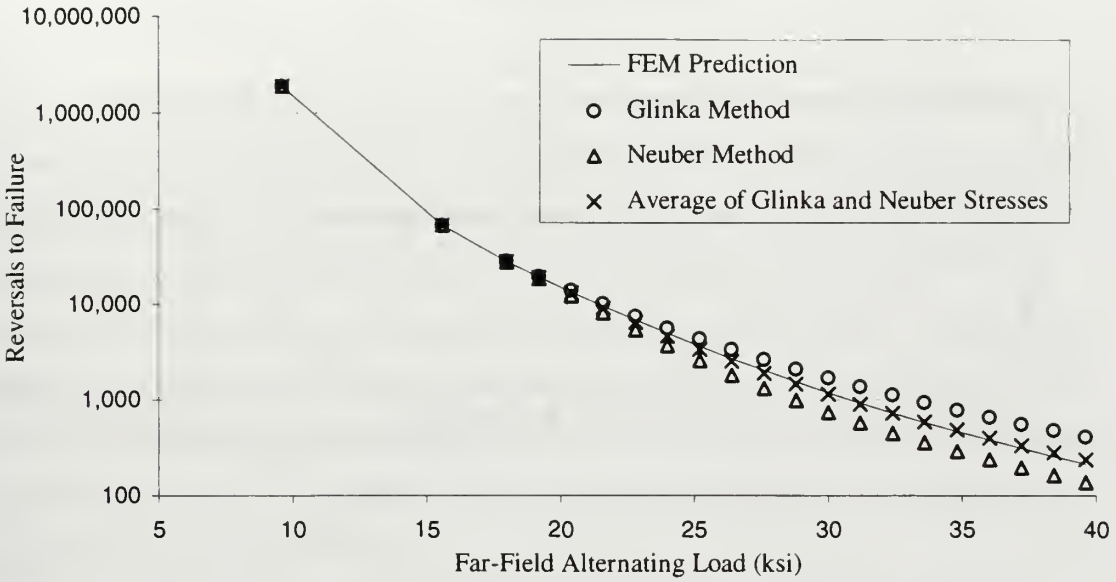

Figure 8.2. Reversals to Failure for Wide Plate in Plane Stress.

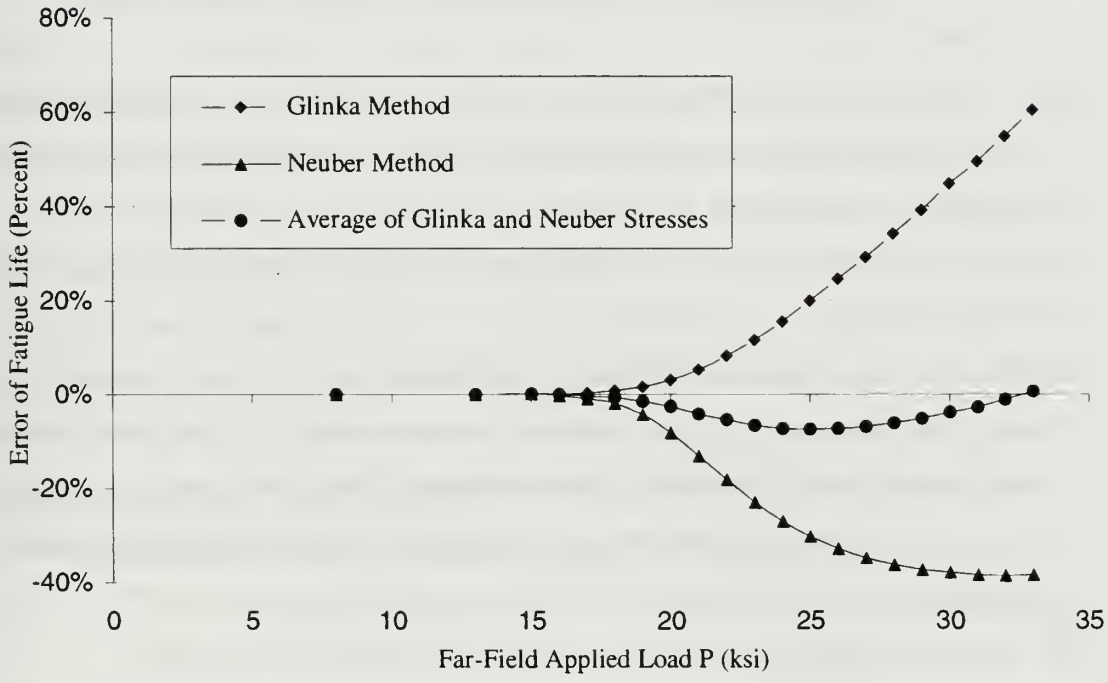

Figure 8.3. Error in Fatigue Life for Narrow Plate in Plane Stress.

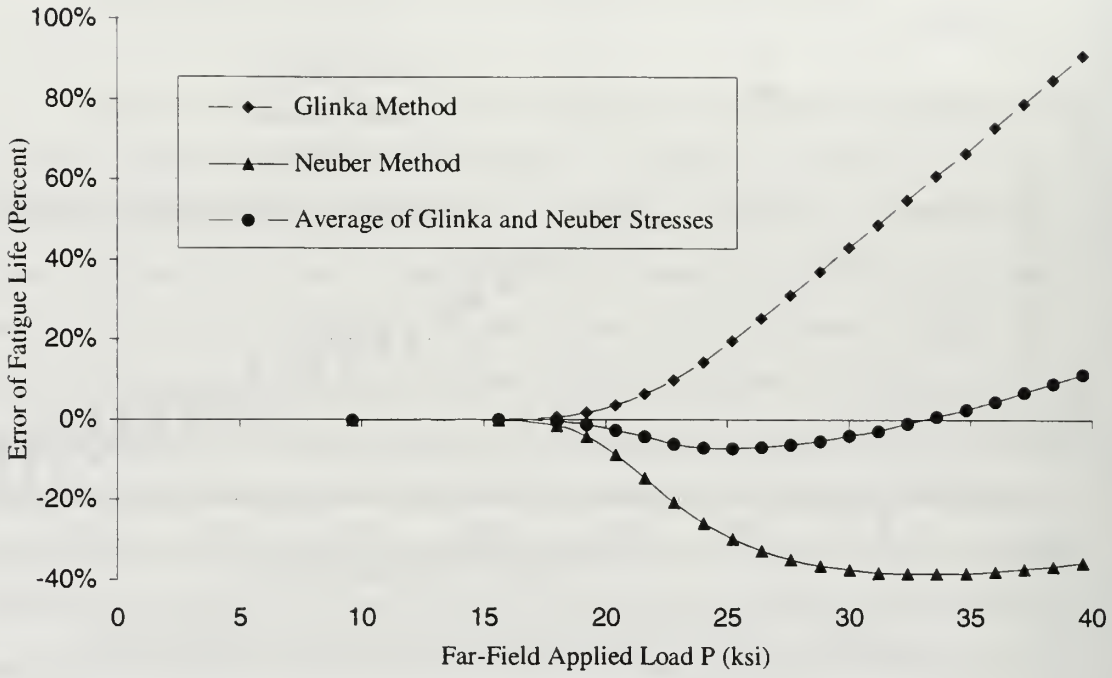

Figure 8.4. Error in Fatigue Life for Wide Plate in Plane Stress.

The comparisons of the Glinka method versus the Neuber method applied to strain life predictions show that although the error in strain calculations are of the same magnitude, underestimating the stresses and strains results in a greater error when calculating the fatigue life. Additionally, not only does this result in a greater error in fatigue calculations, but it errs on the high side of these life calculations. This could have alarming consequences when applied to safety critical parts. It should be noted that the strain-life calculations give only a model of when the actual crack initiation will occur. These comparisons do, however, provide an accurate picture of the trends in using either the Neuber or Glinka methods in a popular model that is used to make fatigue life predictions.

IX. CONCLUSIONS

This study has examined the proposal by Glinka that the strain energy density at the notch root is the same regardless if the material is elastic or elasto-plastic. A detailed comparison of the two strain energy densities was performed not only at the notch root, but throughout the field of symmetrical, semi-circular double notched plates. These comparisons were made for both plane stress and plain strain conditions. Strain energy density was calculated based on finite element analyses that had been rigorously tested with analytic solutions and experimental data. The strain energy density was numerically integrated, applying 21 load steps to reach a nominal stress equal to three fourths of the yield stress for each configuration.

In addition to strain energy density calculations, stress and strain calculations based on Glinka's strain energy density proposal and the Neuber method were performed, and compared with the finite element method results. To calculate the notch root stresses and strains, a transformation to a plane strain stress-strain relationship was performed. For the plane stress condition, the strain results were applied to fatigue life predictions, using the relationship between number of reversals and the strain amplitude.

A. FINITE ELEMENT CALCULATIONS

Prior to calculating the strain energy density for the notched geometries, the finite element program I-DEAS Master Series™ was thoroughly tested by applying it to problems that offered an analytic solution and experimental results. The conclusion concerning the accuracy of the finite element program are listed below:

- The finite element program provided very accurate results for the elastic analysis of an elliptical hole in an infinite plate under uniaxial tension. This included a comparison of all stress components along the axis of the plate and the edge of the ellipse.
- The finite element analysis of a hole in an infinite plate under elasto-plastic loading again produced exceptional results when compared to the analytic

solution. This included the both stress and strain results in the plastic and elastic region.

- The finite element analysis of the narrow plate with a central hole produced good results when compared to the experimental data of Theocaris and Marketos [Ref. 17], especially at the hole edge. When equilibrium at the minimum section was tested, the finite element analysis gave exceptional results, while the experimental data was in error by as much as 10%.

The results show that the finite element analysis had been extensively verified with analytic solutions based on the governing equations of mechanics. The stresses and strains from the finite element program were input into an integration algorithm that calculated strain energy density. Since the stresses and strains have been shown to be highly accurate, it can be inferred that the strain energy density calculations are also accurate.

B. STRAIN ENERGY DENSITY CALCULATIONS

The strain energy density based on an elastic material and an elasto-plastic material was calculated at every second load step for a total of twenty one loads. A detailed comparisons of the two strain energy densities reveal that:

- The strain energy density in the vicinity of the notch root based on elasto-plastic material properties is higher than the strain energy density assuming elastic only properties.
- The plane strain condition results in better agreement between the two strain energy densities than the plane stress condition.
- At the higher loads, the greatest deviation between the two energies occurs slightly inward from the notch root, vice at the notch root itself.
- The distribution of the two strain energy densities along the minimum cross section not only differ in magnitude, but also in shape.

C. NOTCH ROOT STRESS AND STRAIN CALCULATIONS

The notch root stress and strain values were calculated based on the Glinka proposal at the notch root, and compared to the finite element data and the Neuber method of estimating notch root stresses and strains. The comparison of these two methods revealed:

- The Glinka strain energy density method under estimates the stresses and strains, while the Neuber method overestimates the stresses and strains.
- For the plane stress condition, the two methods appeared to give an upper and lower bound. Taking the average of the stresses from each method and determining the strains from this value gave very good results.
- The Glinka method, while under estimating the stress and strain values, produces results two to three times better than the Neuber method for plane strain conditions.

D. IMPACT ON FATIGUE LIFE PREDICTIONS

Fatigue life calculations were made based on the Glinka method, the Neuber method, and the average of the stress values of these two methods, and compared to fatigue life calculations based on the FEM results for the plane stress condition. The impact of the two methods is summarized below:

- Since the Glinka method under estimated the stresses and strains, it overestimated the predicted life. However, the amount of error steadily increased with the applied load, growing up to 90% for the wide plate geometry at its final load level. For the Neuber method, the error appears to reach a maximum of 40% for a lower cyclic load and improves slightly as the load increases.
- Estimating the fatigue life by using an average of the stresses of the two methods produce results that were ±10% from those based on the finite element results.

Even though the fatigue calculations were based on finite element data, with no comparisons made to experimental data, a valid comparison between the two methods was made. Since the Glinka method under estimates the stresses and strains, the fatigue life based on this method will be greater than the actual fatigue life. This would result in parts failing prior to their expected life cycle, and would be very detrimental unless safety factors were built into the structure and the calculations.

E. RECOMMENDATIONS

This study thoroughly analyzed the Glinka strain energy density proposal for stress concentration calculations at the notch root, and compared the findings with results from the Neuber method. For the geometries studied, it was shown that the Glinka method under-predicts the stresses and strains, while the Neuber method over-predicts the stresses and strains. Further comparisons should be made not only to different geometries, but also with different material properties. A study should also be performed by comparing actual fatigue data with predictions based on the two methods. Taking an average value of the two methods appears to give good results, and as in the case of either the Glinka or Neuber method, can be a means of quickly and efficiently computing notch root stresses and strains. This mean value of the two methods should also be compared with different geometries and material properties, along with comparisons to actual fatigue data.

REFERENCES

1. Bannantine, Julie. A., Corner, Jess J., and Handrock, James L.; *Fundamentals of Metal Fatigue Analysis*, Prentice-Hall, Englewood Cliffs, New Jersey, 1990.

2. Neuber, H.: "Theory of Stress Concentration for Shear-Strained Prismatical Bodies With Arbitrary Nonlinear Stress-Strain Law," *Journal of Applied Mechanics*, **28**, 1961, pages 544-550.

3. Molski, Krzysztof and Glinka, Grzegorz: "A Method of Elastic-Plastic Stress and Strain Calculation on a Notch Root," *Materials Science and Engineering*, Volume 50, 1981, pages 93-100.

4. Glinka, Grzegorz: "Energy Density Approach to Calculation of Inelastic Strain - Stress Near Notches and Cracks," *Engineering Fracture Mechanics*, Volume 22, No. 3, 1985, pages 485-508.

5. Glinka, Grzegorz: "Calculation of Inelastic Notch-tip Strain - Stress Histories under Cyclic Loading," *Engineering Fracture Mechanics*, Volume 22, No. 5, 1985, pages 839-854.

6. Glinka, G., Ott, W., and Nowack, H.: "Elastoplastic Plane Strain Analysis of Stresses and Strains at the Notch Root," *Journal of Engineering Materials and Technology*, Volume 110, 1988, pages 195 204.

7. Sharpe, W. N. Jr., Yang, C. H., and Trogoning, R. L., "An Evaluation of the Neuber and Glinka Relations for Monotonic Loading," *Journal of Applied Mechanics*, Volume 59, June 1992, pp. S50-S56.

8. Mendelson, A., *Plasticity: Theory and Application*, The MacMillan Company, New York, 1968.

9. Durelli, A. J., and Murray, W. M., "Stress Distribution Around an Elliptical Discontinuity in Any Two-Dinemsional, Uniform and Axial, System of Combined Stress," *Experimental Stress Analysis*, Volume 1, No. 1, May 1943, pages 19-31.

10. Brown, David K., "A Computer Program To Calculate the Elastic Stress and Displacement Fields Around An Elliptical Hole Under Any Applied Plane State of Stress," *Computers and Structures*, Volume 7, No. 4, 1977, pages 571-580.

11. Davis, E. A., "Extension of Iteration Method for Determining Strain Distributions to the Uniformly Stresses Plate with a Hole," *Journal of Applied Mechanics*, Volume 30, 1963, pages 210-214; discussions, *ibid.*, Volume 31, 1964, pages 362-364.

12. Tuba, I. S., "Elastic-Plastic Stress and Stain Concentration Factors at a Circular Hole in a Uniformly Stressed Infinite Plate," *Journal of Applied Mechanics*, Volume 32, 1965, pages 710-711.

13. Budiansky, Bernard, and Mangasarian, O. L., "Plastic Stress Concentration at a Circular Hole in an Infinite Sheet Subjected to Equal Biaxial Tension," *Journal of Applied Mechanics*," Volume 27, March 1960, pages 59-64.

14. Chakrabarty, J., *Theory of Plasticity*. McGraw-Hill Book Company, New York, 1987.

15. Durelli, A. J. and Sciammarella, C. A., "Elastoplastic Stress and Strain Distribution in a Finite Plate With a Circular Hole Subject to Unidimensional Load," *Journal of Applied Mechanics*, Volume 30, 1963, pages 115-121.

16. Military Handbook, *Metallic Materials and Elements for Aerospace Vehicle Structures Volume 1 of 2* (MIL-HDDBK-5G), Department of Defense, 1 November 1994.

17. Theocaris, P. S. and Marketos, E., "Elastic-plastic Analysis of Perforated Thin Strips of a Strain-Hardening Material," *Journal of the Mechanics and Physics of Solids*, Volume 12, 1964, pages 377-390.

18. Theocaris, P. S. and Marketos, E., "Elastic-plastic Strain and Stress Distribution in Notched Plates Under Plane Stress," *Journal of the Mechanics and Physics of Solids*, Volume 11, 1963, pages 411-428.

19. Dowling, N., Brose, W. R., and Wilson, W. K., "Notched Member Fatigue Life Predictions by the Local Strain Approach," in Fatigue Under Complex Loading, Volume 6 of *Advances in Engineering*, R. M. Wetzel, Ed., Society of Automotive Engineers, Warrendale, PA, 1977.

INITIAL DISTRIBUTION LIST

1. Defense Technical Information Center 2
   Cameron Station
   Alexandria, Virginia 22304-6145

2. Library, Code 52 2
   Naval Postgraduate School
   Monterey, California 93943-5101

3. Department of Aeronautics and Astronautics, Code AA/Co 1
   Naval Postgraduate School
   Monterey, California 93943-5101

4. Department of Aeronautics and Astronautics, Code AA/Li 1
   Naval Postgraduate School
   Monterey, California 93943-5101

5. Department of Mechanical Engineering, Code ME/Kw 1
   Naval Postgraduate School
   Monterey, California 93943-5101

6. LT Grant B. Stephenson 2
   2129 W. Norcliffe Way
   Oak Harbor, WA 98277